

DISS. ETH NO. 20498

Imaging Laser Doppler Velocimetry

A dissertation submitted to
ETH ZÜRICH

for the degree of
Doctor of Sciences

presented by

ALEXANDER H. MEIER

Dipl.-Ing. ETH Zürich
born August 2, 1980
citizen of Dänikon ZH, Switzerland

accepted on the recommendation of

Prof. Dr. Thomas Rösgen, examiner
Prof. Dr.-Ing. habil. Cameron Tropea, co-examiner

2012

Copyright © 2012 ALEXANDER H. MEIER
Institute of Fluidynamics, ETH Zürich
All rights reserved.

Imaging Laser Doppler Velocimetry

Published and distributed by:

Institute of Fluidynamics
ETH Zürich
ETH Zentrum, ML H35
CH-8092 Zürich
Switzerland

<http://www.ifd.mavt.ethz.ch>

Printed in Switzerland by:

Druckzentrum ETH Zentrum
ETH Zentrum, HG E 39
CH-8092 Zürich
Switzerland

Abstract

The present work documents the development of a new measurement technique that allows to measure the velocity distribution of a flow field in an illuminated plane. The measurement principle is based on using the Doppler shift of light scattered from particles moving within the flow and optical heterodyning to demodulate the signals. This new technique can therefore be regarded as the planar extension of the well known laser Doppler velocimetry (LDV).

Different planar configurations are tested to assess the potential of this new technique. First, a simple heterodyne Doppler global velocimetry system (HDGV) is presented. This setup can be regarded as the planar extension of reference beam LDV. Using this setup the velocity distributions of a rotating disk and of a buoyant plume are measured. While these measurements prove the basic feasibility of measuring 2-D velocity distributions in a Doppler arrangement, the achieved measurement range is limited to some mm/s, due to the high occurring signal frequencies.

To extend this limited measurement range a dual light sheet illumination setup is introduced in imaging laser Doppler velocimetry (ILDV). The dual light sheet illumination reduces the high signal frequencies and allows to measure a specific velocity component such as one of the in-plane velocity components or the out-of-plane velocity component. This technique can be regarded as the planar 2-D extension of dual-beam LDV. The capability of this method is examined on a rotating disk and in two different flow fields. In air a laminar jet is measured and in water ILDV is applied to a fully turbulent jet. The in-plane velocity measurements in the flow fields are simultaneously validated using particle imaging velocimetry (PIV) and show a very good agreement between PIV and ILDV. These measurements demonstrate the potential of ILDV to measure instantaneous and mean flow fields and extend the velocity range of HDGV by more than one order of magnitude to approximately 10 cm/s.

The measurable velocity range is basically only limited by the frame rate of the recording camera. From the present measurements it can be extrapolated that with a camera recording at 1 Mfps a measurement range of 40 m/s can be achieved.

Kurzfassung

Die vorliegende Arbeit dokumentiert die Entwicklung einer neuartigen Messtechnik, mit welcher die Geschwindigkeitsverteilung in einer mit einem Lichtschnitt beleuchteten Ebene eines Strömungsfeldes gemessen werden kann. Das Messprinzip basiert auf der Auswertung der Dopplerverschiebung des Lichts, welches von in der Strömung mitbewegten Partikeln gestreut wird. Diese Dopplerverschiebung wird durch die Überlagerung von mehreren Lichtwellen und der dadurch entstehenden Interferenz in ein moduliertes Signal konvertiert, dessen Frequenz mit der Geschwindigkeit gekoppelt ist. Diese Messtechnik kann deshalb als die planare Erweiterung der Laser Doppler Anemometrie (LDA) betrachtet werden.

Verschiedene mögliche planare Konfigurationen wurden im Rahmen dieser Arbeit auf ihre Eignung zur Geschwindigkeitsmessung in einer Strömung hin untersucht. Als erste planare Erweiterung wurde die sog. Heterodyne Doppler Global Velocimetry (HDGV) entwickelt, bei der die Dopplerverschiebung mittels eines Referenzstrahls demoduliert wird. Mit diesem System wurden die Geschwindigkeitsverteilungen auf einer rotierenden Scheibe und in einer dichtegetriebenen Strömung gemessen. Dadurch konnte gezeigt werden, dass es grundsätzlich möglich ist, auf diese Weise auch planare Geschwindigkeitsfelder zu messen. Die messbaren Geschwindigkeiten waren aufgrund der hohen auftretenden Signalfrequenzen jedoch beschränkt auf einige mm/s.

Um den Messbereich zu erweitern, wurde deshalb die sogenannte Imaging Laser Doppler Velocimetry (ILDV) entwickelt, in der die Strömung mittels zwei sich kreuzenden Lichtschnitten beleuchtet wird, wodurch die zu detektierenden Signalfrequenzen stark reduziert werden können. Die Möglichkeiten dieser Messtechnik wurden ebenfalls an einer rotierenden Scheibe und in zwei verschiedenen Strömungen untersucht. Die Geschwindigkeitsverteilungen in den Strömungen wurden zur Validierung gleichzeitig mit Particle Image Velocimetry (PIV) gemessen. Die Übereinstimmung zwischen PIV und ILDV waren sehr gut. Mit dieser Technik konnte der Messbereich um mehr als eine Größenordnung auf 10 cm/s erweitert werden.

Der Messbereich ist jedoch nur durch die Aufnahmegeschwindigkeit der verwendeten Kamera limitiert. Aus den durchgeführten Messungen kann extrapoliert werden, dass mit einer Kamera, die 1 Million Bilder/s aufnimmt, der Messbereich auf 40 m/s erweitert werden kann.

Contents

| | |
|-------------------------------------------|------------|
| Abstract | iii |
| Kurzfassung | v |
| Nomenclature | xv |
| 1 Introduction | 1 |
| 2 Method | 3 |
| 2.1 Signal Formation | 3 |
| 2.1.1 Doppler Effect | 3 |
| 2.1.2 Optical Heterodyning | 4 |
| 2.1.3 Directional Ambiguity | 7 |
| 2.1.4 Finite Signal Duration | 8 |
| 2.1.5 Multiple Particle Scattering | 10 |
| 2.2 Planar Extension | 11 |
| 2.2.1 Reference Beam Method | 12 |
| 2.2.2 Dual Light Sheet Method | 15 |
| 2.2.3 System Setup | 19 |
| 2.2.4 Required Coherence Length | 22 |
| 2.2.5 Light Sources | 26 |
| 2.3 Signal Detection | 27 |
| 2.3.1 High Speed Camera | 28 |
| 2.3.2 Smart Pixel Detector Array | 30 |
| 2.4 Data Analysis | 34 |
| 2.4.1 Fourier Analysis | 34 |
| 2.4.2 Autocorrelation Based Analysis | 35 |
| 3 Measurements | 55 |
| 3.1 Introduction | 55 |
| 3.2 System Components | 55 |
| 3.2.1 Light Source | 55 |
| 3.2.2 Frequency Shifting | 56 |
| 3.2.3 Camera Systems | 57 |
| 3.3 Heterodyne Doppler Global Velocimetry | 61 |
| 3.3.1 Rotating Disk Experiment | 61 |

| | | |
|----------|---------------------------------------------|------------|
| 3.3.2 | Buoyant Plume Experiment | 64 |
| 3.3.3 | Conclusions | 66 |
| 3.4 | Imaging Laser Doppler Velocimetry | 67 |
| 3.4.1 | ILDV with the pOCTii SPDA | 67 |
| 3.4.2 | ILDV with a High Speed Camera | 77 |
| 4 | Conclusions | 97 |
| 4.1 | Achievements | 97 |
| 4.2 | Outlook | 99 |
| | Bibliography | 101 |
| | Curriculum vitae | 105 |
| | List of Publications | 107 |

List of Figures

| | | |
|------|--------------------------------------------------------------------------------------------------------------------------|----|
| 2.1 | Geometry of the scattering process. | 4 |
| 2.2 | Geometry of the scattering process for a dual beam illumination. | 6 |
| 2.3 | Finite signal duration of a particle passing through the probe volume. | 8 |
| 2.4 | Peak broadening of the PSD due to the finite particle passage time. | 9 |
| 2.5 | Visibility of the Doppler signal. | 11 |
| 2.6 | Schematic of an imaging reference beam setup. | 13 |
| 2.7 | Different optical arrangements: (a) Perpendicular arrangement, (b) Scheimpflug arrangement. | 14 |
| 2.8 | Checkerboard imaged with different observation angles α | 14 |
| 2.9 | Schematic of a dual light sheet setup. | 16 |
| 2.10 | Co-planar light sheets setup. | 17 |
| 2.11 | Crossed light sheets setup. | 17 |
| 2.12 | Close up on the cross section of the crossed light sheets setup. | 18 |
| 2.13 | Measurement volume length for the crossed light sheets setup. | 18 |
| 2.14 | Crossing angle variation in the xy-plane of the co-planar light sheet configuration. | 20 |
| 2.15 | Optical paths in the HDGV setup. | 23 |
| 2.16 | Co-planar light sheet setup. | 23 |
| 2.17 | <i>OPD</i> in the xy-plane of the co-planar light sheet configuration. | 24 |
| 2.18 | Crossed light sheets setup. | 25 |
| 2.19 | <i>OPD</i> in the xz-plane of the crossed light sheets configuration. | 25 |
| 2.20 | <i>OPD</i> in the xy-plane of the crossed light sheets configuration at the upper edge of the light sheet. | 26 |
| 2.21 | Output amplitude of the lock-in detection as a function of the signal frequency for different averaging lengths. | 33 |
| 2.22 | PSD of W_{HP} , W_H^4 and $W_H^4 W_{HP}/2$ for $N_f = 4$ | 39 |
| 2.23 | PSD of W_{HP} , W_H^{16} and $W_H^{16} W_{HP}/4$ for $N_f = 16$ | 40 |
| 2.24 | Peak shift of the PSD $W(f)$ of a signal due to the filter applied on it. | 40 |

| | | |
|------|----------------------------------------------------------------------------------------------------------------------------------------------------------------------------------------|----|
| 2.25 | Typical signal used for the calculation of $\hat{\nu}$ | 41 |
| 2.26 | Dependence of $\hat{\nu}$ on N_f for $f_B = 0$ and $\tau = 1/f_s$ | 42 |
| 2.27 | Dependence of $\hat{\nu}$ on N_f for $f_B = 0$ and $\tau = 4/f_s$ | 43 |
| 2.28 | Bias error ϵ for different N_p for $N_f = 4$ and $\tau = 1/f_s$ | 43 |
| 2.29 | Bias error ϵ for different N_f for $N_p = 5$ and $\tau = 1/f_s$ | 44 |
| 2.30 | Bias error ϵ for different N_p for $N_f = 8$ and $\tau = 4/f_s$ | 44 |
| 2.31 | Bias error ϵ for different N_f for $N_p = 5, 10$ and $\tau = 4/f_s$ | 45 |
| 2.32 | Bias error ϵ for different f_B for $N_f = 4$ and $\tau = 1/f_s$ | 46 |
| 2.33 | Bias error ϵ for different f_B for $N_f = 8, 32$ and $\tau = 4/f_s$ | 46 |
| 2.34 | Convergence of $\hat{\nu}$ for different N_f at $f = 0.15f_s$, $f_B/f_s = 5\%$ and $\tau = 4/f_s$ | 47 |
| 2.35 | Power spectral density W_{SPDA} | 49 |
| 2.36 | $\hat{\nu}$ as a function of the real frequency f for different time delays τ | 50 |
| 2.37 | Bias error ϵ for different N_p for $\tau = T_{qp}$ | 50 |
| 2.38 | Bias error ϵ for different N_p for $\tau = 4T_{qp}$ | 51 |
| 2.39 | Bias error ϵ for different f_B and $\tau = T_{qp}$ | 51 |
| 2.40 | Bias error ϵ for different f_B and $\tau = 4T_{qp}$ | 52 |
| 2.41 | Convergence of $\hat{\nu}$ for different τ at $f = 0.5f_D$, $f_B/f_s = 5\%$ | 53 |
| | | |
| 3.1 | Dual pOCTii SPDA camera system. | 60 |
| 3.2 | Setup of the HDGV measurement system of the rotating disk experiment. | 62 |
| 3.3 | Close up of the Doppler camera system. | 62 |
| 3.4 | Top: Velocity distribution of the measured projected velocity of the rotating disk. Bottom: Standard deviation of the measurement. | 63 |
| 3.5 | Top: Comparison of the measured and the true velocity of the rotating disk. Bottom: Error of the velocity measurement. | 64 |
| 3.6 | Setup of the buoyant plume experiment. | 65 |
| 3.7 | Velocity map of the measured projected velocity of the buoy- ant plume. | 66 |
| 3.8 | Setup of the simultaneous ILDV and PIV measurement. | 69 |
| 3.9 | Close up of the illumination of the simultaneous ILDV and PIV measurement. I_1, I_2 : Illuminating laser beams, BS: Beam Splitter, M: Mirrors, CL: Cylindrical lenses. | 69 |
| 3.10 | Measured velocity distribution of the jet using ILDV. | 70 |
| 3.11 | Comparison of the ILDV and the PIV Measurements at a crosssection of $z = 14$ mm. | 71 |
| 3.12 | Convergence of the measured velocity to its mean. | 72 |
| 3.13 | Comparison of ILDV and PIV using the pOCTii and the HSC. | 73 |

| | | |
|------|-------------------------------------------------------------------------------------------------------------------------------------------------------------------------------------------------------------------------|----|
| 3.14 | Setup of the rotating disk experiment. T: Telescope, BS: Beam splitter, EOM: Electro optic modulator, M: Mirrors. | 74 |
| 3.15 | Close up on the rotating disk. | 75 |
| 3.16 | Measured z-component of the velocity of the rotating disk. | 75 |
| 3.17 | Top: Comparison of the measured and the true velocity of the rotating disk. Bottom: Error of the velocity measurement. | 76 |
| 3.18 | Setup of the in-plane velocity measurement of a turbulent jet in water. T: Telescope, BS: Beam splitter, EOM: Electro optic modulator, M: Mirrors, CL: Cylindrical lens, HSC: High speed camera. | 78 |
| 3.19 | Close up on the water tank setup of the in-plane velocity measurement. | 79 |
| 3.20 | Measured instantaneous velocity distribution of the turbulent jet using ILDV with 128 consecutive images. | 80 |
| 3.21 | Measured mean velocity distribution of the turbulent jet using ILDV. | 80 |
| 3.22 | Measured instantaneous velocity distribution of the turbulent jet using PIV. | 81 |
| 3.23 | Measured mean velocity distribution of the turbulent jet using PIV. | 82 |
| 3.24 | Comparison between the measured mean velocities between ILDV and PIV along $x = 27$ mm. | 83 |
| 3.25 | Comparison between the measured instantaneous velocities using ILDV and PIV along $x = 27$ mm. | 83 |
| 3.26 | Setup of the out-of-plane velocity measurement of a turbulent jet in water. | 84 |
| 3.27 | Measured mean out-of-plane velocity distribution of the turbulent jet using ILDV. | 84 |
| 3.28 | Measured instantaneous out-of-plane velocity distribution of the turbulent jet using ILDV with 128 consecutive images. | 85 |
| 3.29 | Combined ILDV and PIV measurement of the mean flow velocities. | 86 |
| 3.30 | Comparison between the SPDA-algorithm, the Hilbert transform based algorithm and PIV along $x = 27$ mm with $\tau = 1/f_s$ for a measurement series with 8 consecutive images and 512 independent realizations. | 87 |
| 3.31 | Comparison between the SPDA-algorithm, the Hilbert transform based algorithm and PIV along $x = 27$ mm with $\tau = 4/f_s$ for a measurement series with 8 consecutive images and 512 independent realizations. | 88 |

| | | |
|------|-----------------------------------------------------------------------------------------------------------------------------------------------------------------------------------------------------------------------------------------------------------|----|
| 3.32 | Comparison between the SPDA-algorithm, the Hilbert transform based algorithm with a different high pass filter and PIV along $x = 27$ mm with $\tau = 4/f_s$ for a measurement series with 8 consecutive images and 512 independent realizations. | 89 |
| 3.33 | Convergence of the autocorrelation of the SPDA-algorithm and the Hilbert transform based algorithm to their respective mean for a single point in the flow field and different ordering of the samples. | 89 |
| 3.34 | Comparison between the SPDA-algorithm, the Hilbert transform based algorithm and PIV along $x = 27$ mm with $\tau = 1/f_s$ for a measurement series with 128 consecutive images. | 90 |
| 3.35 | Comparison between the SPDA-algorithm, the Hilbert transform based algorithm and PIV along $x = 27$ mm with $\tau = 4/f_s$ for a measurement series with 128 consecutive images. | 91 |
| 3.36 | Comparison between the resulting velocities for a Fourier analysis applied on the data set with 128 consecutive images and PIV. | 91 |
| 3.37 | Typical signal measured with the high speed camera. | 92 |
| 3.38 | “Instantaneous” PSD of the signal measured with the high speed camera. | 92 |
| 3.39 | Instantaneous in-plane velocity distribution of the turbulent jet using ILDV with spatial autocorrelations calculated using 8 consecutive images on a 16×16 pixel neighborhood. | 93 |
| 3.40 | Comparison between the data analysis techniques using temporal and spatial correlations and PIV. | 94 |
| 3.41 | Relative convergence to its mean of the different autocorrelation based data analysis techniques. | 95 |

List of Tables

| | | |
|-----|-----------------------------------------------------------------------------------------------|----|
| 2.1 | Performance examples of the Photron FASTCAM SA5 and the Vision Research Phantom v711. | 29 |
| 3.1 | Specifications of the Coherent Verdi V5. | 56 |
| 3.2 | Specifications of the frequency shifting system. | 58 |
| 3.3 | Specifications of the Photron Fastcam Ultima 512. | 58 |
| 3.4 | Specifications of the pOCTii sensor. | 59 |

Nomenclature

Roman symbols

| | |
|---------------|--------------------------------------------------------------|
| A_i | Amplitude |
| c | Speed of light |
| C | Complex signal |
| CL | Cylindrical lens |
| d | Separation distance between the light sheet optics |
| E_i | Electromagnetic field |
| Δf | Frequency spacing |
| f | Signal frequency |
| f_B | FWTM frequency broadening |
| f_D | Demodulation frequency of the pOCTii |
| $F_{Hilbert}$ | Hilbert filter |
| F_{HP} | High pass filter |
| f_{max} | Maximum occurring signal frequency |
| f_{min} | Minimum occurring signal frequency |
| f_s | Sampling frequency |
| h | Thickness of the light sheet |
| I | In-phase component of the lock-in detection |
| \vec{I}_i | Illumination direction |
| L | Distance of the measurement area from the light sheet optics |
| l | Length of the measurement volume |
| l_c | Coherence length of the light source |
| M | Number of independent realizations |
| N | Number of periods of the lock-in process |
| N_p | Number of signal periods a particle generates |
| N_{part} | Number of particles |
| N_f | Number of consecutive recorded images in a camera |
| N_p^{min} | Minimum number of signal periods a particle has to generate |
| N_T | Total number of acquired images |
| \vec{O} | Observation Direction |
| Q | Quadrature component of the lock-in detection |
| $R(\tau)$ | Continuous autocorrelation |
| $r(k)$ | Discrete autocorrelation |

| | |
|----------------|-------------------------------------------------------|
| S | Doppler signal |
| S_{AC} | Modulated part of the Doppler signal |
| S_{DC} | Unmodulated part of the Doppler signal |
| S_i | Sampled Doppler signal |
| S_i^{AC} | Zero mean sampled signal |
| S_i^a | sampled zero mean analytic signal |
| \hat{S}_k | Spectral components of the signal S |
| s | Probe volume size |
| s_{min} | Minimum probe volume size |
| S_ϕ | Phase sensitivity |
| T | Telescope |
| Δt | Sampling interval |
| t_m | Particle arrival time |
| T_t | Transit time |
| T_{qp} | Integration time of the pOCTii sensor |
| $V(t)$ | Voltage applied to the EOM |
| \vec{V} | Velocity |
| v_{max} | Maximum occurring flow velocity |
| $W(f_k) = W_k$ | PSD of a signal |
| $W^a(f)$ | PSD of the analytic signal filter |
| $W_F(f)$ | PSD of the entire filter |
| $W_H(f)$ | PSD of the Hilbert filter |
| $W_H^i(f)$ | PSD of the Hilbert filter calculated with i samples |
| $W_{HP}(f)$ | PSD of the high pass filter |
| X, Y | Size of the measurement volume |

Greek symbols

| | |
|-------------------|---------------------------------------------------------------|
| α | Observation angle of the camera |
| δ | Peak shift |
| ϵ | Bias error |
| ϕ_i | Signal phase |
| λ_0 | Center wavelength of the light source |
| $\mu = \mu(W(f))$ | Mean of the PSD |
| ν | Frequency of light |
| ν_0 | Center frequency of the light source |
| ν_d | Doppler shift |
| ν_D | Difference between the Doppler shifts in the dual beam method |
| ν_D^{max} | Maximum occurring Doppler frequency |
| ν_i | Doppler shift for illumination direction i |
| ν_s | Shift frequency |

| | |
|----------------|----------------------------------------------------|
| $\hat{\nu}$ | Estimated signal frequency |
| $\vec{\Sigma}$ | Sensitivity vector |
| Σ | Length of the sensitivity vector |
| Σ^{opt} | Optimum sensitivity |
| τ | Time delay in the autocorrelation |
| θ | Crossing angle between the illumination directions |

Abbreviations

| | |
|------------------------|----------------------------------------------|
| BS | Beam splitter |
| DFT | Discrete Fourier transform |
| DVS | Dynamic Vision Sensor |
| EOM | Electro optic modulator |
| fps | Frames per second |
| FWTM | Full width tenth maximum |
| HDGV | Heterodyne Doppler global velocimetry |
| HSC | High speed camera |
| ISIS | In-situ Storage Image Sensor |
| ILDV | Imaging laser Doppler velocimetry |
| LDV | Laser Doppler velocimetry |
| M | Mirror |
| Mfps | Million frames per second |
| <i>OPD</i> | Optical path length difference |
| <i>OPL_i</i> | Optical path lengths |
| PIV | Particle image velocimetry |
| pOCTii | Parallel optical coherence tomography imager |
| PSD | Power spectral density |
| SPDA | Smart pixel detector array |

Others

| | |
|---------------|------------------|
| \mathcal{F} | Fourier operator |
| \mathcal{H} | Hilbert operator |

1 Introduction

Measuring the velocity distribution in a flow is one of the main objectives in flow diagnostics. Over the years, many different single point measurement techniques have been developed. Among these are pressure and hot wire probes which require a probe inside the flow, but also non-intrusive techniques like multi-component laser Doppler velocimeters (LDV). These techniques usually allow to measure the velocity with a low uncertainty and good temporal resolution but only at a single point.

For a complex flow field, such as the turbulent flow around a model in a wind tunnel, the knowledge of the flow velocity in a single point does not reveal a lot about the flow topology. For a distributed measurement of the flow field those single point probes need to scan the region of interest and therefore only allow to measure the mean flow field. In many situations, however, it is necessary to measure the instantaneous velocity distribution to fully understand the flow phenomena.

For this purpose different planar measurement techniques have been developed, which allow to measure the velocity distribution in a plane. The most prominent technique among these is Digital Particle Image Velocimetry (PIV, [Willert et al., 1991](#)). In PIV the displacement of tracer particles that are mixed into the flow is measured by illuminating a plane with a light sheet twice within a very short time and recording the particle positions with a suitable camera. The velocity distribution is then extracted by determining the displacements of particle clusters using cross-correlations. As this techniques measures the displacement of particles, it is necessary that those particles move within the illuminated plane, and therefore also only the in-plane velocity components can be measured. Extensions of these planar techniques that allow to measure all three velocity components in a plane exist, such as Stereo PIV ([Arroyo et al., 1991](#)) or Dual Plane PIV ([Raffel et al., 1996](#)). But apart from the complex setups and calibration required in these techniques, the out-of-plane velocity component usually suffers from an uncertainty which is an order of magnitude larger than the uncertainty of the in-plane components ([Prasad et al., 1993](#)). The displacement-based techniques have also been expanded to measure the velocity distribution in a whole volume. In Tomographic PIV ([Elsinga et al., 1994](#)) and Tomographic Particle Tracking Velocimetry ([Maas et al., 1993](#)) several cameras are used for a 3-D reconstruction of the particle distribution.

The common problem of all those particle displacement based techniques is that they require to resolve the seeding particles in the flow to be able to detect their displacements. This limits those techniques to measurement areas of less than one square meter, as especially in gaseous flows micron sized particles have to be detected. Therefore only few attempts have been made to apply these techniques to large facilities (Resagk et al., 2000).

A different family of planar velocity measurement techniques uses the Doppler shift in the frequency of the light scattered from moving particles and therefore does not rely on the displacement of particles. By measuring the frequency shift of light and not the position of the scattering particles, these Doppler based techniques avoid the restriction of the need to resolve the tracer particles and are therefore suited to measure larger areas. The Doppler shifts are usually very small compared to the frequency of light and therefore difficult to detect. In Doppler Global Velocimetry (DGV) molecular line filters are used to convert the frequency shift into a change in intensity (Ainsworth et al., 1997; Elliott et al., 1999; Samimy et al., 2000). The technique has been successfully applied in full scale wind tunnels (Beutner et al., 1998), high-speed flows (Smith et al., 1996) and combustion measurements (Roehle et al., 2000). Molecular line filters can also be used to change the Doppler frequency shift into a phase shift as it is done in near resonant interferometry (Landolt et al., 2009) to measure velocity distributions. However, those methods usually suffer from uncertainties in the order of a few m/s (Elliott et al., 1999) and are therefore only suited to high speed flows.

In this work we present another approach to measure planar velocity distributions using the Doppler shift of scattered light which is well known for single point measurements: In reference beam LDV (Y. Yeh et al., 1964) and in dual-beam LDV (vom Stein et al., 1969) the Doppler shift is demodulated using a process called optical heterodyning, yielding a signal with a beat frequency that is in a technically accessible range. An extension of dual-beam ILDV to measure velocities along a line has been presented by Czarske et al. (2002). However these two techniques can also be extended into planar measurement techniques by using light sheets instead of laser beams to illuminate the particles and 2-D detector arrays to detect the distributed signals. With different light sheet configurations either the out-of-plane or one of the in-plane components of the velocity can be measured. The present work therefore starts with a brief description of the physical basics of the signal formation process and then focuses on the planar extension of the technique and the requirements on the detector system for the distributed measurement. In the measurement section the different planar extensions and different detector systems are introduced to measure velocity distributions, assessing the potential of this new technique.

2 Method

Imaging Laser Doppler Velocimetry (ILDV) and Heterodyne Doppler Global Velocimetry (HDGV) can be considered as the planar extensions of the well known laser Doppler velocimetry (LDV) point measurement technique. They therefore share the same physical principles which are briefly recalled based on the theory presented in the book “Laser Doppler and Phase Doppler Measurement Techniques” (Albrecht et al., 2003). Based on the two most commonly used LDV setups, the reference beam LDV and the dual-beam LDV, the necessary steps to expand the technique from a point measurement technique to a planar measurement technique are described in the following sections. This includes the expansion of the illumination to generate a planar measurement volume, the requirement on the camera systems to detect the Doppler signal and the data analysis techniques that can be used to determine the flow velocity.

2.1 Signal Formation

2.1.1 Doppler Effect

The frequency ν of light scattered from an illuminated moving particle is shifted proportional to its velocity according to the Doppler equation (Eq. 2.1).

$$\nu - \nu_0 = \nu_d = \frac{\nu_0}{c} (\vec{O} - \vec{I}) \cdot \vec{V} \quad (2.1)$$

The Doppler frequency shift ν_d depends on the magnitude and direction of the velocity \vec{V} of the scattering particle, the frequency ν_0 and the direction the illumination \vec{I} , the direction of observation \vec{O} where the detector is placed, and the speed of light c . Figure 2.1 shows the geometry of this scattering process indicating the orientation of the vectors of Eq. 2.1.

As the Doppler shift ν_d is a scalar also only one component of the velocity can be measured, namely the component into the direction of $\vec{O} - \vec{I}$. Furthermore, using the Doppler shift to measure the velocity of a fluid flow is an indirect technique, as the velocity of the scattering particles within the flow is measured.

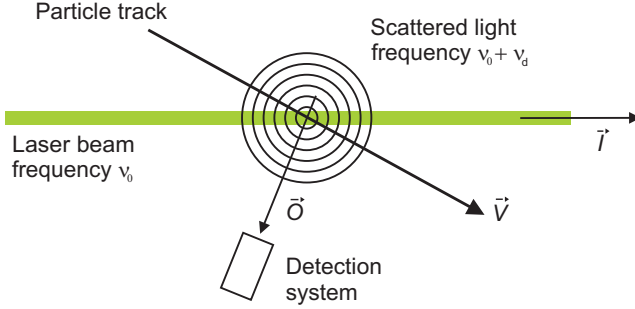


Figure 2.1: Geometry of the scattering process.

2.1.2 Optical Heterodyning

The Doppler frequency shift is on the order of several MHz per m/s of flow velocity. Compared to the frequency of light, which is on the order of around 100 THz, it is very small and therefore virtually impossible to detect directly. Using a process called optical heterodyning, the small frequency shifts can be extracted by mixing the scattered electromagnetic light wave from the particle with a second light wave on the detector. This can be either a reference wave, as it is done in reference beam LDV (Y. Yeh et al., 1964) or a second scattered wave from the particle, as in dual-beam LDV (vom Stein et al., 1969).

The light wave scattered from the particle can be modelled by a non-polarized planar wave:

$$E_{Sig} = A_{Sig} e^{2\pi j[(\nu_0 + \nu_d)t + \phi_{Sig}]} \quad (2.2)$$

Where E_{Sig} is the electromagnetic field, A_{Sig} the amplitude of the wave, ν_0 the frequency of the illumination source and ϕ_{Sig} a random phase shift of the scattered light which can be assumed constant during the scattering process. In the reference beam method this scattered wave is mixed with a reference wave from the same coherent light source which can be modeled identically:

$$E_{Ref} = A_{Ref} e^{2\pi j[\nu_0 t + \phi_{Ref}]} \quad (2.3)$$

A_{Ref} denotes the amplitude of the reference wave and ϕ_{Ref} a random but constant phase shift. Those two waves are then mixed on the detector

$$E = E_{Ref} + E_{Sig}. \quad (2.4)$$

Due to interference between the two waves E_{Sig} and E_{Ref} the observable signal S , i.e. the intensity of the mixed signal, becomes

$$S = \epsilon c \langle E^2 \rangle = \epsilon c E E^* \quad (2.5)$$

$$S = A_{Ref}^2 + A_{Sig}^2 + 2A_{Ref}A_{Sig} \cos(2\pi\nu dt + \phi), \quad (2.6)$$

where ϵ is the electric constant. The multiplicative pre-factor ϵc has been omitted for simplicity in Eq. 2.6. This Doppler signal S has a constant offset of $A_{Ref}^2 + A_{Sig}^2$ and is modulated by ν_d , the frequency of the Doppler shift. Additionally the signal has a random phase shift ϕ which can be assumed constant during the scattering process. The offset is usually large compared to the amplitude of the modulated part, as A_{Sig} is much smaller than A_{Ref} . The magnitude of the Doppler shift and the measured velocity component depend on the geometrical arrangement of the illumination and the detector with respect to each other and on the frequency ν_0 of the light source. Looking at the Doppler equation (Eq. 2.1) these dependencies can be collected into a sensitivity vector $\vec{\Sigma}$:

$$\vec{\Sigma} = \frac{\nu_0}{c} (\vec{O} - \vec{I}) \quad (2.7)$$

The direction of $\vec{\Sigma}$ is the sensitive direction of the measurement technique and its length $\Sigma = |\vec{\Sigma}|$ gives the magnitude of the signal frequency for a given velocity.

For an imaging technique the dependence of $\vec{\Sigma}$ on the observation direction severely limits the measurement range, as will be shown in Sec. 2.2.1. This dependence can be avoided by using a second scattered wave from the flow scene for the mixing process instead of the reference wave, as it is done in dual-beam LDV. Here the particle is illuminated from two different directions \vec{I}_1 and \vec{I}_2 as shown in Fig. 2.2. The light scattered from the particle into the direction \vec{O} exhibits two different Doppler shifts ν_1 and ν_2 for the two different illumination directions:

$$\nu_1 = \frac{\nu_0}{c} (\vec{O} - \vec{I}_1) \cdot \vec{V} \quad (2.8)$$

$$\nu_2 = \frac{\nu_0}{c} (\vec{O} - \vec{I}_2) \cdot \vec{V} \quad (2.9)$$

The two scattered electromagnetic waves can again be modeled as

$$E_1 = A_1 e^{2\pi j[(\nu_0 + \nu_1)t + \phi_1]} \quad (2.10)$$

and

$$E_2 = A_2 e^{2\pi j[(\nu_0 + \nu_2)t + \phi_2]}. \quad (2.11)$$

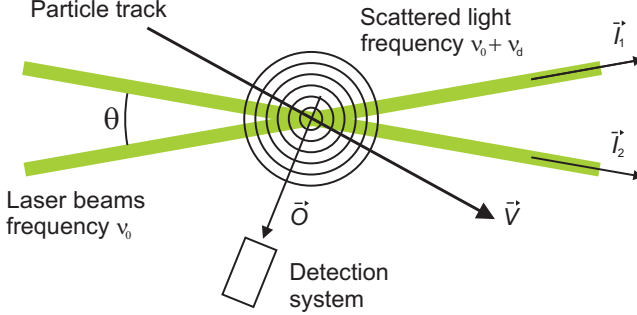


Figure 2.2: Geometry of the scattering process for a dual beam illumination.

A_1 and A_2 are the amplitudes of the two waves and ϕ_1 and ϕ_2 two random phase shifts. Since the two waves are scattered in the same direction \vec{O} they are automatically mixed on the detector and the observable signal S results to

$$S = A_1^2 + A_2^2 + 2A_1A_2 \cos(2\pi(\nu_1 - \nu_2)t + \phi). \quad (2.12)$$

The signal S has again an offset of $A_1^2 + A_2^2$ and is now modulated with the difference $\nu_1 - \nu_2$ between the two Doppler shifts. The offset is, compared to the reference beam method, much smaller. Since A_1 and A_2 are about equal, the offset is on the same order of magnitude as the amplitude of the modulated part of the signal $2A_1A_2$. Using Eqs. 2.8 and 2.9 the difference $\nu_1 - \nu_2$ can be rewritten as

$$\nu_D = \nu_1 - \nu_2 = \frac{\nu_0}{c} (\vec{I}_2 - \vec{I}_1) \cdot \vec{V} \quad (2.13)$$

The measured frequency ν_D no longer depends on the direction of observation \vec{O} but on the arrangement of \vec{I}_1 and \vec{I}_2 .

Similar to the reference beam method a sensitivity vector $\vec{\Sigma}$ can be introduced:

$$\vec{\Sigma} = \frac{\nu_0}{c} (\vec{I}_2 - \vec{I}_1) \quad (2.14)$$

Its length $\Sigma = |\vec{\Sigma}|$ again describes the conversion factor between velocity and measured frequency and its direction the direction of the measured velocity component. Eq. 2.13 can be further simplified, by using the crossing angle θ between \vec{I}_1 and \vec{I}_2 and the velocity component v_\perp , to

$$\nu_D = \frac{2 \sin\left(\frac{\theta}{2}\right)}{\lambda_0} v_\perp. \quad (2.15)$$

λ_0 denotes the wavelength of the illumination light source and v_{\perp} is the component of the velocity \vec{V} into the direction of $\vec{\Sigma}$. The sensitivity of the system can be changed by changing the angle θ between \vec{I}_1 and \vec{I}_2 . Moreover the measured velocity component only depends on the illumination directions and no longer on the direction of observation. Thus the sensitivity is now decoupled from the placement of the detector. This is especially important when expanding this measurement principle to an imaging technique with a planar measurement volume, as it will be shown in Sec. 2.2.2.

2.1.3 Directional Ambiguity

The Doppler signal S measured using the reference beam method (Eq. 2.6) and the dual-beam method (Eq. 2.12) both lack the sense of the direction of \vec{V} along the sensitivity vector $\vec{\Sigma}$. Moreover particles that do not move do not generate a signal at all. The Doppler equation itself allows for negative and positive Doppler shifts ν_d depending on the direction of \vec{V} projected onto $\vec{\Sigma}$. The directional sensitivity is lost due to the optical heterodyning. The Doppler shift ν_d and the difference of the two Doppler shifts ν_D both appear inside a cosine function in the signal S . Since the cosine function is an even function, i.e. $f(x) = f(-x)$, the sense of direction is lost. This sensitivity can be regained by pre-shifting the frequency of the reference beam E_{Ref} in the reference beam method or one of the two illumination beams E_1 or E_2 in the dual beam method by a known frequency shift ν_s :

$$E_{Ref} = A_{Ref} e^{2\pi j[(\nu_0 + \nu_s)t + \phi_{Ref}]} \quad (2.16)$$

$$E_1 = A_1 e^{2\pi j[(\nu_0 + \nu_1 + \nu_s)t + \phi_1]} \quad (2.17)$$

The signal S resulting for the two methods is:

$$S = A_{Ref}^2 + A_{Sig}^2 + 2A_{Ref}A_{Sig} \cos(2\pi(\nu_d + \nu_s)t + \phi) \quad (2.18)$$

$$S = A_1^2 + A_2^2 + 2A_1A_2 \cos(2\pi(\nu_D + \nu_s)t + \phi). \quad (2.19)$$

S has now a frequency offset of ν_s : Particles that do not move generate a signal that is modulated by ν_s . Particles that move along $\vec{\Sigma}$ generate a signal with a frequency that is higher than ν_s and particles that move in the opposite direction generate a signal with a lower frequency than ν_s as long as ν_d or ν_D are smaller than ν_s . If ν_d or ν_D are larger, again $\nu_d + \nu_s$ becomes negative and this information is lost due to the cosine function. This pre-shifting can be done using either Bragg cells, a rotating Bragg grating or an electro optic modulator (EOM) as it will be shown in Sec. 2.2.3.

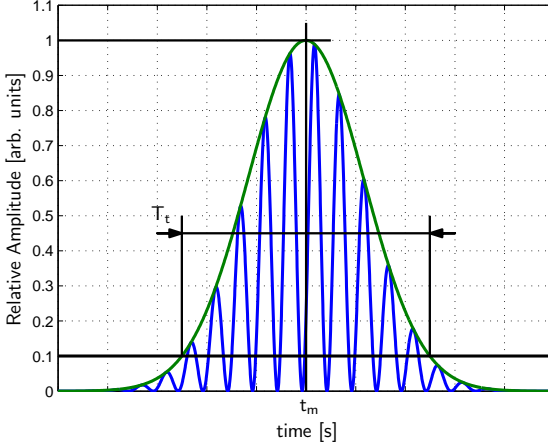


Figure 2.3: Finite signal duration of a particle passing through the probe volume.

2.1.4 Finite Signal Duration

The signals described by the Eqs. 2.18 and 2.19 are both infinitely long modulated signals. In reality only particles that do not move generate an infinitely long signal. Moving particles will pass through the probe volume and therefore generate a signal with a finite duration depending on their velocity, the probe volume size and their trajectory through the probe volume. Using a Gaussian distribution to model the time dependence of the light intensity scattered by a particle during its passage through the probe volume, the measured signal S becomes

$$S = e^{-\frac{4 \ln 10}{T_t^2} (t-t_m)^2} (A_1^2 + A_2^2 + 2A_1 A_2 \cos(2\pi(\nu_D + \nu_s)t + \phi)). \quad (2.20)$$

T_t is the transit time of the particle through the probe volume and t_m is the time, when the maximum scattering intensity is reached, as shown in Fig. 2.3 for a signal with $A_1 = A_2 = 1$ and $T_t = 10/(\nu_D + \nu_s)$ and its Gaussian envelope. The 10 signal periods with an amplitude larger than 10% of the maximal signal amplitude are contained within the time interval of T_t . Therefore T_t is the so called full width tenth of maximum (FWTM) value of the Gaussian distribution.

The number of periods N_p a particle generates is given by

$$N_p = T_t \left(\nu_s + \vec{\Sigma} \cdot \vec{V} \right) = \frac{s\nu_s}{|\vec{V}|} + \vec{\Sigma} \cdot \frac{\vec{V}}{|\vec{V}|} s, \quad (2.21)$$

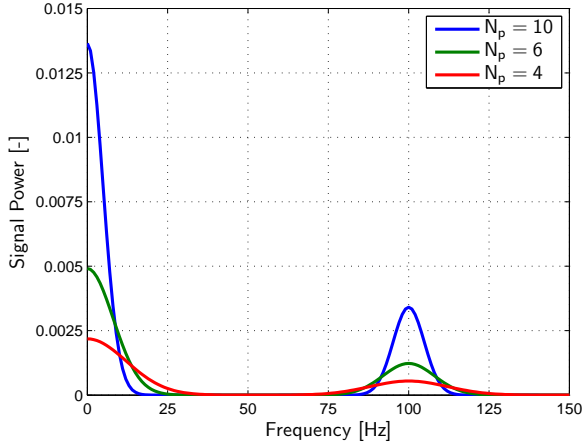


Figure 2.4: Peak broadening of the PSD due to the finite particle passage time.

where s is the size of the probe volume. N_p can be split up in two parts: The first part describes the number of signal periods generated due to the pre-shift ν_s . The faster a particle moves through the probe volume the fewer signal periods will be generated due to the pre-shift. The second term describes the influence of the sensitivity and the direction of motion of the particle with respect to the direction of the sensitivity. If a particle moves perpendicular to $\vec{\Sigma}$, it will not generate any Doppler signal and only the frequency of the pre-shift ν_s will be measured. If the particle moves in the direction of $\vec{\Sigma}$ the number of periods is increased and if it moves in the opposite direction the number of periods is decreased. Both terms also depend on s . The larger the probe volume is, the longer becomes the passage time and the more signal periods will be generated, unless $\nu_s = 0$ and \vec{V} is perpendicular to $\vec{\Sigma}$.

The influence of the finite signal duration on the signal quality can also be analyzed in the frequency domain. Figure 2.4 shows the power spectral density (PSD) of three different signals with $A_1 = A_2 = 1$ and a frequency $\nu_D + \nu_s = 100$ Hz and $N_p = 4, 6$ and 10 . An infinitely long signal is not shown. It would be a single peak at 100 Hz with an infinite amplitude. The peaks of the finite signals are clearly broadened and the amplitudes reduced as N_p is decreased. The FWTM broadening f_B is inversely proportional to

the transit time:

$$f_B = \frac{2\sqrt{2} \ln 10}{\pi} \frac{1}{T_t} \approx \frac{2}{T_t} \quad (2.22)$$

A signal with 10 periods therefore has a FWTM frequency bandwidth of 20%. For some signal processing algorithms this peak broadening also leads to a biased frequency estimation as will be shown in Sec. 2.4.

2.1.5 Multiple Particle Scattering

In a single point LDV usually signal bursts, generated by a single particle passing through the probe volume, are analyzed to measure the velocity. For an imaging technique a more continuous signal is needed, as in a camera all pixels are usually sampled simultaneously and the recording time is limited. A continuous signal can be achieved by a higher seeding particle density and leads to a situation where several particles scatter the light at the same time in the probe volume that is imaged onto the detector. The resulting signal is a superposition of N individual signals S_i described by Eq. 2.20 with different random phases ϕ_i and arrival times ${}_i t_m$ in the probe volume. Assuming that the scattering intensities ${}_i A_j$ are all equal and neglecting the transit time differences the resulting signal becomes:

$$S = \sum_{i=1}^N (2A^2 + 2A^2 \cos(2\pi(\nu_D + \nu_s)t + \phi_i)) \quad (2.23)$$

This signal can be split up in two parts: The unmodulated part S_{DC}

$$S_{DC} = \sum_{i=1}^N 2A^2 = 2NA^2 \quad (2.24)$$

and the modulated part S_{AC}

$$S_{AC} = 2A^2 \sum_{i=1}^N \cos(2\pi(\nu_D + \nu_s)t + \phi_i). \quad (2.25)$$

While the unmodulated part grows linearly with the number of scattering particles, the amplitude of the modulated part depends on the random phases ϕ_i . Since the detector has to be able to resolve the modulated part in the presence of the unmodulated part, the visibility

$$\gamma = \frac{S_{AC}}{S_{DC}} \quad (2.26)$$

of the signal is a measure of the signal quality. The theoretical analysis of the signal S (Eq. 2.23) is not trivial, therefore its analyzed numerically.

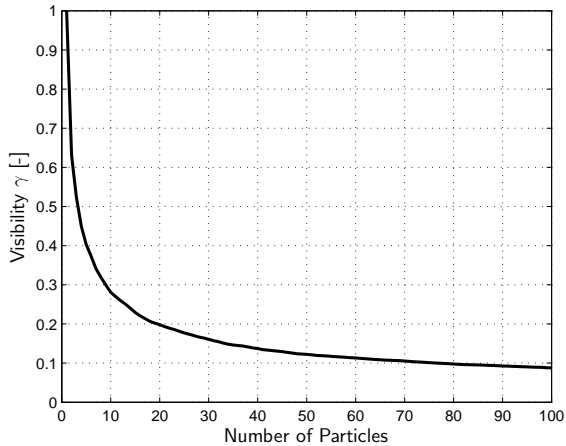


Figure 2.5: Visibility of the Doppler signal.

Figure 2.5 shows the visibility as a function of the number of particles averaged over 1000 realizations to eliminate the influence of the random phases. For a single particle $\gamma = 1$. The visibility drops as the number of particles increases in the probe volume. With 100 particles the visibility remains larger than 8%. Thus with a dynamic range of only 8-bits the signal should remain detectable and it is possible to increase the particle density to increase the signal intensity, without losing the visibility. Of course this only applies to the dual-beam setup, as in the reference beam setup the offset generated by the reference beam is usually much larger than the modulated part of the signal, leading to a much lower visibility.

2.2 Planar Extension

The two demodulation techniques described in Sec. 2.1.2 are commonly used in point measurement techniques. Both techniques can be extended into planar imaging measurement techniques where the velocity distribution in a plane is measured, using different light sheet configurations and suitable cameras. The main points that have to be considered for the planar extensions are:

- How to create a measurement plane with the required illumination properties.

- How to achieve the optical mixing.
- Which velocity component can be measured.
- How to reduce the sensitivity Σ to achieve a Doppler signal with frequencies that can be detected with a camera, while still maintaining a sharp image,
- How to set up a system for a given flow scenario to obtain a signal with enough signal periods N_p .
- And since optical heterodyning is an interferometric detection method, what coherence length l_c is needed.

The 2-D extensions of the measurement volume and their impact on the imaging task and the camera systems will be described in the next two sections for each heterodyning technique separately. The impact of the planar extension on the setup and the requirements on l_c are subsequently discussed in separate sections.

2.2.1 Reference Beam Method

In reference beam LDV the measurement volume is defined by the cross section between the illuminating laser beam, which is focussed at the point of interest and the observation direction. To expand this into a planar measurement technique is straightforward. A schematic of such a setup is shown in Fig. 2.6. Instead of illuminating the flow with a single laser beam, it is illuminated by a light sheet using a long coherence laser as a light source. The light, scattered from the particles in the flow field, is recorded using a camera system with a 2-D detector array instead of a single detector. From the laser part of the light, around 5%, is split off using a beam splitter. This reference beam is redirected to the camera, where it is mixed with the light imaged from the flow scene on the 2-D detector array. The mixing can be done e.g. using a beam splitter between the lens and the detector array. Each pixel of the 2-D detector array therefore simply acts as an individual single point reference beam LDV.

The measured signal frequency is, as shown in Sec. 2.1.2, directly the Doppler shift ν_d and depends on the arrangement between the illumination direction \vec{I} and the observation direction \vec{O} . For an imaging technique this dependence is quite important and, as previously mentioned, restrictive: An imaging task usually requires that the observation direction is perpendicular to the object plane as shown in Fig. 2.7(a). For the Doppler measurement this means that the sensitivity vector $\vec{\Sigma}$ of the system is set

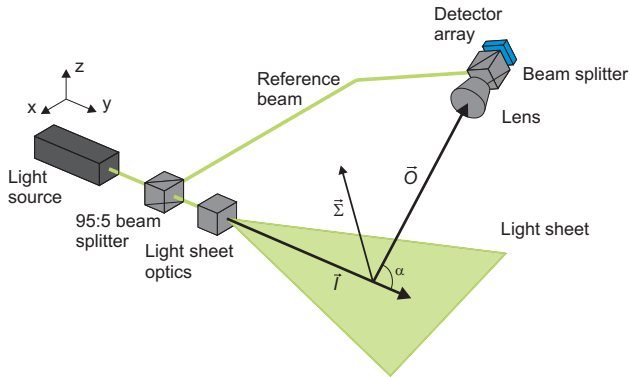


Figure 2.6: Schematic of an imaging reference beam setup.

to a vector 45° out-of-plane. Thus also the measurable velocity component is fixed to this direction. With such a perpendicular arrangement the Doppler frequency, that needs to be detected is in the order of $2 \text{ MHz}/(\text{m/s})$ which is for an imaging task very large – even a camera with a frame rate of 1 Mfps would only allow to measure flow velocities up to 0.25 m/s. It is therefore desirable to reduce the sensitivity of the system by decreasing the angle α between \vec{O} and $\vec{\Sigma}$. The requirement of a perpendicular orientation between the illumination and observation direction can be relaxed using a Scheimpflug optical arrangement. This arrangement allows to acquire a sharp image of a tilted object plane with respect to the camera by tilting and shifting the lens and the detector array of the camera as well. To achieve a sharp image the object plane, the lens plane and the image plane have to intersect in a line as shown in Fig. 2.7(b). With this arrangement α can be decreased and the illuminated plane can be kept in focus. Figure 2.8 shows a checkerboard, imaged with three different observation angles, $\alpha = 90^\circ$, $\alpha = 45^\circ$, and $\alpha = 10^\circ$. Using the Scheimpflug arrangement the image remains sharp over the whole plane for all observation angles. But by increasing α the image becomes increasingly distorted and the spatial resolution in the direction of the tilt is reduced: At the extreme angle of 10° the area of 5×2 squares, that fills the entire image (a) is contained in about 25% of the image. Imaging the checkerboard at even lower observation angles is still possible, but the spatial resolution would

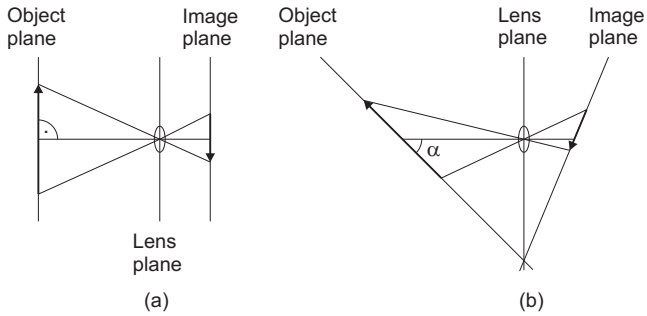


Figure 2.7: Different optical arrangements: (a) Perpendicular arrangement, (b) Scheimpflug arrangement.

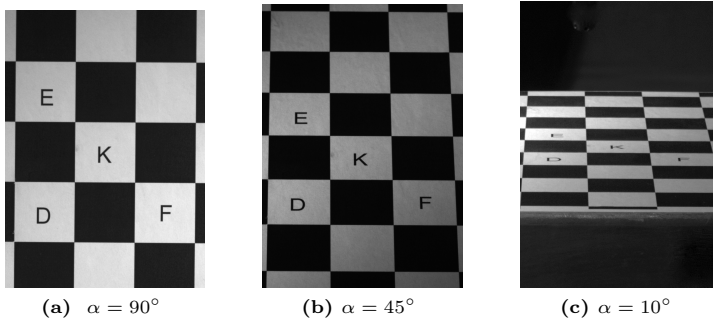


Figure 2.8: Checkerboard imaged with different observation angles α .

be further reduced, until the checkerboard collapses into a line at $\alpha = 0^\circ$. On the other hand the decrease in sensitivity Σ due to the tilt is not very large: Even with an observation angle of 10° Σ is only reduced to approx. 500 kHz/(m/s).

The measured velocity component also depends on the observation angle. By changing the length of $\vec{\Sigma}$ also its direction changes and therefore the measurable velocity component. An independent choice of $\vec{\Sigma}$, the measured component and the measurement plane is not possible. Thus to measure a specific velocity component on a specific measurement plane, it is necessary to record the scattered light from three different directions simultaneously as it is done in DGV (Nobes et al., 2004).

With those limitations from the imaging side and the resulting large frequencies for low particle velocities, the planar extension of the reference beam method is only suitable for very slow flows. In addition the usually large signal offset generated by the reference beam (Sec. 2.1.2) and the resulting reduced visibility of the signal S require a camera with a very high dynamic range.

Due to the similarity in the geometrical properties between DGV and the planar heterodyne detection, the planar extension of the reference beam LDV may be named Heterodyne Doppler Global Velocimetry (HDGV).

2.2.2 Dual Light Sheet Method

As shown in Sec. 2.1.2, the dependence on the observation direction can be avoided by illuminating the particle from two different directions. In dual beam LDV this is accomplished by using two focussed laser beams that intersect at the measurement point. The intersection of the two beams therefore defines the probe volume. To extend this point measurement technique into a planar one, a measurement plane has to be generated, where each point is illuminated from two directions. The planar extension works similar as in HDGV. A schematic of such a setup is shown Fig. 2.9. Instead of using two laser beams, two light sheets are used, and the scattered light is recorded using a camera. The probe volume is now defined by the intersection of those two planes and the area of this intersection that is imaged onto a pixel. Each pixel therefore acts as a single point LDV.

The intersection between two planes is usually only a line. To obtain a planar measurement volume special care has to be taken in the geometrical arrangement between the two planes. Crossing two light sheets to form a measurement plane where each point is illuminated from two directions, can be accomplished in many different ways. They all can be seen as combinations of two basic configurations: The co-planar light sheet configuration, shown in Fig. 2.10, and the crossed light sheet configuration,

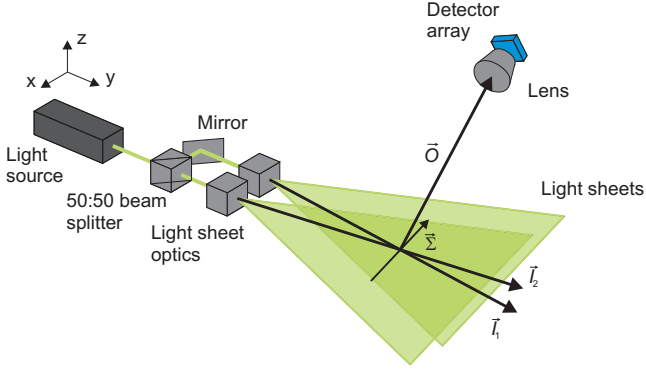


Figure 2.9: Schematic of a dual light sheet setup.

shown in Fig. 2.11.

In the co-planar light sheet configuration both light sheets illuminate the same plane but from two different directions. The measurement volume is therefore given by the volume that is illuminated with both light sheets. With both \vec{I}_1 and \vec{I}_2 within the same illuminated plane, $\vec{\Sigma}$ is within the illuminated plane as well. This configuration therefore allows to measure one of the in-plane components of the velocity.

In the crossed light sheets configuration the two light sheets are oriented such that \vec{I}_1 and \vec{I}_2 are again in the same plane, but the plane of the light sheets is perpendicular to this plane. Usually the cross section between such two planes is a line. But the intersection between the two planes can be expanded from a line into a volume, by using very shallow crossing angles θ and light sheets with a thickness h of several millimeters, as shown in Fig. 2.11. A close up on the cross section between two planes is shown in Fig. 2.12. The measurement volume is a parallelepiped with a rhomboid base area. While the width of the measurement volume is given by the width of the light sheets, its length l depends on θ and on h :

$$l = \frac{h}{\sin(\frac{\theta}{2})} \quad (2.27)$$

The dependence of l on θ for a light sheet thickness of 1 cm is shown in Fig. 2.13. For an angle of 1° the measurement volume is already approx. 60 cm long, and for an even smaller angle of 0.25° it becomes 2 m long. As very shallow crossing angles are used, the parallelepiped that forms the measurement volume becomes very flat and long and its thickness is approximately the thickness of the light sheets used. It therefore can be

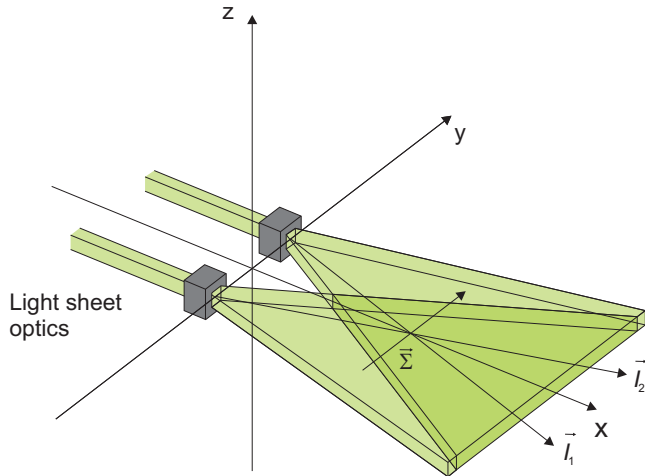


Figure 2.10: Co-planar light sheets setup.

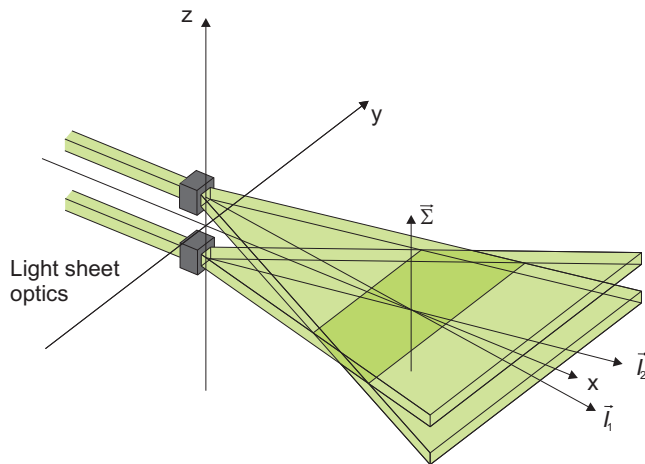


Figure 2.11: Crossed light sheets setup.

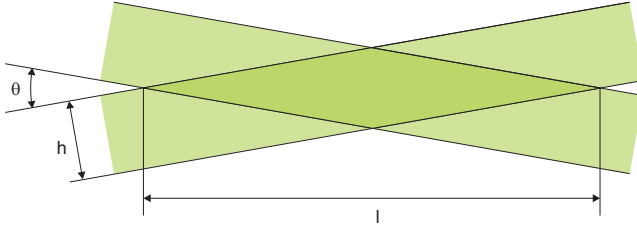


Figure 2.12: Close up on the cross section of the crossed light sheets setup.

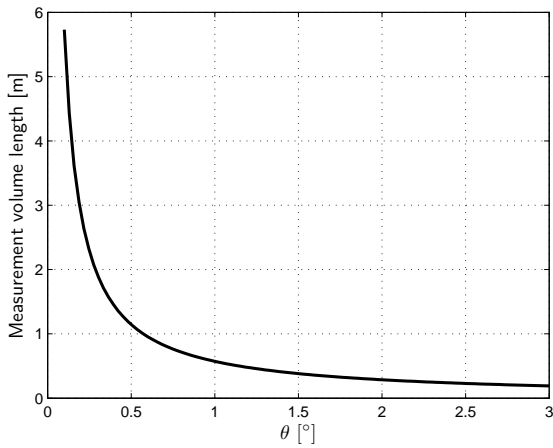


Figure 2.13: Measurement volume length for the crossed light sheets setup.

seen as a light sheet itself. When both \vec{I}_1 and \vec{I}_2 lie within the same plane, $\vec{\Sigma}$ is within this plane as well. As the measurement volume is formed by the intersection between the two light sheets, that are perpendicular to this plane, $\vec{\Sigma}$ is perpendicular to this sheet like measurement volume. Therefore, using this setup, the out-of-plane component of the velocity can be measured.

The length of $\vec{\Sigma}$ depends for both configurations on θ :

$$\Sigma = \frac{2 \sin\left(\frac{\theta}{2}\right)}{\lambda_0} \quad (2.28)$$

As $\vec{\Sigma}$ is independent of \vec{O} there is no limit on reducing θ to very small values and still keeping the whole measurement plane in focus. For a crossing angle of $\theta = 0.3^\circ$ and a wavelength of $\lambda_0 = 532 \text{ nm}$ Σ becomes as low as $10 \text{ kHz}/(\text{m/s})$. However there is a lower limit on θ and on the minimum size of the probe volume s , that is imaged onto a pixel, due to the finite signal duration of a particle crossing the probe volume. This dependence will be analyzed in Sec. 2.2.3 in detail.

Additionally the crossing angle θ varies over the measurement plane in the co-planar setup due to the laser beam fan out. The variation of θ across a rectangular measurement area, is shown in Fig. 2.14. The measurement area is assumed $L = 2 \text{ m}$ away from the light sheet optics and has a side length of $X = Y = 1 \text{ m}$. The two light sheet optics are placed apart at a distance of $d = 10 \text{ mm}$. θ is constant on circles around the light sheet optics and decreases with increasing distance from 0.28° to 0.19° , which leads to a quite strong change in sensitivity Σ . This large change of about 30% in sensitivity obviously needs to be calibrated for a reliable measurement.

In the crossed light sheets setup the crossing angle θ is constant, as long as the light sheets that are used to generate the measurement volume have a constant thickness. However, if their thickness increases or decreases along the light sheet the crossing angle varies as well and a calibration becomes necessary.

As this setup is the imaging extension of the dual-beam LDV, it may be named Imaging Laser Doppler Velocimetry (ILDV).

2.2.3 System Setup

In a very general flow scenario where the velocity distribution in a plane needs to be measured, it is important to know how to set up the parameters of the system to achieve a reliable measurement. Those parameters include the probe volume size s which is the area that is imaged onto single pixel of the detector, the sensitivity $\vec{\Sigma}$ and the sampling frequency f_s of the camera. In such a general flow scenario there is no preferred direction of

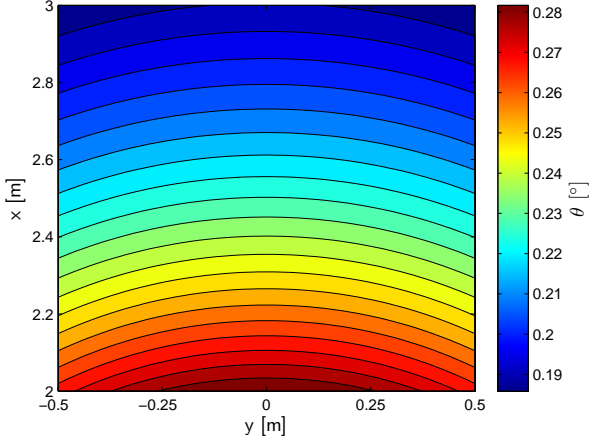


Figure 2.14: Crossing angle variation in the xy-plane of the co-planar light sheet configuration.

the velocity, but the flow can be characterized by the maximum appearing velocity v_{max} . The link between all those parameters of the system is given by the relation of the number of signal periods N_p of the measured signal to the system parameter, as discussed in Sec. 2.1.4:

$$N_p = T_t (\nu_s + \nu_d) = \frac{s\nu_s}{|\vec{V}|} + \vec{\Sigma} \cdot \frac{\vec{V}}{|\vec{V}|} s. \quad (2.29)$$

For a flow situation with no dominant velocity direction the frequency pre-shift is usually set to the center of the measurement range, thus $\nu_s = f_s/4$. The minimum required number of signal periods N_p^{min} is given by the data analysis technique. Also the minimum detectable signal frequency f_{min} is limited by the data analysis technique and the quality of the signal itself. A rather conservative choice as a limit is $f_{min} = 1/8f_s$. With this choice the maximum occurring signal frequency will be limited to $f_{max} = 3/8f_s$ for a flow situation with no dominant velocity direction. Using Eq. 2.29 the limits for the probe volume size s and the sensitivity $\vec{\Sigma}$ for a given flow scenario can be derived, or vice versa the maximum measurable velocity v_{max} for a given optical setup.

In the reference beam method the limiting parameter in the optical setup is the sensitivity $\vec{\Sigma}$ as explained in Sec. 2.2.1. It is therefore interesting to find the maximum measurable velocity v_{max} and the smallest possible probe

volume size s_{min} that can be achieved with such a setup. Using f_{max} the maximum detectable velocity v_{max} can be found as

$$f_{max} = \nu_s + \nu_D^{max} = \frac{3}{8}f_s, \quad (2.30)$$

and

$$\nu_D^{max} = \frac{1}{8}f_s = \Sigma v_{max} \quad (2.31)$$

as the maximum Doppler shift appears for a particle that moves parallel to $\vec{\Sigma}$. Finally v_{max} results to

$$v_{max} = \frac{\nu_D^{max}}{\Sigma} = \frac{f_s}{8\Sigma}. \quad (2.32)$$

Inserting this result into Eq. 2.29 for \vec{V}_{max} along $-\vec{\Sigma}$ gives

$$N_p^{min} = s_{min}\Sigma. \quad (2.33)$$

For a given number of N_p^{min} and $\vec{\Sigma}$ given by the optical setup, the minimum probe volume size s_{min} can be calculated. As Σ is on the order of 1 MHz/(m/s) and N_p^{min} on the order of 5-20, the size of the probe volume limits the measurement system only in microscopic applications where the spatial resolution needs to be better than 10 μm .

In the crossed light sheets method there is no limit on Σ from the imaging task to keep the measurement plane in focus and not to lose the spatial resolution, as shown in Sec. 2.2.2. The limits for the choice of s and Σ are given by v_{max} , f_s and N_p^{min} . The limiting situation for the probe volume size s_{min} is imposed by a particle that moves in the direction of $-\vec{\Sigma}$ through the probe volume and needs to generate N_p^{min} signal periods:

$$N_p^{min} = T_t (\nu_s - \nu_D^{max}) = \frac{s_{min}}{v_{max}} f_{min} \quad (2.34)$$

Solved for s_{min} results in:

$$s_{min} = \frac{N_p^{min} v_{max}}{f_{min}} = 8 \frac{N_p^{min} v_{max}}{f_s}. \quad (2.35)$$

The optimum choice for Σ , that uses the full frequency range, measurable with the camera is easily found:

$$f_{max} = \nu_s + \nu_D^{max} = \frac{1}{4}f_s + \Sigma^{opt} v_{max} = \frac{3}{8}f_s \quad (2.36)$$

$$\Sigma^{opt} = \frac{f_s}{8v_{max}} \quad (2.37)$$

This lower limit on the probe volume size s shows an interesting property of the measurement technique: There is a lower limit on the spatial resolution that can be achieved with a given frame rate of the camera and v_{max} . This limit is independent of Σ and only depends on the velocity of the particle. Thus microscopic applications with spatial resolutions of $1\ \mu\text{m}$ require frame rates of 10^8 fps per m/s of flow velocity. Reversing this argument, by increasing the measurement area also v_{max} can be increased as well and at the same time the Doppler frequency can be easily controlled by reducing Σ . Thus with increasing measurement area higher velocities can be measured with the same camera, as the sensitivity can be reduced. Since the Doppler technique does not require to resolve the position of a single particle this allows to measure large areas that are not possible to measure with PIV/PTV.

2.2.4 Required Coherence Length

Optical heterodyning is a process that relies on interference between the two electromagnetic waves which are mixed on the detector. It is therefore necessary that both waves stem from the same light source and that the optical path length difference OPD of the path of the two electromagnetic waves, from the point where they are split in two separate beams to the point where they are mixed, is within the coherence length l_c of the light source used.

The requirement on l_c is the most severe for HDGV: A schematic of a HDGV setup is shown in Fig. 2.15 indicating the two paths of the electromagnetic waves OPL_1 in blue and OPL_2 in red. The shortest required coherence length for such a setup can be achieved, when the path length of the reference beam is adjusted, such that the optical path length difference of the light recorded from the center of the field of view (FOV) of the camera system and the reference beam is zero, i.e. $OPD = OPL_1 - OPL_2 = 0$. Then the optical path length difference of the points in the corner of the FOV of the camera, depicted by the black rectangle in the schematic, are the largest and in the order of the width of the FOV.

The restrictions on l_c are substantially lower in the ILDV setups. A schematic of a co-planar ILDV setup is shown in Fig. 2.16. The optical path from the scattering particle to the sensor is the same for both electromagnetic waves. If the system is set up such that $OPD = 0$ at the light sheet optics, only the path length difference from the light sheet optics to the particle is relevant. The variation of OPD across the rectangle in Fig. 2.16 is shown in Fig. 2.17 for a generic setup. The rectangle is located at $L = 2\ \text{m}$ away from the light sheet optics and has a side length of $X = Y = 1\ \text{m}$. The two light sheet optics are placed apart at a distance of

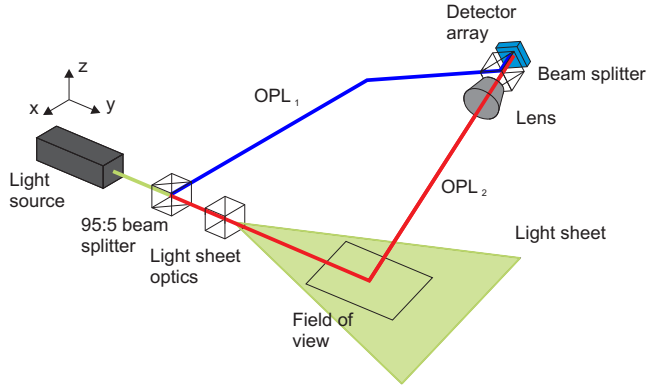


Figure 2.15: Optical paths in the HDGV setup.

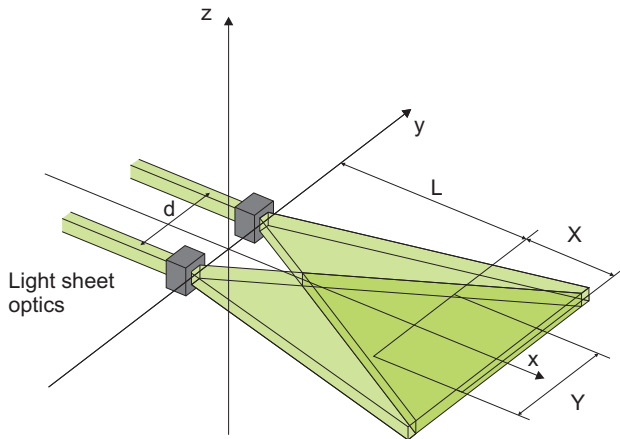


Figure 2.16: Co-planar light sheet setup.

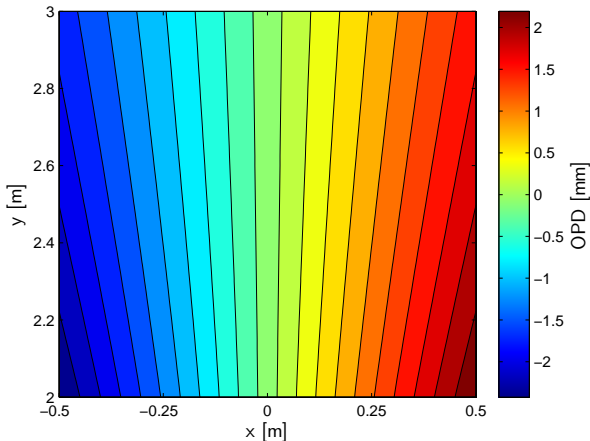


Figure 2.17: *OPD* in the xy -plane of the co-planar light sheet configuration.

$d = 10$ mm. In the center at $x = 0$ the path length difference is zero and increases to the sides of the measurement area to about ± 2.5 mm.

For the crossed light sheets setup the required coherence length is even smaller. Figure 2.18 shows a schematic of such a setup. The path length difference for the points in the xy -plane is zero for any point within this plane, as the two light sheet optics are symmetrically located above and below this plane. To form the measurement volume the light sheets need to have a certain thickness h . The variation of *OPD* across the height h of the measurement volume along the x -axis is shown in Fig. 2.19 again for a measurement area located at $L = 2$ m away from the light sheet optics and for a light sheet thickness of $h = 10$ mm. *OPD* is constant along lines that fan out away from the light sheet sources. *OPD* is zero along $z = 0$ and increases resp. decreases across the height to a maximum value of ± 25 μm . The variation of *OPD* across a plane located at $z = 0.5$ mm, the upper edge of the measurement volume, is shown in Fig. 2.20. The *OPD* is constant along circles with a center located at $x = y = 0$ and it decreases with increasing distance away from the light sheet optics from 25 μm down to 16 μm .

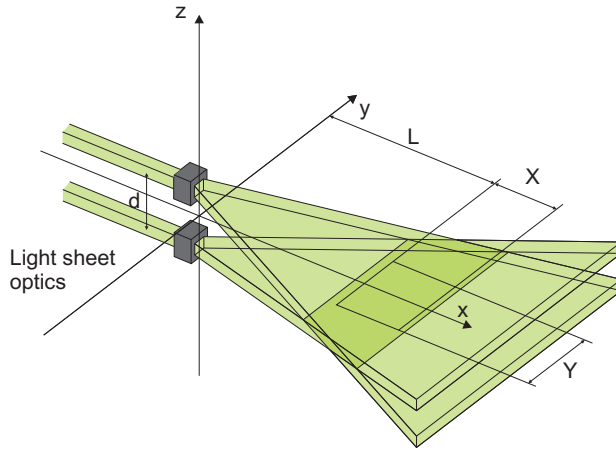


Figure 2.18: Crossed light sheets setup.

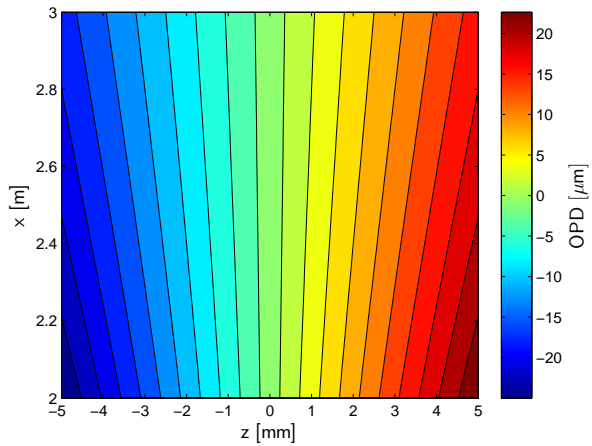


Figure 2.19: OPD in the xz -plane of the crossed light sheets configuration.

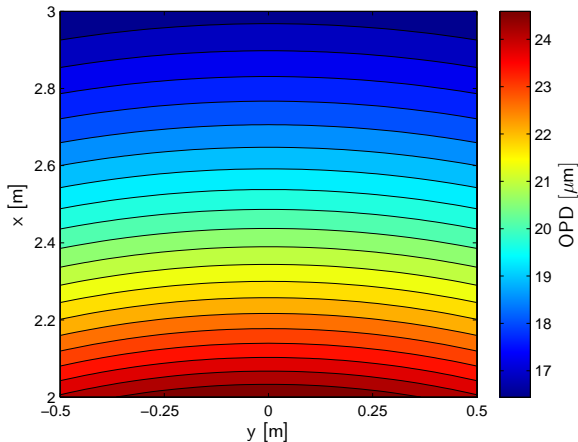


Figure 2.20: *OPD* in the xy -plane of the crossed light sheets configuration at the upper edge of the light sheet.

2.2.5 Light Sources

The light sources that can be used for HDGV and ILDV have to meet three requirements:

- The coherence length l_c needs to be sufficiently long.
- It should be possible to generate a light sheet from the emitted light, without losing too much of the power of the light source.
- The light source needs to offer high optical output power.

For LDV lasers are typically used as light source. They are also the best suited light source for HDGV and ILDV, as they also provide the ability to form light sheets and offer high optical output power. Depending on the type of laser the available coherence lengths extend over several orders of magnitudes. Diode lasers have coherence lengths of typically around $50\ \mu\text{m}$, while single-mode fiber lasers can achieve coherence lengths exceeding $100\ \text{km}$. Also the available laser power ranges from some mW to several kW.

The laser power needed for a planar measurement, using a camera offering 1 Mfps, can easily be on the order of 100 W as the experiments in Chap. 3 will show. The required coherence length greatly differs between HDGV,

co-planar ILDV and crossed light sheet ILDV, as shown in Sec. 2.2.4. For HDGV l_c needs to be on the order of cm to m depending on the size of the illuminated plane. For co-planar ILDV l_c needs to be around 1 mm and for crossed light sheet ILDV around 10 μm . High power lasers with a sufficient coherence length for HDGV are usually very expensive. Affordable lasers with an output power in the range of 100 W usually offer only coherence lengths of about 100 μm . They are therefore only suitable for crossed light sheet ILDV.

The recent development of high power LEDs offers an interesting and especially cheaper alternative to lasers. With a coherence length of about 10 μm they can be used for crossed light sheet ILDV. When used in pulsed mode, they already offer up to 60 W and generating reasonably thin light sheets is possible as well (Willert et al., 2010). As they are very cheap, a higher output power can easily be achieved by using several LEDs in parallel. Additionally the rather low coherence length l_c also helps to create the probe volume, even if the light sheets are not perfectly collimated: Only the particles in the area where $OPD < l_c$ will generate a Doppler signal. Particles outside this area will only generate an unmodulated signal which will appear as an offset to the Doppler signal.

2.3 Signal Detection

For the planar extension, it is not only necessary to generate the planar measurement geometry. Also an imaging detection system that is capable of detecting the signal is needed. Since a signal frequency has to be determined, it is required to record a time-series of several images. Using a very small crossing angle of 0.3° in ILDV, the resulting sensitivity is still about 10 kHz/(m/s). Thus for a velocity measurement range of 10 m/s a camera with a frame rate of at least 200'000 frames per second (fps) is needed. Recent developments have made several high speed cameras commercially available with frame rates of up to 1 million frames per second (Mfps). Depending on the operating principle, even frame rates of up to 100 Mfps are possible. A short overview on the different high speed camera technologies and the currently available cameras will therefore be given in the next section.

Another approach for the detection of the modulated signals is the use of so-called “smart pixel” detector arrays (SPDA). These detector arrays offer at the pixel level not only the ability to detect light, but also some basic pre-processing of the signal. Several different SPDAs exist, but their pixel level pre-processing is usually very problem specific. Two of them offer a pre-processing that can be used to detect the Doppler signal: Recent advances in parallel Optical Coherence Tomography have led to the devel-

opment of the pOCTii detector by [Beer et al. \(2005\)](#). This SPDA offers a resolution of 144×90 pixels and performs a dual phase lock-in detection on each pixel with a maximum demodulation frequency of 250 kHz. As this sensor has been used for some measurements presented in [Chap. 3](#), its working principle is presented in detail in [Sec. 2.3.2](#). Another SPDA that could be used is the dynamic vision sensor (DVS) developed by [Lichtsteiner et al. \(2007\)](#). The working principle of this sensor completely differs from a conventional camera as it does not record individual frames but only responds to changes in intensity on each pixel. A brief overview of the functionality of this sensor and its potential for a planar Doppler measurement is given in [Sec. 2.3.2](#) as well.

For HDGV the sensitivity of the system is much higher, as shown in [Sec. 2.2.1](#). Therefore even faster cameras are needed for the same velocity range. Additionally the signal has, due to the offset of the reference beam, a very low visibility, therefore requiring a very high dynamic range. This high dynamic range can hardly be achieved using high speed cameras, thus those signals can only be detected using SPDAs.

2.3.1 High Speed Camera

Based on their working principle, high speed cameras (HSC) are very simple devices. Once the camera is triggered, it just acquires a time series of N_f images which are stored in the camera. This set of images is then transferred to the computer where it can be analyzed. The main limiting factor in any high speed camera system is the speed of the readout of the data from the sensor and its transfer into the memory of the camera. Therefore there is typically a trade off between frame rate, resolution and the number of images acquired. For optimizing this trade off three different camera concepts exist.

Conventional High Speed Cameras

The most common HSC type works as any normal camera. There is one single detector array which is exposed to the light. To achieve the high frame rates there are just many more output tabs on the sensor, compared to a normal camera. The high frame rate is therefore achieved with a massive parallel readout of the sensor and the number of images that can be acquired is only limited by the memory inside the camera. Those cameras are typically designed to record at medium frame rates of around 5000 Hz at video resolutions of 1280×720 pixels to 1920×1080 pixels. Higher frame rates of up to 1.4 Mfps can be achieved with those cameras by reducing the resolution. At such high frame rates the image acquired is usually

Table 2.1: Performance examples of the Photron FASTCAM SA5 and the Vision Research Phantom v711.

| FASTCAM SA5 | Phantom v711 |
|--------------------------------|--------------------------------|
| 1024 × 1000 pixels at 7500 fps | 1280 × 800 pixels at 7530 fps |
| 128 × 128 pixels at 262500 fps | 128 × 128 pixels at 215600 fps |
| 64 × 16 pixels at 1000000 fps | 128 × 8 pixels at 1400000 fps |

only a narrow stripe of around 128×8 pixels. Such a narrow stripe can hardly be regarded as an image anymore. But at intermediate resolutions of, say, 128×128 pixels frame rates of 200 kfps are already available. Two typical representatives of this camera type are the Photron FASTCAM SA5 and the Vision Research Phantom v711. Their specifications are listed in Tab. 2.1.

The development of those cameras has seen a massive improvement in both frame rate and resolution over the last years. Cameras with reasonable resolutions of 128×128 pixels at 1 Mfps can therefore be expected to be readily available in the near future.

Framing Cameras

In contrast to the conventional “single chip” HSCs framing cameras use the opposite approach: To achieve the high frame rate, they use several sensors, which are consecutively exposed to the incoming light. As a separate sensor is used for each image the frame rate of those cameras is only limited by the technique used to direct the light to each sensor. This can be done using a rotating mirror as e.g. in the Bandaris 128 (Chin et al., 2003). Alternatively beam splitters can be used to direct the light to the individual sensors as for example in the Imacon 468 system (DRS Technologies, Tring, UK). Similar cameras are also produced by Specialized Imaging and PCO. This concept needs additional image intensifiers as shutters to control the exposure of each sensor. The number of images that can be acquired is therefore limited by the number of sensors inside the camera. The main advantage of those systems is the frame rate that can be achieved. With the Bandaris 128 a frame rate of 25 Mfps with 128 consecutive images at a resolution of 500×292 pixels has been achieved. With the Imacon 468 system even higher frame rates of 200 Mfps with a resolution of 576×385 pixels can be achieved, but only 8 consecutive images are recorded. The drawbacks of those cameras are their price and size, as they basically consist of many individual cameras. Additionally for the Doppler measurement it is important that all the image sensors are very well aligned to each other,

such that the corresponding pixels in each sensor record the same signal. While this can easily be achieved for 8 individual sensors, it seems rather questionable to achieve this with a camera consisting of 128 sensors.

In-situ Storage Image Sensor

Another different technique to achieve a high frame rate is used in the In-situ Storage Image Sensor Version 2 (ISIS-V2) developed by [Etoh et al. \(2003\)](#). This CCD sensor allows to record 103 consecutive images at 1 Mfps with 260×312 pixels. To every pixel in the ISIS-V2, 103 memory elements are attached on the image sensor itself. During the image acquisition the integrated image signals are stored in those so-called in-situ storage elements without being read out from the sensor. The frame rate of this sensor is therefore only limited by the time it takes to shift the data into the in-situ storage. One of the main drawbacks of the ISIS-V2 is the low fill factor of only 13% as the in-situ storage requires a lot of space. This low fill factor results into a very low sensitivity of the sensor. The ISIS-V2 is used in the Shimadzu HPV-1 and the Photron FASTCAM IS-1M.

The further development of this sensor has led to the ISIS-V16 ([Etoh et al., 2011](#)). A back side illuminated CCD is employed capable of recording 117 consecutive images at 16 Mfps with 362×456 pixels. With the back side illumination the fill factor has been increased to 100%. Additionally charge carrier multipliers (CCM) are installed in the readout section of the sensor. The CCM and the back side illumination structure allow for a very high sensitivity of less than ten photons.

A similar camera system has also been developed by Princeton Scientific Instruments but with a much lower resolution of 64×64 pixels. Also some custom camera manufacturers such as XCam and Theta System offer systems that employ the same storage principle on modified standard CCDs.

2.3.2 Smart Pixel Detector Array

Parallel Optical Coherence Tomography Imager - pOCTii

The working principle of the pOCTii sensor presented in this section has been previously published in *Experiments in Fluids* in 2012 ([Meier et al., 2012](#)).

The pOCTii sensor is a SPDA which has been developed for parallel optical coherence tomography ([Beer et al., 2005](#)). The advantage of this detector array is that it not only detects the light as does a conventional integrating camera, but it performs a dual phase lock-in detection on each pixel with a maximum demodulation frequency f_D of 250 kHz at a resolu-

tion of 144×90 pixels. Using the signal processing described in Sec. 2.4.2, this compares to a frame rate of 1 Mfps for a conventional high-speed camera. As it is developed to detect signals with a low modulation depth it additionally offers an offset compensation which increases the sensitivity to 86 dB. This is helpful if many particles are imaged onto the same pixel and thus the visibility of the signal is low.

Dual phase lock-in amplifiers are normally used to extract the amplitude A and the phase ϕ of weak periodic signals of known frequency f from a noisy background. The functional principle of a dual phase lock-in amplifier relies on the orthogonality of sinusoidal functions as described in Eqs. 2.38 and 2.39:

$$I = \langle A \cos(2\pi ft + \phi) \cos(2\pi f_D t) \rangle$$

$$= \begin{cases} \frac{A}{2} \cos(\phi) & \text{if } f_D = f \\ 0 & \text{otherwise} \end{cases} \quad (2.38)$$

$$Q = \langle A \cos(2\pi ft + \phi) \sin(2\pi f_D t) \rangle$$

$$= \begin{cases} \frac{A}{2} \sin(\phi) & \text{if } f_D = f \\ 0 & \text{otherwise} \end{cases} \quad (2.39)$$

The periodic input signal with the frequency f , phase ϕ and amplitude A is multiplied with a periodic reference signal at the demodulation frequency f_D and averaged over a sufficiently long time. The ideal output of the lock-in amplifier is only non-zero if the signal frequency f and the demodulation frequency f_D are the same. The resulting in-phase (I) and quadrature (Q) components can be used to calculate the amplitude A and the phase ϕ of the signal:

$$A = \sqrt{I^2 + Q^2} \quad (2.40)$$

$$\phi = \arctan\left(\frac{Q}{I}\right) \quad (2.41)$$

This lock-in detection is implemented on each pixel in the pOCTii as follows: The incoming light is first integrated on the photosensitive area of the pixel and sampled at the sampling frequency f_s which corresponds to four times the demodulation frequency f_D . These samples are then multiplied by a discrete periodic signal with frequency f_D and the discrete values $[1, 0, -1, 0]$ for the I component and for the Q component with the values $[0, 1, 0, -1]$. These discrete values replace the sine and the cosine of the

lock-in detection algorithm. The signals are then accumulated over several periods and read out. Eqs. 2.42 and 2.43 describe this process:

$$I(t_i) = \sum_{k=0}^{N-1} \left(\int_{4kT_{qp}}^{(4k+1)T_{qp}} S(t) dx - \int_{(4k+2)T_{qp}}^{(4k+3)T_{qp}} S(t) dx \right) \quad (2.42)$$

$$Q(t_i) = \sum_{k=0}^{N-1} \left(\int_{(4k+1)T_{qp}}^{(4k+2)T_{qp}} S(t) dx - \int_{(4k+3)T_{qp}}^{(4k+4)T_{qp}} S(t) dx \right) \quad (2.43)$$

$S(t)$ is the signal to be detected, T_{qp} denotes the integration time ($T_{qp} = 1/f_s$) and N is the number of periods to be averaged, as the averaging process cannot be performed over infinitely long times. The effect of the finite averaging for three different averaging lengths N on the calculated amplitude for an input signal S described by Eq. 2.12 with $A_1 = A_2 = 1$ and frequency $f = \nu_1 - \nu_2$ is shown in Fig. 2.21. The ideal sharp discrimination described in Eqs. 2.38 and 2.39 between signals that are modulated with f_D and signals that are modulated with a different frequency is relaxed: Signals with frequencies different from the demodulation frequency f_D also generate a non-zero output signal. To achieve a peak-width narrower than 1% the averaging has to be performed over more than $N = 40$ periods.

The pOCTii could therefore be used to detect the Doppler frequency by sweeping f_D over the range of expected frequencies. But using the detector as a lock-in amplifier for a flow measurement does not offer a practical performance: For a measurement resolution of 1% of the measured frequency range a sweep of the detector is needed with 100 different lock-in frequencies and an averaging over 40 periods for each frequency. This leads to long acquisition times to obtain a reasonably accurate result.

Another more promising use of the demodulation principle that does not require a time consuming frequency sweep, is based on autocorrelations and is presented in Sec. 2.4.2.

Dynamic Vision Sensor - DVS

The motivation for the development of the Dynamic Vision Sensor (DVS) is that a normal scene usually consists of a lot of static information and only few features change in time. In a high speed camera the data rate of the readout of the data from the sensor limits the frame rate of the camera. If in the recorded scene only few features change between the frames it is basically this static redundant information that limits the frame rate. The DVS is designed to discard this static information and only generate an output for changes in intensity in the scene (Lichtsteiner et al., 2007).

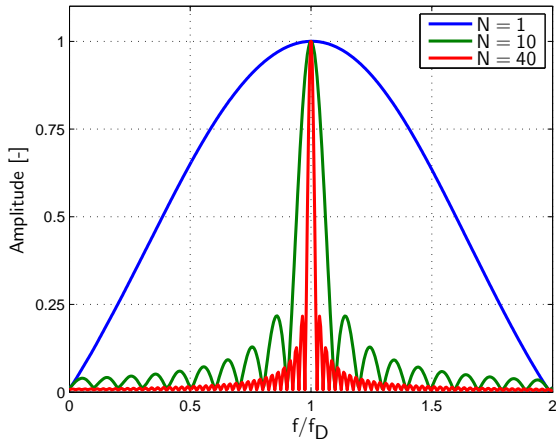


Figure 2.21: Output amplitude of the lock-in detection as a function of the signal frequency for different averaging lengths.

Thus the working principle of the DVS differs significantly from normal cameras. Instead of recording a stream of data for each pixel, the image sensor reacts to changes in intensity on each pixel. If the change of intensity which a pixel detects exceeds a predefined threshold, the pixel generates an event and the sensor generates a data stream consisting of the time of such an event and its location on the sensor. The Doppler frequency could then be analyzed by the time between the events like in early LDV where zero-crossings of the Doppler signal were analyzed (Adrian, 1972).

As with the conventional HSCs the limiting factor is also for this sensor the data transfer from the sensor into the memory. For the DVS this limit is expressed by the number of events that can be detected per second (events/s). The current DVS allows to detect 1 Mevents/s on 128×128 pixels. While this resolution is already sufficient, the number of events/s is not high enough for an instantaneous ILDV measurement: In an ILDV measurement system, where many particles are within the illuminated plane, there is no static information present. Therefore the measurable Doppler frequency will become very low using the DVS. But in a system where only a low seeding density can be used, the sensor offers an advantage to normal cameras: With a low seeding density the camera needs to acquire a signal until each pixel has recorded the Doppler signal of at least one particle. A normal camera therefore needs to record the signal of each pixel for the

whole time, generating a large amount of data. In contrast the DVS sensor only generates data when a particle is present in the probe volume and therefore massively reduces the requirement on the data storage.

2.4 Data Analysis

As described in Sec. 2.2 the individual pixels of the camera used to detect the scattered light can be seen as individual single point LDVs. Therefore many of the data analysis techniques that are used in LDV are also applicable to the signals acquired using HDGV and ILDV. A broad overview of those techniques can be found in “Laser Doppler and Phase Doppler Measurement Techniques” (Albrecht et al., 2003). Nevertheless the cameras used to acquire the signal impose some restrictions on the possible data analysis techniques. If a high speed camera is used, the number of acquired frames N_f depends on the type of camera as shown in Sec. 2.3.1. It starts at $N_f = 4$ and can easily reach $N_f > 10000$. In the case where $N_f > 100$ frames, the spectral analysis can be done using discrete Fourier transforms (DFT) on the time series recorded by each pixel. Since it is a well known technique, it will be presented only briefly, discussing the main properties and the necessary steps for the data analysis. For very low numbers of N_f and also for the signal processing of the data from the pOCTii a data analysis technique is needed that does not require many successive frames, but is rather based on averaging over independent measurements of the Doppler signal. For this purpose a data analysis technique based on autocorrelations is presented.

2.4.1 Fourier Analysis

The Fourier analysis of discrete signals is usually performed using Discrete Fourier Transforms (DFT). The DFT of a finite series of an uniformly sampled signal S_i , sampled at the sampling frequency f_s is defined as

$$\hat{S}_k = \hat{S}(f_k = k\Delta f) = \mathcal{F}(S_i) = \sum_{i=0}^{N_f-1} S_i e^{-j2\pi \frac{ik}{N_f}}, \quad k = 0, 1, \dots, (N_f - 1) \quad (2.44)$$

The spectral components \hat{S}_k are computed for the equally spaced frequencies f_k given by

$$f_k = \frac{k f_s}{N_f}, \quad (2.45)$$

where N_f is the number of samples used for the DFT. The frequency spacing Δf between the Fourier coefficients is

$$\Delta f = \frac{f_s}{N_f}. \quad (2.46)$$

Δf is therefore both the lowest frequency that can be resolved and also the frequency resolution of the spectral components.

The power spectral density (PSD) $W(f_k)$ of the signal S_i is given by the squared magnitude of the spectral components:

$$W(f_k) = W_k = \frac{1}{N_f f_s} \hat{S}_k \hat{S}_k^*. \quad (2.47)$$

The PSD describes the signal power of the different frequencies which are present in the signal S between the frequencies 0 and f_s . A more convenient representation is the use of positive and negative frequencies where all values of $k \geq N/2$ are interpreted as negative frequencies

The frequency f_{peak} of the peak in the PSD therefore describes the dominant frequency of the signal. Due to the frequency spacing Δf , the resolution of the PSD is also limited to Δf . With a Gaussian interpolation using three points around the peak position k the resolution can be typically increased by a factor of 10:

$$\delta = \frac{\ln(W_{k-1}) - \ln(W_{k+1})}{2[\ln(W_{k+1}) - 2\ln(W_k + \ln(W_{k-1}))]} \quad (2.48)$$

And the frequency of the interpolated peak is:

$$f = \Delta f(k + \delta) \quad (2.49)$$

To achieve a resolution of $<1\%$ in the determination of the signal frequency it is therefore necessary that $N_f \geq 32$. With $N_f = 32$ the frequency spacing is $f_s/32$ resulting in 16 different frequencies between 0 and $f_s/2$. Using the peak interpolation this resolution can be increased by a factor of 10 such that a resolution of $1/160 = 0.625\%$ results.

2.4.2 Autocorrelation Based Analysis

The autocorrelation $R(\tau)$ of a complex continuous signal $S(t)$ is defined as:

$$R(\tau) = \int_{-\infty}^{\infty} S(t)S(t + \tau)^* dt. \quad (2.50)$$

where $S(t)^*$ is the complex conjugate of the signal $S(t)$. As $S(t)$ is complex, $R(\tau)$ is complex as well and a Hermitian function, i.e. $R(-\tau) = R^*(\tau)$. $R(\tau)$ can therefore be written as

$$R(\tau) = A(\tau)e^{j\phi(\tau)}, \quad (2.51)$$

where $A(\tau)$ is an even function and $\phi(\tau)$ is an odd function.

The analysis using autocorrelations to estimate a signal frequency is based on the pulse pair statistics method described by [Miller et al. \(1972\)](#): The Wiener–Khinchin theorem states that the power spectral density $W(f)$ and the corresponding autocorrelation $R(\tau)$ of a signal $S(t)$ are Fourier transform pairs. Using this theorem one can show that the mean μ of $W(f)$ corresponds to the derivative of $R(\tau)$ evaluated at $\tau = 0$:

$$\mu(W(f)) = \frac{\int_{-\infty}^{\infty} fW(f)df}{\int_{-\infty}^{\infty} W(f)df} = \frac{1}{i2\pi R(0)} \left. \frac{dR(\tau)}{d\tau} \right|_{\tau=0} \quad (2.52)$$

As the autocorrelation is a Hermitian function, this can be reduced to

$$\mu(W(f)) = \dot{\phi}(0). \quad (2.53)$$

$\mu(W(f))$ can thus be estimated for small $\tau \neq 0$ by

$$\mu(W(f)) = \dot{\phi}(0) \approx \frac{\phi(\tau)}{\tau} = -\frac{1}{2\pi\tau} \arctan\left(\frac{\Im\{R(\tau)\}}{\Re\{R(\tau)\}}\right) = \hat{\nu}. \quad (2.54)$$

Here, $\hat{\nu}$ is the estimate of $\mu(W(f))$. To achieve a minimum variance in $\hat{\nu}$, τ needs to be in the range of

$$\frac{0.5}{2\pi f_B} \leq \tau \leq \frac{5}{2\pi f_B}, \quad (2.55)$$

where f_B is the frequency broadening described in [Sec. 2.1.4](#).

This estimate of the mean frequency $\hat{\nu}$ is only useful for zero mean analytic signals, as they have a PSD which is zero for $f < 0$ and therefore $\mu(W(f)) \neq 0$. Signals, like the data acquired using a camera, differ in several points from the required zero mean analytic signals: The signal $S(t)$ is not continuous, it is sampled at the sampling frequency f_s . Thus $S(t) = S(t_i) = S_i$ with $t_i = i/f_s$. The signal is also not infinitely long, as only a finite number of images N_f can be acquired. Furthermore S_i is not complex and always positive. Its PSD is therefore symmetric with respect to f and S_i is not zero mean. The above derivation to estimate the mean frequency of a signal is valid as well for discrete signals. But in order to use this approach for the signal acquired with a camera, the signal has to be pre-processed to obtain a zero mean analytic signal: First S_i has to be

made mean-free by using a high pass filter F_{HP} . As N_f is usually small (<32) only a simple high pass filter can be used, e.g.:

$$S_i^{AC} = S_{i+1} - S_i, \quad i = 0, 1, \dots, N_f - 1 \quad (2.56)$$

or described as a convolution with the filter F_{HP} :

$$S_i^{AC} = S * F_{HP}[i] \quad (2.57)$$

$$F_{HP} = [-1, 1] \quad (2.58)$$

The zero mean signal S_i^{AC} can then be converted into an analytic signal S_i^a using the Hilbert transform \mathcal{H} :

$$S_i^a = S_i^{AC} + j\mathcal{H}(S_i^{AC}), \quad i = 0, 1, \dots, N_f - 1 \quad (2.59)$$

with

$$\mathcal{H}(S_i^{AC}) = \sum_{k=0}^{N_f-1} S_i^{AC} \frac{1 - \cos(\pi(i-k))}{\pi(i-k)} \quad (2.60)$$

$$= S^{AC} * \frac{1 - \cos(\pi(i-k))}{\pi(i-k)} = S^{AC} * F_{Hilbert}[i]. \quad (2.61)$$

S_i^a is then used to calculate the discrete autocorrelation $r(k)$

$$r(k) = \sum_{i=0}^{N_f-1} S_i^a S_{i-k}^{a*}, \quad (2.62)$$

and $r(k)$ can be used to calculate the estimate $\hat{\nu}$ of the mean frequency of the signal:

$$\mu(W^a(f)) = -\frac{1}{2\pi k \Delta t} \arctan \left(\frac{\Im\{r(k)\}}{\Re\{r(k)\}} \right) = \hat{\nu}. \quad (2.63)$$

The time delay τ from Eq. 2.54 is now a multiple of the sampling interval $\Delta t = 1/f_s$.

Obviously the number of consecutive acquired images N_f influences the estimated frequency $\hat{\nu}$. Using the Hilbert transform an analytic signal is only obtained for $N_f \rightarrow \infty$. As this data analysis is intended for cases where $N_f < 32$, the influence of the truncated Hilbert transform on $\hat{\nu}$ has to be analyzed. For such small N_f the autocorrelation $r(k)$ has to be calculated using M independent realizations of S . The M independent measurements can be consecutive measurements, but also neighboring pixels from the camera, if the resolution is good enough to allow for some spatial averaging. In fact $\hat{\nu}$ can be estimated using only 3 consecutive images and averaging

over many independent realizations as $r(k)$ only has to be evaluated at one point k to calculate $\hat{\nu}$. Therefore only S_i^a and S_{i-k}^a are needed. To calculate S_i^a and S_{i-k}^a for $k = 1$ only three data points in S_i are needed: The Hilbert transform needs at least two data points and one additional data point is needed for the high pass filter.

But for a finite and low number of N_f Eq. 2.63 is only valid in the limit of $\tau \rightarrow 0$. Due to the sampling, the lower limit for τ is $\tau = \Delta t$. To still use this approach to measure $\mu(W(f))$, the influence of the finite number of N_f and τ on $\hat{\nu}$ have to be analyzed. The points that have to be considered are:

- Does still a unique relationship between $\hat{\nu}$ and $\mu(W(f))$ exist, such that $\hat{\nu}$ can be used to calculate $\mu(W(f))$, although Eq. 2.63 is not valid anymore.
- How many independent realizations M are needed.
- How many signal periods N_p^{min} are necessary for a reliable frequency estimation.
- How does a signal with a finite frequency bandwidth f_B , e.g. from a turbulent flow, influence $\hat{\nu}$.

Although $\hat{\nu} \neq \mu(W^a(f))$ it is still related to it. Analyzing the influence of the two filters F_{HP} and $F_{Hilbert}$ on $W^a(f)$ is therefore useful to assess the dependence of $\hat{\nu}$ on N_f and τ : The PSD of the initial signal S_i and the derived analytic signal S_i^a are:

$$W(f) = \mathcal{F}\{S\}\mathcal{F}\{S\}^* \quad (2.64)$$

$$W^a(f) = \mathcal{F}\{S^a\}\mathcal{F}\{S^a\}^* \quad (2.65)$$

The derived analytic signal S_i^a is calculated from S_i as described above:

$$S_i^a = S_i * F_{HP} + j[S_i * F_{HP}] * F_{Hilbert} \quad (2.66)$$

Using the convolution theorem $\mathcal{F}\{S^a\}$ can be calculated as

$$\mathcal{F}\{S^a\} = \mathcal{F}\{S_i^a\}\mathcal{F}\{F_{HP}\} [1 + j\mathcal{F}\{F_H\}] \quad (2.67)$$

and therefore

$$W^a(f) = W(f)W_{HP}(f)W_H(f) \quad (2.68)$$

with

$$W_{HP}(f) = \mathcal{F}\{F_{HP}\}\mathcal{F}\{F_{HP}\}^* \quad (2.69)$$

$$W_H(f) = (1 + j\mathcal{F}\{F_H\})(1 + j\mathcal{F}\{F_H\})^* \quad (2.70)$$

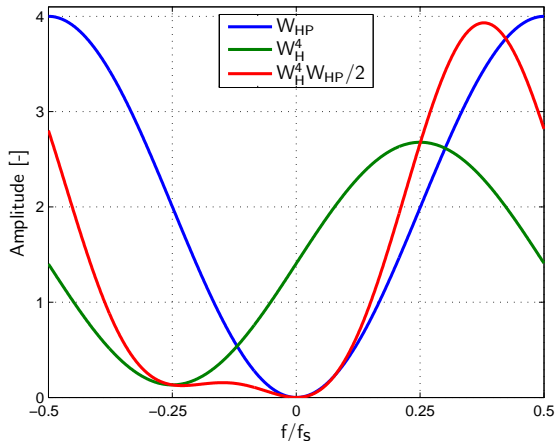


Figure 2.22: PSD of W_{HP} , W_H^4 and $W_H^4 W_{HP}/2$ for $N_f = 4$.

$W^a(f)$ is simply obtained by multiplying the PSD of the initial signal S_i with the PSDs of the two filters W_{HP} and W_H . Figure 2.22 shows W_{HP} and W_H^4 and $W_H^4 W_{HP}/2$ for $N_f = 4$, and Fig. 2.23 shows W_{HP} and W_H^{16} and $W_H^{16} W_{HP}/4$ for $N_f = 16$. The factors 2 and 4 have only been used for scaling as the absolute amplitudes are not relevant. W_{HP} is, as required, zero at $f = 0$. It therefore eliminates the mean of the signal. The filters resulting from the Hilbert transform W_H^4 and W_H^{16} damp the amplitudes of the negative frequencies and therefore generate an asymmetric power spectrum. W_H^{16} obviously filters S_i such that it becomes a better approximation of an analytic signal, as more points for the Hilbert transform are used. The product $W_H W_{HP} = W_F$, which acts on S is therefore asymmetric and 0 at $f = 0$ as well. But W_F is also a function of f for both N_f and therefore induces a frequency dependent weighting in $W^a(f)$. While this is not a problem for signals with very small bandwidths f_B , the estimated frequency $\hat{\nu}$ of signals with a finite bandwidth f_B will be biased. The influence of the filtering on a signal with a center frequency of $f = 0.215 f_s$ and a finite bandwidth of $f_B/f_s = 7.5\%$ is shown in Fig. 2.24. The blue curve shows a close up on the original PSD, the green line the filtered PSD and the red line the filter $W_F = W_H^4 W_{HP}$. Due to the slope of the filter, the peak of $W^a(f)$ is slightly shifted to a higher frequency and the whole spectrum is deformed. Therefore also $\mu(W^a(f))$ is shifted to a higher frequency and as $\hat{\nu}$ estimates $\mu(W^a(f))$, $\hat{\nu}$ will be biased with respect to $\mu(W(f))$. The

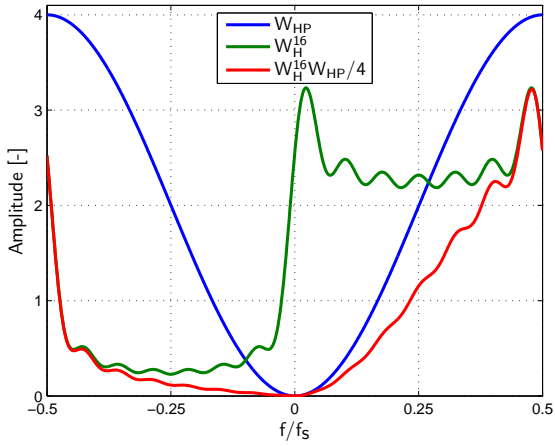


Figure 2.23: PSD of W_{HP} , W_H^{16} and $W_H^{16}W_{HP}/4$ for $N_f = 16$.

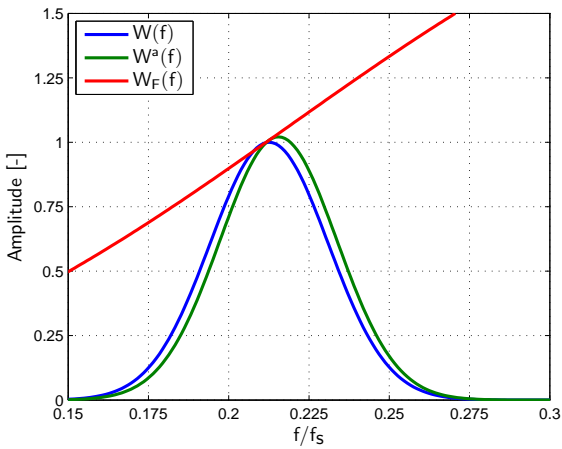


Figure 2.24: Peak shift of the PSD $W(f)$ of a signal due to the filter applied on it.

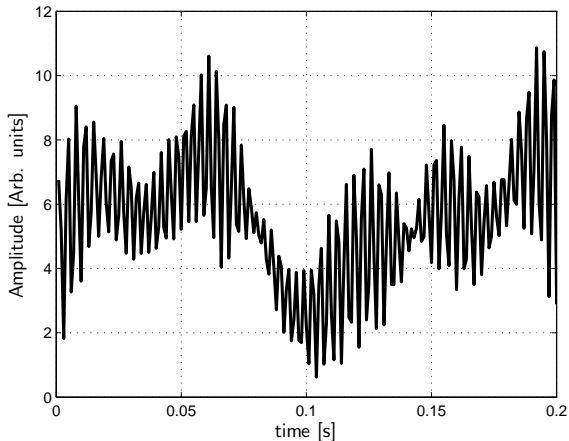


Figure 2.25: Typical signal used for the calculation of $\hat{\nu}$.

magnitude of this shift depends on f_B : The larger f_B the larger the shift will be. This shift will therefore generate a bias in the estimated frequency $\hat{\nu}$ which cannot be corrected since f_B is usually unknown.

This qualitative analysis already gives some insight in the properties of the algorithm, which have to be further analyzed. The influences of τ , N_f and f_B have to be analyzed numerically as $\hat{\nu} \neq \mu(W^a(f))$ for $\tau = k\Delta t$. For the simulation a signal S_i is generated as a superposition of N_{part} independent signals described by Eq. 2.20. The number of particles N_{part} , i.e. the number of superimposed signals, is chosen such that in average always two particles are present at the same time. The arrival time t_m and the phase ϕ of each particle is random and white noise with an amplitude of 10% of the peak amplitude of the signal is added. A typical signal S is shown in Fig. 2.25. For each data point 81920 independent signals S were calculated to eliminate the influence of the random arrival times and phases.

The dependence of $\hat{\nu}$ on N_f for $f_B = 0$ and $\tau = 1/f_s$ is shown in Fig. 2.26 for different N_f . For a large number of successive images N_f , $\hat{\nu}(f)$ becomes almost a straight line. This could be expected since for such a large number the Hilbert transform generates an almost pure analytic signal. For smaller N_f $\hat{\nu}(f)$ deviates, but it remains a strictly increasing function. Therefore numerical inversion of $\hat{\nu}(f)$ is possible and can be used as a calibration function for $\hat{\nu}$ to calculate f .

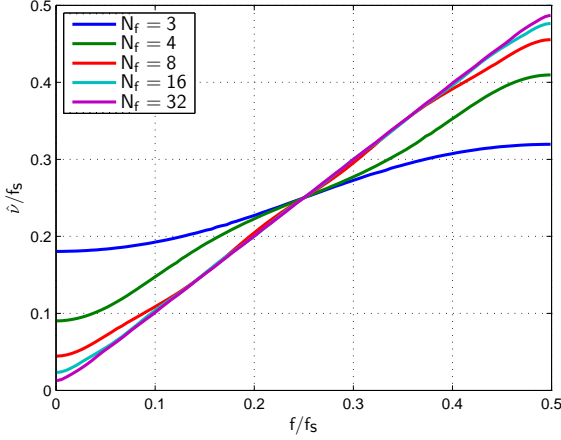


Figure 2.26: Dependence of \hat{v} on N_f for $f_B = 0$ and $\tau = 1/f_s$.

The influence of τ is shown in Fig. 2.27 again for $N_f = 8, 16, 32$ and for $\tau = 4/f_s$. A lower number of N_f is not possible due to τ . $\hat{v}(f)$ shows an additional wrapping at $f/f_s = 0.125$ and $f/f_s = 0.375$. For a distributed measurement this wrapping is less restrictive than it seems: a flow field usually does not show such strong discontinuities and therefore the flow field can be reconstructed. The phase unwrapping problem can be solved in a least-squares sense, using for example the fast cosine transform as suggested by Ghiglia et al. (1994).

The influence of the number of signal periods N_p generated by a single particle on \hat{v} is shown in Fig. 2.28 for $N_f = 4$. The bias error ϵ of \hat{v} is normalized by the measurement range. At $f < 1/8f_s$ there is a large bias error for all N_p . This bias stems from the noise in the signal, limiting the measurement range at the lower end. At the upper end of the measurement range the bias error strongly increases as N_p decreases. With $N_p > 5$ this error can be limited to less than 1% over the frequency range of $1/8f_s < f < 3/8f_s$.

The dependence of ϵ on N_f is shown in Fig. 2.29 for $N_p = 5$ and $\tau = 1/f_s$. For $N_f \geq 4$ the bias error is smaller than $\pm 0.75\%$ over the frequency range of $1/8f_s < f < 3/8f_s$. The bias error is also very similar for all $N_f \geq 4$, as it is mainly generated by the simple high pass filter.

The influence of τ on ϵ is shown in Fig. 2.30 for $N_f = 8$, $\tau = 4/f_s$ and different N_p . For $N_p < 5$ the error is again very large. This is because the

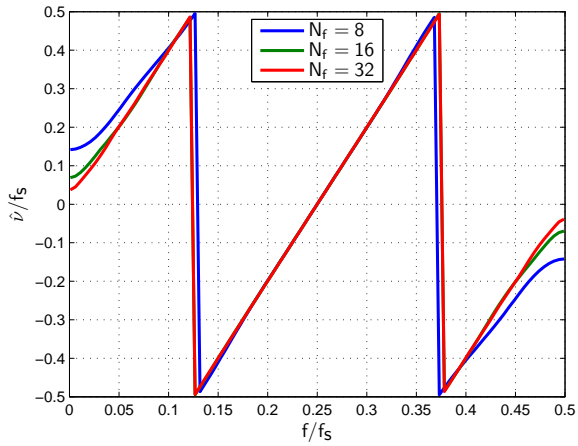


Figure 2.27: Dependence of \hat{v} on N_f for $f_B = 0$ and $\tau = 4/f_s$.

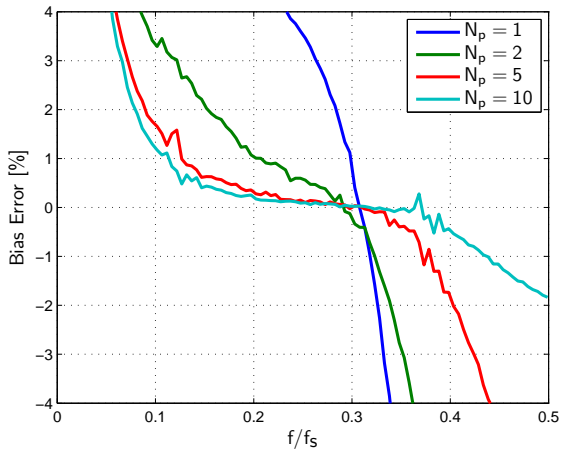


Figure 2.28: Bias error ϵ for different N_p for $N_f = 4$ and $\tau = 1/f_s$.

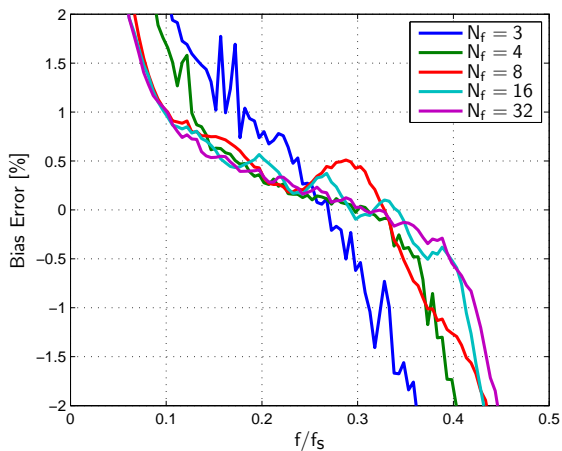


Figure 2.29: Bias error ϵ for different N_f for $N_p = 5$ and $\tau = 1/f_s$.

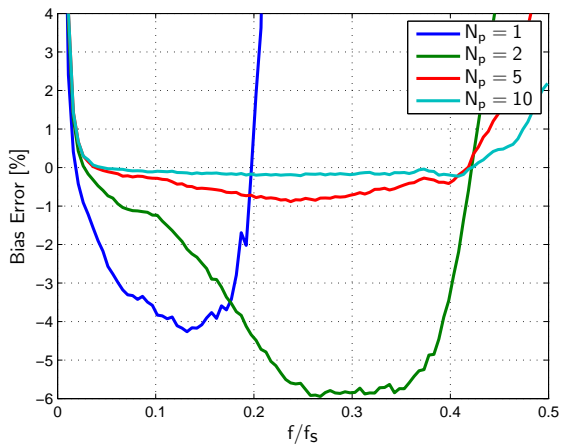


Figure 2.30: Bias error ϵ for different N_p for $N_f = 8$ and $\tau = 4/f_s$.

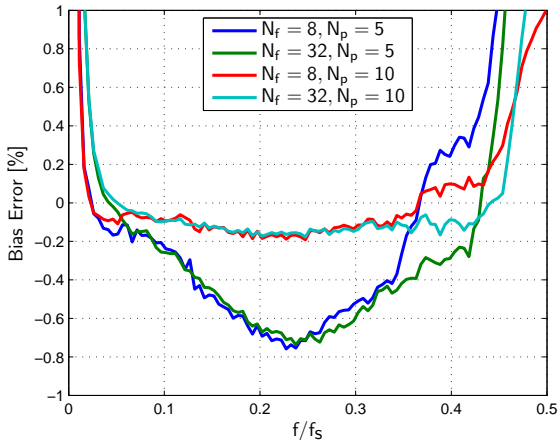


Figure 2.31: Bias error ϵ for different N_f for $N_p = 5, 10$ and $\tau = 4/f_s$.

chance that a particle which generates only 2 signal periods is present in all the frames used for the autocorrelation is very low. For $N_p \geq 5$ the error is smaller than 1% over almost the whole frequency range.

The dependence of ϵ on N_f for $\tau = 4/f_s$ is shown in Fig. 2.31 for $N_p = 5$ and 10. The influence of N_f is again very small and the error is lower than 0.8% over the whole measurement range for $N_p = 5$ and lower than 0.2% for $N_p = 10$.

The influence of N_p shows that in order to use this data analysis technique, the system should be set up such that $N_p \geq 5$, if possible even larger. At the same time the measurement range should be limited to $1/8f_s < f < 3/8f_s$ to minimize the errors generated by the setup. If 8 consecutive images can be recorded $\tau = 4/f_s$ should be used for the data analysis.

To be able to measure also turbulent flows, the data analysis technique should also avoid large bias errors for signals that have a finite frequency bandwidth f_B . The influence of f_B on \hat{v} is shown in Fig. 2.32 for $N_f = 4$ and $\tau = 1/f_s$ for five different f_B/f_s ranging from 0.5% to 12.5%. In the frequency range $1/8f_s < f < 3/8f_s$ the error is lower than 1% for $f_B/f_s \leq 5\%$. The bias error generated by a more optimal setup with $N_f = 8$ or $N_f = 32$ and $\tau = 4/f_s$ is shown in Fig. 2.33. Again there is only a minor improvement by increasing N_f beyond 8. However, a frequency bandwidth of 12.5% will still generate a bias larger than 2%.

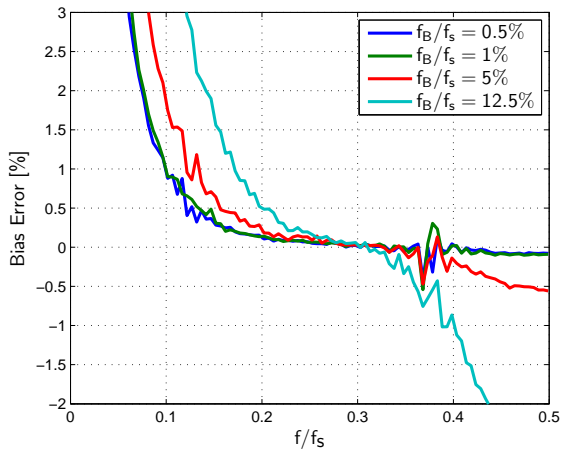


Figure 2.32: Bias error ϵ for different f_B for $N_f = 4$ and $\tau = 1/f_s$.

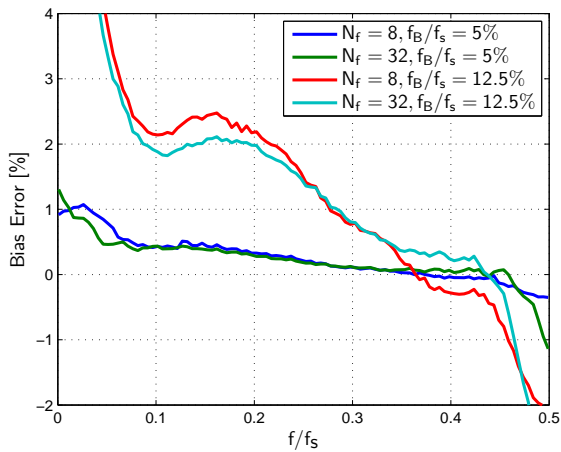


Figure 2.33: Bias error ϵ for different f_B for $N_f = 8, 32$ and $\tau = 4/f_s$.

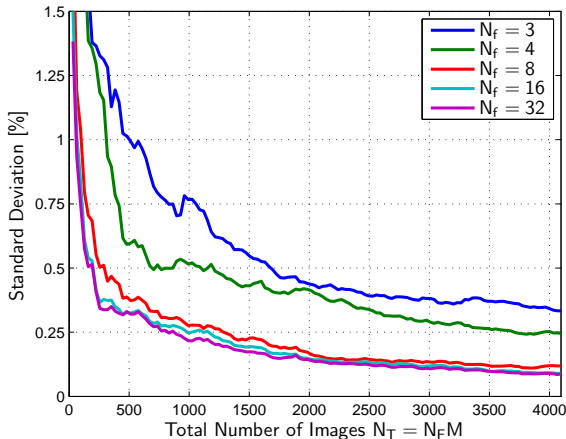


Figure 2.34: Convergence of $\hat{\nu}$ for different N_f at $f = 0.15f_s$, $f_B/f_s = 5\%$ and $\tau = 4/f_s$.

For a measurement in a highly turbulent flow, this means that the M independent realisations have to be recorded in a very short time. The velocity fluctuations have to remain smaller than 20% of the velocity range, that is measured, to not exceed a bias error of 1%.

The last point to be considered for this data analysis technique is the total number of images $N_T = N_f \times M$ needed for a converged autocorrelation. To compare the influence of N_f on the convergence, Fig. 2.34 shows the standard deviation over 50 independent calculations of $\hat{\nu}$ normalized by the measurement range as a function of N_T for a signal with $f = 0.15f_s$, $f_B/f_s = 5\%$, $\tau = 4/f_s$ and different N_f . The standard deviation drops very quickly below 1% for all N_f and the decay is increased by increasing N_f . For $N_f \geq 8$ less than 128 frames are needed. This corresponds to the same number of images needed for a Fourier analysis to achieve the same standard deviation. For $N_f = 3$ and 4 the decay is very slow and also for $N_T = 4096$ larger than 0.25%. This also explains why the presented error plots for $N_f = 4$ are still quite noisy, even though a very large number of independent signals was used to calculate them.

The main advantage of this presented data analysis technique is that it does not require many consecutive frames as they are required for a Fourier analysis. The frequency is estimated by using many independent measurements. As little as 3 consecutive frames are enough which drastically re-

duces the requirements for the camera system. At $N_f = 3$ the sensitivity on f_B and also on the noise is quite large. But already at $N_f = 4$ signals with $f_B/f_s = 5\%$ can be measured if the measurement range is reduced to $1/8 < f/f_s < 3/8$, and the system is set up such that N_p^{min} is larger than 10. Such fluctuations correspond to 20% of the measurement range. The independent measurements used to calculate the autocorrelation do not necessarily have to be from independent measurements taken over time, neighboring pixels can also be used. By using neighboring pixels the spatial resolution will be reduced in exchange for a higher temporal resolution.

Another advantage of this data analysis is that it does not require computationally expensive FFTs and peak interpolations but only the simple calculation of autocorrelations. For $N_f = 4$ this would even allow to implement it into an SPDA.

Data Analysis of the pOCTii Data

The data analysis of the data acquired with the pOCTii sensor is closely linked to the autocorrelation based technique presented above. This data analysis technique has been published in Experiments in Fluids in 2012 (Meier et al., 2012):

Instead of performing the lock-in detection process of the pOCTii described in Sec. 2.3.2 over a large number of periods N it is only performed over $N = 1$ cycles. The resulting signals I and Q are already mean free, due to the sampling of the camera described in Eqs. 2.43 and 2.43. Combining the two output signals I and Q of the detector into a complex signal C

$$C(t_i) = I(t_i) + jQ(t_i) \quad (2.71)$$

with the corresponding autocorrelation $R(\tau)$ with $\tau = k\Delta t$

$$R(\tau) = \langle C(t_i)C(t_i + \tau) \rangle \quad (2.72)$$

leads to a signal that has similar properties as the filtered signals described in the previous section for $N_f = 4$.

The sampling process and merging of the two signals into C can again be interpreted as filters that are applied to the initial signal S . The PSD of the total filter W_{SPDA} is shown in Fig. 2.35.

W_{SPDA} is zero at $f = 0$ and has an asymmetric power spectral density. Thus the resulting signal C is a zero mean signal with an asymmetric power spectral density. The concept of evaluating the first derivative of the autocorrelation to estimate the mean frequency in the signal is valid for this signal as well. However, the estimate based on Eq. 2.54 is again only valid for $\tau \rightarrow 0$, therefore a calibration function for the estimated mean frequency

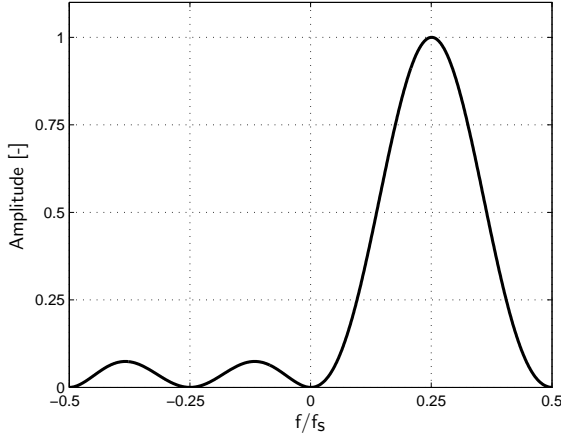


Figure 2.35: Power spectral density W_{SPDA}

$\hat{\nu}$ is needed. This calibration function can be derived by inserting Eq. 2.6 into Eqs. 2.42, 2.43, 2.71, 2.72 and 2.54 and leads to Eq. 2.73.

$$\hat{\nu} = \frac{-1}{2\pi\tau} \arctan(\tan(2\pi f\tau) \sin(2\pi fT_{qp})) \quad (2.73)$$

The calculated mean frequency $\hat{\nu}$ only depends on the integration time T_{qp} and the time delay τ used to evaluate the autocorrelation $R(\tau)$. The influence of different time-delays τ on $\hat{\nu}$ is shown in Fig. 2.36. For $\tau = T_{qp}$ it is a strictly increasing function. Numerical inversion leads to the required relationship between the calculated mean frequency $\hat{\nu}$ and the present signal frequency f . For $\tau = 4T_{qp}$ and $\tau = 8T_{qp}$ the mean frequency shows again an additional wrapping.

Again the sensitivity of $\hat{\nu}$ on N_p and f_B has to be analyzed to assess the applicability of this analysis technique on a flow measurement.

The sensitivity of $\hat{\nu}$ on N_p is shown in Fig. 2.37 for $\tau = T_{qp}$ and in Fig. 2.38 for $\tau = 4T_{qp}$. The bias error induced by the number of signal periods generated by a particle increases as N_p is decreased. For $N_p \geq 25$ the bias error is negligible almost over the whole measurement range. By increasing τ the error becomes smaller as well. For $\tau = 4T_{qp}$ it is smaller than 1% over almost the whole measurement range for $N_p \geq 10$. The system should therefore be set up such that $N_p \geq 10$ and $\tau \geq 4T_{qp}$.

The sensitivity of $\hat{\nu}$ on f_B is shown in Fig. 2.39 for $\tau = T_{qp}$ and for $\tau = 4T_{qp}$ in Fig. 2.40. The bias error generated by $f_B/f_s \geq 12.5\%$ is larger

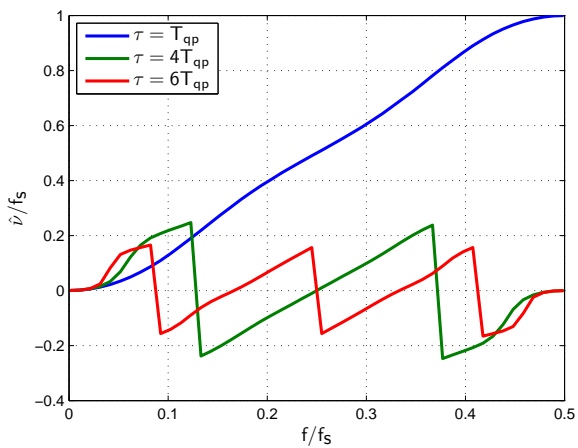


Figure 2.36: $\hat{\nu}$ as a function of the real frequency f for different time delays τ .

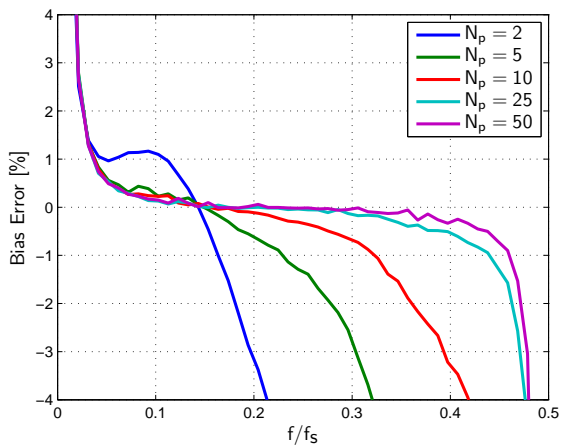


Figure 2.37: Bias error ϵ for different N_p for $\tau = T_{qp}$.

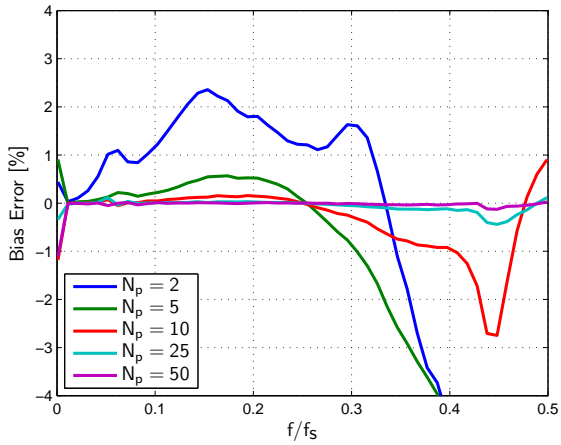


Figure 2.38: Bias error ϵ for different N_p for $\tau = 4T_{qp}$.

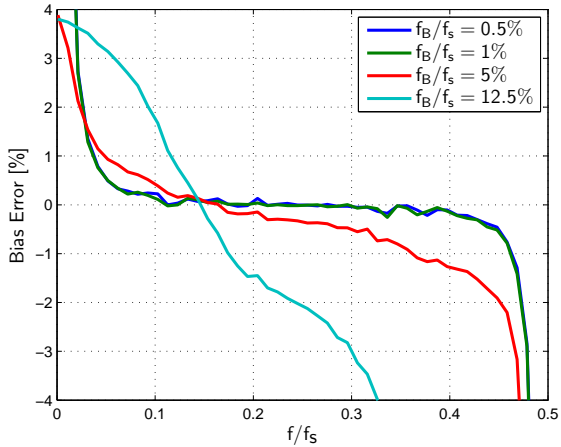


Figure 2.39: Bias error ϵ for different f_B and $\tau = T_{qp}$.

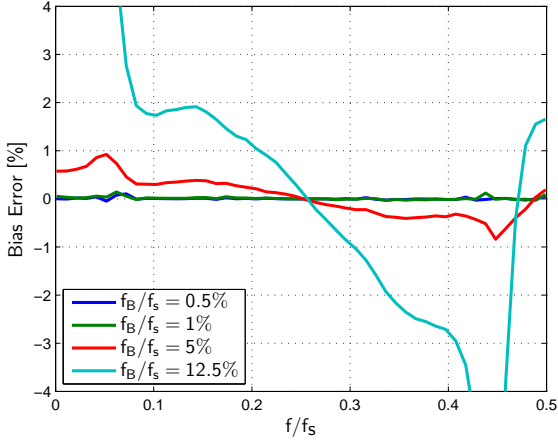


Figure 2.40: Bias error ϵ for different f_B and $\tau = 4T_{qp}$.

than 1% for most of the measurement range for both τ . For $f_B/f_s \leq 5\%$ the error is smaller than 1% for $\tau = T_{qp}$ over most of the measurement range. For $\tau = 4T_{qp}$ the error is smaller than 1% over the whole range.

The standard deviation normalized by the measurement range of \hat{v} at $f = 0.5f_D$ for $\tau = 1, 4$ and 6 is shown in Fig. 2.41 as a function of the number of image pairs from the pOCTii needed. The standard deviation drops very quickly below 1% for all time delays τ . Not much more than 25 image pairs are needed. Those 25 image pairs roughly correspond to the 128 images needed for a converged result in the autocorrelation based analysis as each image pair consists of 4 individual images.

This data analysis scheme is attractive for the pOCTii as it can detect a complete range of frequencies without a systematic and time consuming frequency sweep, but it requires a set of image pairs acquired with a small time delay τ . Those image pairs can be two consecutive images of one pOCTii. The time delay τ is then limited by the frame rate of the pOCTii of max. 5000 fps. Alternatively the image pairs can be acquired using two pOCTiis with one detector array operating with a fixed delay with respect to the other.

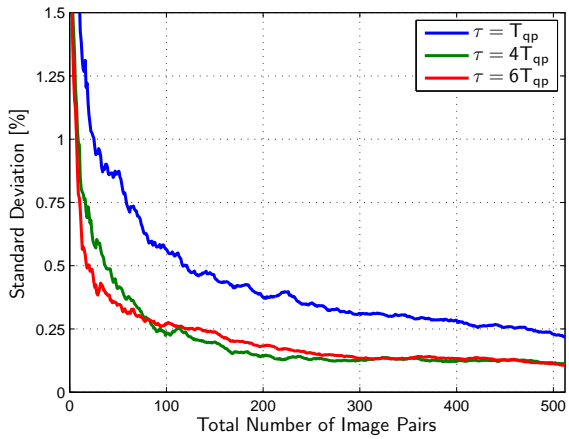


Figure 2.41: Convergence of $\hat{\nu}$ for different τ at $f = 0.5f_D$, $f_B/f_s = 5\%$.

3 Measurements

3.1 Introduction

Based on the planar extensions presented in Sec. 2.2 different measurement systems have been developed for HDGV and ILDV. Several measurements performed with these systems are presented in this section and their applicability to measure flow velocity distributions is examined.

The different systems are presented in chronological order and therefore document the development of the measurement technique. The development starts with a very simple HDGV setup without frequency pre-shift and using one pOCTii SPDA to detect the Doppler signal. This experiment proved the possibility to measure planar velocity distributions using optical heterodyning. From there the system is step-wise extended into the final setup using a conventional high speed camera and frequency pre-shifting. With this system the different aspects of the data analysis and the optimized setup requirements of the system could be analyzed. The results presented in Sec. 3.3 and Sec. 3.4.1 have been published in Experiments in Fluids (Meier et al., 2009, 2012).

As many of the components are used in more than one of the measurement systems, those reoccurring components are first briefly characterized.

3.2 System Components

3.2.1 Light Source

A Verdi V5 laser from Coherent Inc. is used as light source for all the experiments. It is a diode pumped solid state CW-laser, emitting light at a wavelength of 532 nm with an adjustable power of up to 5.5 W. The main properties of the laser are listed in Tab. 3.1. The advantage of this laser is that it offers a very long coherence length of approximately 60 m at a fairly high output power. This long coherence length allows its use for HDGV, but it also simplifies the setups of the ILDV measurements as no care has to be taken regarding the different optical path lengths in the system to create the measurement plane.

Table 3.1: Specifications of the Coherent Verdi V5.

| Parameter | Value |
|----------------|-------------|
| Output Power | 0.5-5.5 W |
| Wavelength | 532 nm |
| Linewidth | 5 MHz |
| Beam Diameter | 2.25 mm±10% |
| M ² | <1.1 |

3.2.2 Frequency Shifting

As described in Sec. 2.1.3 it is necessary to shift the frequency of the reference beam in HDGV or one of the two illumination directions in ILDV to retrieve the directional sensitivity of the measurement system. In the single point measurement techniques this is usually accomplished using so-called acousto-optic modulators or Bragg cells. For an imaging technique these modulators are not suitable as their shift frequency is in the order of 30-100 MHz. This would introduce a carrier frequency in the signal which is not detectable anymore, even with the fastest high speed cameras. To achieve the necessary small frequency shifts in the order of 0-250 kHz either two Bragg cells running at different frequencies or an electro optic modulator (EOM) can be used. Using two Bragg cells has two disadvantages: By changing the shift frequency also the deflection angle of the exiting beam changes, which requires a realignment of the optical setup. Additionally not 100% of the light is frequency shifted.

Using an EOM provides a simpler solution. It uses a non linear optical material, usually a crystal, that changes its refractive index n_x if a voltage is applied to it. By changing the refractive index, the phase ϕ of the light passing through the crystal is shifted. The EOM is therefore characterized by the phase sensitivity S_ϕ , which describes the change of the phase as a function of the applied voltage V :

$$S_\phi = \frac{d\phi}{dV} \quad (3.1)$$

This sensitivity is usually constant and in the order of some mrad/V. To create a frequency shift ν_s with an EOM, the phase has to be continuously changed:

$$E_{in} = Ae^{j(2\pi\nu_0 t + \psi)} \quad (3.2)$$

$$E_{out} = Ae^{j(2\pi\nu_0 t + \phi(t) + \psi)} \quad (3.3)$$

Here E_{in} describes the electromagnetic wave that enters the EOM and E_{out} the exiting electromagnetic waves. The phase ψ is a random phase and $\phi(t)$ the phase shift introduced by the EOM.

Using the phase sensitivity S_ϕ

$$\phi(t) = S_\phi V(t) \quad (3.4)$$

the exiting electromagnetic wave becomes

$$E_{out} = Ae^{j(2\pi\nu_0 t + S_\phi V(t))}. \quad (3.5)$$

Thus to create a frequency shift, the voltage applied to the EOM has to be increased linearly:

$$V(t) = 2\pi Bt \quad (3.6)$$

$$E_{out} = Ae^{j(2\pi(\nu_0 + S_\phi B)t)} \quad (3.7)$$

$$\nu_s = S_\phi B = \frac{1}{2\pi} S_\phi \frac{dV}{dt} \quad (3.8)$$

The frequency shift depends on the rate of change of the voltage and the sensitivity S_ϕ . To generate a constant frequency shift the voltage needs to be increased linearly. This leads quickly to very high voltages. Therefore the EOM is operated using a sawtooth wave generated by a waveform generator. Using a sawtooth wave, the frequency shift can be controlled by the frequency and the amplitude of the sawtooth wave.

The EOM used for the experiments is a Conoptics model M350-50 which has been modified by the manufacturer to be used as a phase modulator. The driver of the EOM was a Conoptics model 302. The properties of the components are listed in Tab. 3.2. To generate the sawtooth wave a HP 33120A waveform generator was used.

3.2.3 Camera Systems

High Speed Camera

For the ILDV measurements a Photron Fastcam Ultima 512 is used. It is a standard high speed camera with a resolution of 512×512 pixel and an internal memory of 670 MB. At full resolution the camera can record at 2000 fps. By reducing the resolution the frame rate can be increased up to 32000 fps. The memory allows to record from 2048 consecutive images at full resolution up to 32768 reduced size images at the highest frame rate. The main properties of the camera are listed in Tab. 3.3.

Table 3.2: Specifications of the frequency shifting system.

| Parameter | Value |
|-------------------|--------------------|
| Phase Modulator | Conoptics 350-50 |
| Phase Sensitivity | 7 mrad/V at 500 nm |
| Crystal Length | 50 mm |
| Clear Aperture | 3.1 mm |
| Driver | Conoptics 302 |
| Input level | $2 V_{p-p}$ |
| Output Voltage | $800 V_{p-p}$ |
| Frequency Range | 0–1 MHz |

Table 3.3: Specifications of the Photron Fastcam Ultima 512.

| Parameter | Value |
|-------------------------|------------------------|
| Sensor Size | 8.2 mm \times 8.2 mm |
| Sensor Resolution | 512 \times 512 |
| Pixel Pitch | 16 μ m |
| Fill Factor | 60% |
| Sensitivity | 10-bit |
| Memory | 670 MB |
| Resolution at 2000 fps | 512 \times 512 |
| Resolution at 4000 fps | 512 \times 256 |
| Resolution at 32000 fps | 512 \times 32 |

Table 3.4: Specifications of the pOCTii sensor.

| Parameter | Value |
|-----------------------------|------------------------------------|
| Sensor Size | 9.150 mm \times 9.490 mm |
| Resolution | 144 \times 90 |
| Pixel Pitch | 50 μ m \times 83.5 μ m |
| Photo Diode Dimension | 44.15 μ m \times 9.9 μ m |
| Fill Factor | 10% |
| Max. External Frame Rate | 5000 fps |
| Max. Demodulation Frequency | 50 kHz or 300 kHz |

The advantage of using this camera is that it allows to simulate all the cameras mentioned in Sec. 2.3, except the DVS. Therefore all the data analysis techniques can be tested and compared with each other using the data acquired with this camera. Additionally it is also used for the comparative PIV measurements.

Parallel Optical Coherence Tomography Imager – pOCTii

The pOCTii SPDA is used for the HDGV measurements as it offers the required high dynamic range of 86 dB due to its offset compensation. Also, the first steps in ILDV were performed using this sensor. Its properties are listed in Tab. 3.4. From this sensor two different versions were used: The first version of the sensor is mounted on a comparatively large interface board as shown in the setup in Fig. 3.3. This version only allows a maximum demodulation frequency of 50 kHz and the storage of 300 images. The second version uses an improved interface board which is much smaller. This version allows a demodulation frequency of up to 300 kHz and the storage of 500 images. It has only been used in the dual sensor pOCTii camera system.

Dual Sensor pOCTii Camera

An ILDV/HDGV system using only a single pOCTii has one main problem. The algorithm to determine the frequency of the signal requires image pairs with a small time delay τ between them. This time delay between two images in a single detector system is determined by the external frame rate of the sensor. It therefore limits the setup as the signal generated by a single particle needs to be long enough so that it is present on both frames.

To avoid this limitation a system using two pOCTii sensors in one camera system has been developed. Such a system eliminates the problem as

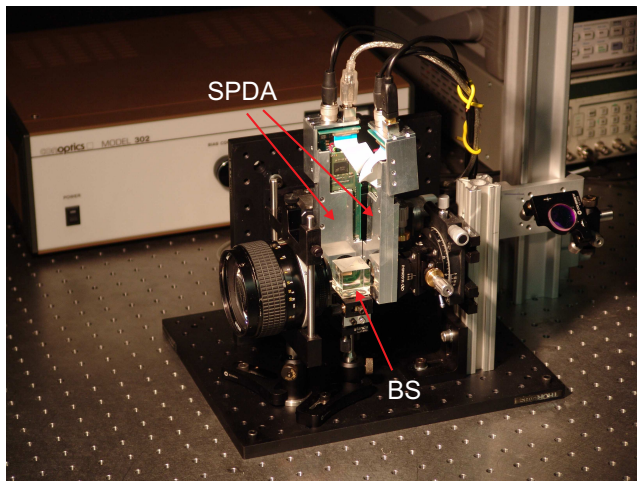


Figure 3.1: Dual pOCTii SPDA camera system.

the two sensors can acquire the images with much smaller time delays between the two images. With smaller time delays the crossing angle between the laser sheets can also be reduced since the time the signal needs to be persistent is reduced too. A close-up of the camera system is shown in Fig. 3.1. The light from the scene is imaged into the camera system using a single lens. Inside the camera system a non-polarizing beam splitter divides the light for the two SPDAs. The beam splitter is mounted on a rotation (Standa, 7R128) and a tilt stage (Standa, 5OM111) for a coarse alignment of the two sensors with respect to each other. The fine alignment of the detectors is done using micro positioning stages with sub-pixel precision relative to each other in order to assure that the corresponding pixels acquire the same signal from the scene. For the translational positioning one of the sensors is mounted on a fiber coupling stage with a sensitivity of $0.2\ \mu\text{m}$ (Standa, Flexure Stage 7TF2). For the rotational positioning the other sensor is mounted on two goniometric rotation stages (Newport, GON40) with a resolution of $5\ \text{arcsec}$ and a platform rotation stage (Edmund Optics, NT55-029). The goniometric setup allows to rotate the sensor around its center and therefore simplifies the adjustment.

The pixel pitch of the pOCTii is large enough such that it can be detected with a normal camera using a macro lens. Therefore the sub pixel accuracy of the alignment can be achieved optically. To adjust the time delay τ between the two sensors, a Stanford Research Systems SRS DG535 digital

delay generator is used.

The main drawback of this two sensor camera is its low sensitivity to light: The fill factor of the individual pOCTii sensors is already only 10%. By using two of them inside a camera only 5% of the light that enters the camera reaches the individual pixels and 90% of the light is lost. This could be improved by using micro lens arrays in front of the sensor. However, the micro lens arrays supplied by the manufacturer are optimized for microscopic applications. For non microscopic imaging tasks these micro lens arrays do not improve the sensitivity of the sensor.

3.3 Heterodyne Doppler Global Velocimetry

Two experiments are presented using the reference beam setup. The first compares the measured velocity distribution of a rotating disk with its true velocity. This experiment is well suited to validate the measurement technique. The second experiment involves the measurement of the velocity distribution in a buoyant plume above a heated resistor, validating the method in a real flow.

Figure 3.2 shows a typical HDGV setup as it was used for the experiments: The source laser beam of the CW-laser is split into two parts using a Fresnel beam sampler. One beam, containing 95% of the optical power, is coupled into a fiber optic delivery system. Different front-ends can be attached to the system depending on the illumination requirements. The reference beam containing the remaining 5% of the power is redirected towards the camera using several mirrors. Figure 3.3 shows a close-up of the camera. The camera lens (Nikon 105mm f/2.8) images the scene onto the pOCTii detector, while a separate two-lens system is used to expand the reference beam to cover the same detector area. The beam splitter is used to overlay the light from the scene and the light from the reference beam resulting in an effective reference beam power of approx. 1-2%.

This open setup is not a problem for the pOCTii sensor, as its background suppression eliminates any unmodulated stray light. In addition it easily allows to tilt the lens with respect to the sensor for the Scheimpflug arrangement.

3.3.1 Rotating Disk Experiment

The setup shown in Fig. 3.2 was used to measure the (known) velocity of a rotating disk. To illuminate the disk, a collimator front-end was attached to the fiber optic delivery system. The resulting expanded laser beam had a diameter of 50 mm and the power of the laser was set to 0.5 W. The measured area on the rotating disk was roughly $20 \times 40 \text{ mm}^2$ and the

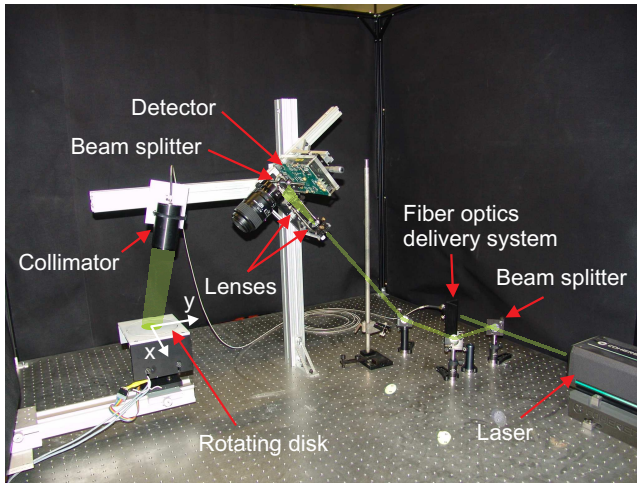


Figure 3.2: Setup of the HDGV measurement system of the rotating disk experiment.

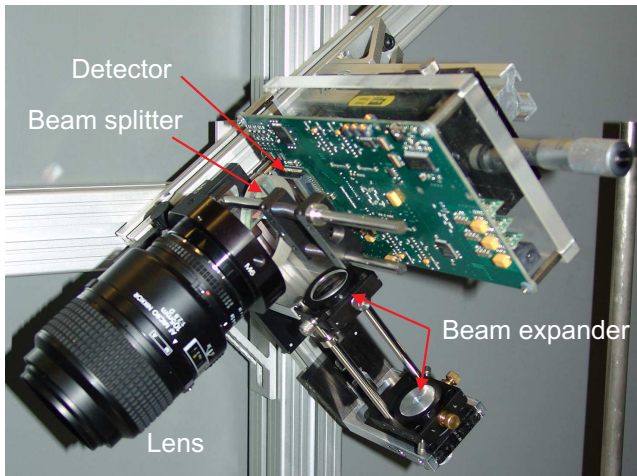


Figure 3.3: Close up of the Doppler camera system.

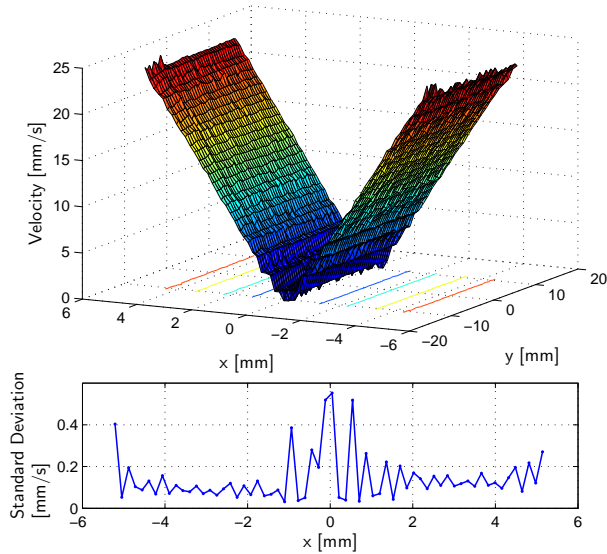


Figure 3.4: Top: Velocity distribution of the measured projected velocity of the rotating disk. Bottom: Standard deviation of the measurement.

rotational frequency of the disk was set to 0.73 Hz. The demodulation frequency f_D of the pOCTii was set to 13.02 kHz averaging over $N = 1$ periods of the lock-in process. For the correlation averaging 300 images were recorded. The data is then analyzed using the autocorrelation based analysis presented in Sec. 2.4.2. The time delay τ between two frames was $8T_{qp} = 1/(4f_D)$.

The resulting velocity map is presented in Fig. 3.4 (top). It shows the expected linear distribution: The projected velocity is constant on straight lines and increases linearly towards the outside of the disk. It also shows the directional ambiguity of the velocity measurement in a setup without EOM. Figure 3.4 (bottom) shows the standard deviation of the measurement calculated along the direction with constant velocity. Except for the very low and high velocities the standard deviation is below 0.25 mm/s. This corresponds to a standard deviation of 250 Hz for the frequency estimation or less than 1% of the maximum detectable frequency. The increasing standard deviation towards the lower and upper end of the measurement

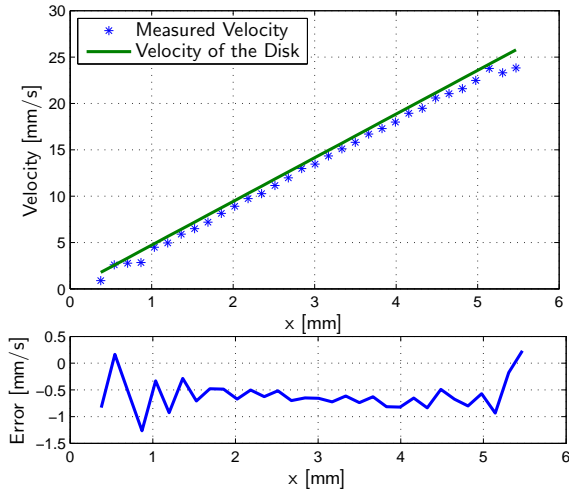


Figure 3.5: Top: Comparison of the measured and the true velocity of the rotating disk. Bottom: Error of the velocity measurement.

range is related to the detected amplitude shown in Fig. 2.21 in Sec. 2.3.2 for $N = 1$. The I-Q demodulation of the detector acts as a band-pass filter even when the signal is averaged only over $N = 1$ cycle. High and low frequencies are damped and the signal-to-noise ratio drops. Figure 3.5 compares the true velocity of the rotating disk along a line with the measured velocity. At the top the figure shows the measured velocities and the true velocity of the disk while the bottom part shows the error of the measurement. Although all the calibration parameters of the system were only measured and not calibrated by an independent measurement, the velocity measurement shows a good agreement. The calculated error indicates that the slope is matched very well, but there is a bias of -0.5 mm/s.

3.3.2 Buoyant Plume Experiment

The setup shown in Fig. 3.6 was used to measure the velocity above a heated resistor. The resistor was placed in an acrylic glass tube which was closed at the top and the bottom, and the flow was seeded using smoke particles generated by smoke sticks. For this experiment the scene was illuminated with a planar laser sheet using a light sheet front-end at the

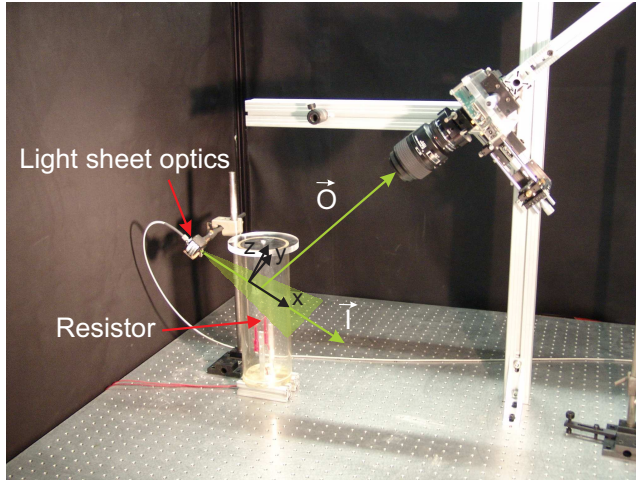


Figure 3.6: Setup of the buoyant plume experiment.

fiber optic delivery system with a Powell lens. The geometrical arrangement of the observation \vec{O} and illumination \vec{I} directions was chosen such that $\vec{\Sigma}$ points vertically upwards. Therefore the detected Doppler shift corresponds to the vertical velocity component of the flow. The output power of the laser was increased to 4 W and the demodulation frequency f_D was set to 4.35 kHz, performing the lock-in detection over $N = 1$ periods. With this demodulation frequency the time delay resulted to $\tau = 6T_{qp} = 3/(2f_D)$. For the averaging 300 images were recorded.

The resulting velocity distribution is shown in Fig. 3.7. The shape of the plume is clearly visible. Due to the asymmetric setup and the elongated shape of the heat source the measured flow distribution is not symmetric either. The directional ambiguity of the technique can be noticed again in the right part of the image. The error and standard deviation figures measured in the rotating disk experiment cannot be directly used to assess the accuracy of the plume measurement since a different demodulation frequency and a different geometry were employed. Nevertheless the low standard deviation seen in the rotating disk experiment is also visible in Fig. 3.7 as the data surface is quite smooth.

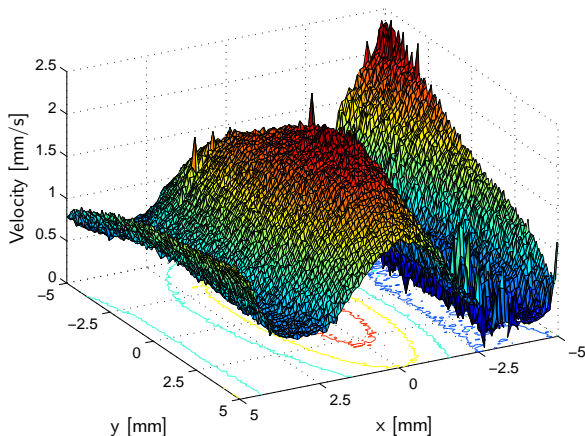


Figure 3.7: Velocity map of the measured projected velocity of the buoyant plume.

3.3.3 Conclusions

The two experiments demonstrate the basic feasibility of the direct demodulation / heterodyning concept using the pOCTii SPDA. The autocorrelation based signal processing offers the possibility to detect complete frequency shift distributions without the need for a frequency sweep of the detection device.

The pOCTii SPDA has demonstrated detection capabilities in a real flow extending to Doppler frequencies of about 4.5 kHz. This corresponds, depending on the viewing geometry and the dominant flow direction, to a detectable velocity range of about 3 mm/s. This is sufficient already for a number of microfluidic applications. For higher flow velocities the available power of the laser was too low as they require higher demodulation frequencies. Higher demodulation frequencies lead to shorter integration times and for integration times shorter than 57.5 μ s there was not enough light left to be detected. The rotating disk experiment demonstrated that with sufficient power Doppler frequencies up to 26 kHz can be detected. With the maximum demodulation frequency of 250 kHz of the second version of the pOCTii, Doppler shifts up to 500 kHz could be measured. For the geometrical arrangement of the illumination and observation direction, as it was used in the present experiments, those Doppler shifts correspond

to a velocity of approx. 0.2 m/s.

3.4 Imaging Laser Doppler Velocimetry

While the HDGV experiments presented in the last section demonstrate the basic feasibility of the heterodyning concept, the velocity range that can be measured with this setup are very limited. Those limitations can be avoided by using a dual light sheet setup as described in Sec. 2.2.2.

At the beginning ILDV was also performed using the pOCTii SPDA and the dual sensor setup described in Sec. 3.2.3 was developed for that purpose. During the experiments with the SPDA it became evident that a normal HSC can be used for the measurements as well. For the final setup which is presented in Sec. 3.4.2 only the HSC was used, as the sensitivity of the dual sensor SPDA camera was too low for a flow measurement.

3.4.1 ILDV with the pOCTii SPDA

Two experiments are presented in this section. The first demonstrates the feasibility of a flow measurement using ILDV with one pOCTii SPDA: The velocity distribution of a free jet is measured simultaneously with ILDV and PIV. Also a first use of a high speed camera to perform an ILDV measurement is presented. The second experiment presents a more complex setup using the dual pOCTii SPDA camera and the EOM to eliminate the directional ambiguity. The benefit of such a system is demonstrated by measuring the velocity distribution on a rotating disk.

Free Jet Experiment

To demonstrate the feasibility of a flow measurement using ILDV with one pOCTii or a high speed camera, the velocity distribution of a free jet is measured simultaneously with ILDV and PIV. The setup used for this experiment is shown in Fig. 3.8. The experiment is performed inside an acrylic glass cube (side length 1 m). This allows for a homogeneous and continuous seeding of the jet and the quiescent air around it and the acrylic glass walls allow for an easy optical access for the illumination and the cameras. The jet is generated using a fan at the inlet of the black tube located at the bottom of the acrylic glass cube. The flow is then redirected by 90° to obtain a vertical jet. This redirection is necessary to have a long enough inflow in order to reduce the influence of the fan on the flow profile and to keep the jet nozzle close enough to the bottom of the acrylic glass cube to have a large enough measurement area above. The vortices generated in the flow by the 90° bend are suppressed by a honeycomb grid right after the bend.

Nevertheless, the bend arrangement influences the resulting jet profile as will be seen in the results. The two cameras used for the simultaneous ILDV and PIV measurements are located outside the acrylic glass cube. The SPDA on the left is equipped with a Nikon 85mm f/1.4 lens. Due to its low fill factor of only 10% a very shallow observation angle of 25° is necessary to receive enough light from the forward scattering particles. To keep the complete light sheet in focus, the sensor and the lens are set up in a Scheimpflug imaging arrangement. The high speed camera equipped with a Tokina 28-70mm f/2.8 lens for the PIV measurements can be placed with a less extreme observation angle of approx. 80° . Nevertheless a Scheimpflug optical arrangement is necessary as well. The flow is illuminated from the right using two cylindrical lenses. A close up of the optical setup is shown in Fig. 3.9. The laser beam of the CW-laser is split up into two separate beams using a 50:50 beam splitter (BS) and then redirected using several mirrors to two cylindrical lenses (CL, $f = -50$ mm) which expand the two laser beams to light sheets with a thickness of approx. 5 mm and cross them inside the acrylic glass cube. With the cylindrical lenses placed above each other generating vertical light sheets this arrangement corresponds to the co-planar light sheet geometry in Fig. 2.10. Thus one of the in-plane components namely the z-component of the velocity can be measured. The measurement area is approx. 180×40 mm² and located 200 mm above the orifice of the jet. The crossing angle between the two illumination directions varied over the field of view from 2.1° to 2.3° .

The volume inside the acrylic glass cube is seeded using a Laskin nozzle generating particles with a diameter of approx. 1 μ m. The seeding density has to be kept as low as possible: There should be just enough particles in the measurement volume to generate a detectable continuous signal. Increasing the seeding density above this level does not improve the signal quality for the ILDV measurements but make the comparative PIV measurement impossible.

For the measurement the HSC camera recorded 512 images with a frame rate of 500 fps. The SPDA was set to a demodulation frequency f_D of 4 kHz and recorded 299 images with a frame rate of 2000 fps resulting in a time-delay $\tau = 8T_{qp} = 500$ μ s. After the measurement a checkerboard target for the optical calibration of both measurement systems was placed inside the acrylic glass cube and recorded with both cameras. With the checkerboard target inside the cube the crossing angle between the two illumination directions is measured at the edge of the target by measuring the separation between the two light sheets right at the two cylindrical lenses and the distance to the edge of the target.

The data obtained by the pOCTii is then processed as described in Sec. 2.4.2 to obtain the signal frequency for each pixel. Using the checker-

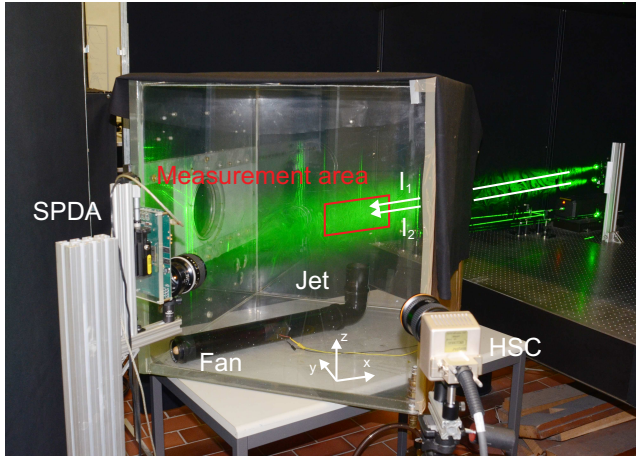


Figure 3.8: Setup of the simultaneous ILDV and PIV measurement.

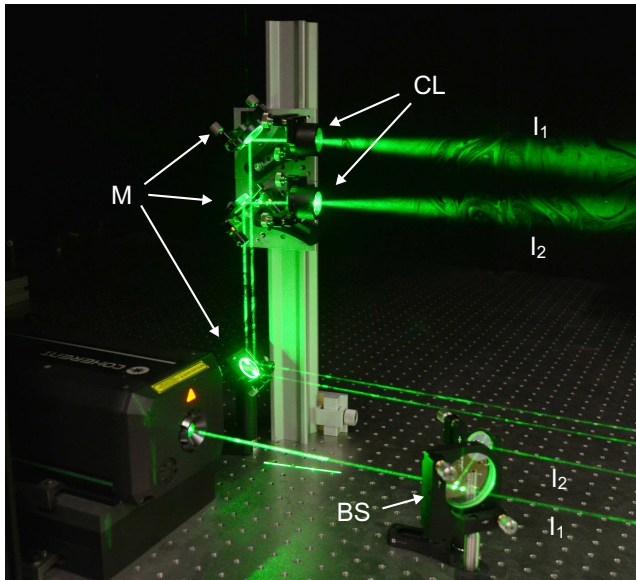


Figure 3.9: Close up of the illumination of the simultaneous ILDV and PIV measurement. I_1, I_2 : Illuminating laser beams, BS: Beam Splitter, M: Mirrors, CL: Cylindrical lenses.

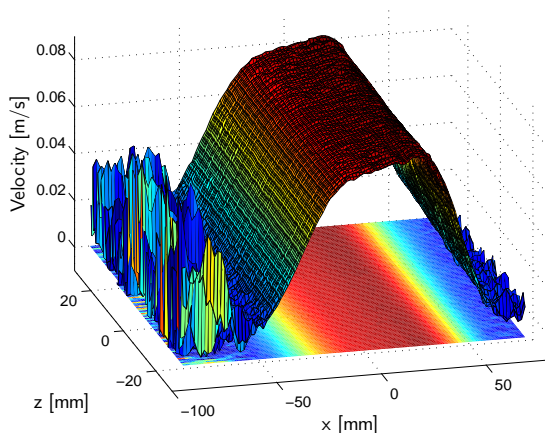


Figure 3.10: Measured velocity distribution of the jet using ILDV.

board target the local angle between the illumination directions is calculated for each pixel to convert the signal frequency into a velocity, and the measurement data is mapped onto a regular coordinate system.

The PIV analysis of 30 independent image pairs acquired with the HSC is performed using the commercial software PIVView (PIVTec, Germany). The average pixel shifts obtained from the PIV analysis are converted into velocities and mapped onto the same regular coordinate system as the ILDV data using the checkerboard target reference data.

The result of the ILDV measurement is shown in Fig. 3.10. The shape of the jet is clearly visible, it is slightly asymmetrical due to the 90° bend at the bottom of the cube. Due to its low velocity the jet is essentially laminar and its shape changes only slightly along the z -axis. On both edges of the jet, where the velocity drops to zero, the signal becomes noisy. This is due to the fact that zero velocity creates zero Doppler shift, and the camera noise becomes the dominating part of the signal. The comparison between the ILDV and the PIV measurement is shown in Fig. 3.11. It shows the velocity distribution in a cross section of the jet. For velocities faster than 1 cm/s the ILDV measurement shows a very good agreement with the PIV measurement. For velocities slower than 1 cm/s the disturbance of the ILDV measurement by the camera noise is again visible.

The presented signal processing requires the calculation of the correlation coefficient using a number of image pairs. It is therefore of interest

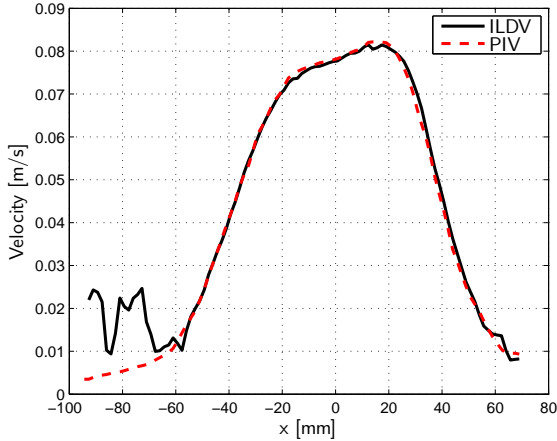


Figure 3.11: Comparison of the ILDV and the PIV Measurements at a cross-section of $z = 14$ mm.

how many image pairs are required for an accurate result. Figure 3.12 shows the convergence of the measured velocity at one point on the jet ($x = -30$ mm, $z = 0$ mm) to its mean normalized by the measurement range of 0.11 m/s. With more than 150 image pairs the fluctuations remain below 1%. Therefore the 300 recorded image pairs are sufficient.

To perform an ILDV measurement using the high speed camera it had to be placed closer to the pOCTii to observe the flow under a shallower angle and the lens was replaced by a Nikon 50mm f/1.4 lens. This was necessary since the frame rate of the high speed camera had to be increased to 16000 fps which reduced the integration time by a factor of 32 compared to the previous PIV measurements. At 16000 fps the resolution of the high speed camera dropped down to 512×64 pixels but in exchange it allowed to record 4096 images. This way the data of the HSC could be used to perform PIV and ILDV analyses using the same data set since sufficient images for a reasonable particle shift for the PIV analysis could be recorded. However, due to the low resolution in one direction the PIV analysis was only possible on three lines. The data of the HSC camera was then analyzed using the Fourier analysis and the autocorrelation based analysis of the SPDA. A comparison of the measured velocities is shown in Fig. 3.13. The velocities calculated using the data of the HSC show a very good agreement for the two frequency analysis algorithms of the ILDV

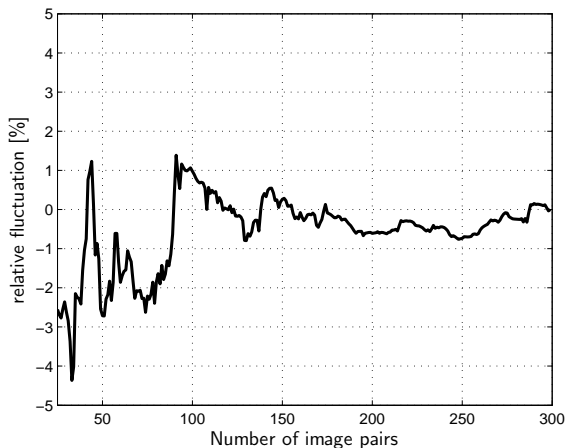


Figure 3.12: Convergence of the measured velocity to its mean.

measurement. The agreement with the PIV reference measurement is also very good, but the PIV measurement shows significant errors in the areas with zero flow velocities as well. This is due to the Doppler signal which is superimposed onto the particle motion creating periodic intensity fluctuations in the signal. Those fluctuations can be averaged out for the PIV measurement for the high velocities by taking the mean of 30 consecutive images to form one single image for the PIV analysis. This does not work for the low velocities since the Doppler frequency is too low and those low frequency brightness fluctuations disturb the PIV analysis for the very low velocities. Other variants of pre-processing the images instead of averaging such as calculating the median or maximum pixel values to eliminate this problem give the same results.

The velocity distribution measured by the SPDA is slightly shifted with respect to the data from the HSC. This shift results from a slight misalignment of the checkerboard target with respect to the light sheet during the calibration process. Apart from this shift, the agreement between the measurements using the HSC and the SPDA is very good again.

Dual Sensor Camera System

An ILDV system using only a single pOCTii as presented above has one main problem. The algorithm to determine the frequency of the signal

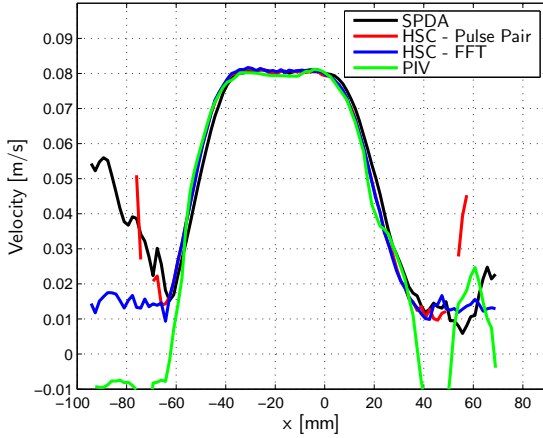


Figure 3.13: Comparison of ILDV and PIV using the pOCTii and the HSC.

requires image pairs with a small time delay τ between them, limiting the velocity measurement range. This time delay between two images in a single detector system is determined by the frame rate of the camera. To further increase the measurement range, the dual sensor SPDA camera system has been developed.

Figure 3.14 shows the setup used for the measurement on a rotating disk using the dual sensor SPDA camera system. The beam of the CW-laser is first passed into a telescope (T) to reduce its diameter and then split up into two parts using a 50:50 beam splitter (BS). One of the two resulting beams is fed into the EOM to shift the frequency of the laser beam. The two beams are then redirected using several mirrors (M), expanded and crossed using a convex lens to illuminate the rotating disk. Thus the disk is not illuminated by a light sheet but each point on the disk receives light from two directions with a crossing angle of approx. 0.15° .

A close up of the rotating disk is shown in Fig. 3.15 indicating the two illumination directions and the measurement area. Both illumination directions are in the y - z plane. This allows to measure the z -component of the velocity. The measured area on the rotating disk was approx. $80 \times 80 \text{ mm}^2$ and the rotational frequency was set to 6 Hz. The camera was set to a demodulation frequency of 16 kHz and recorded 512 image pairs with a time delay of $4T_{qp} = 62.5 \mu\text{s}$. The EOM was set to shift the frequency of one illumination direction by 16 kHz. Therefore signals of particles that are not

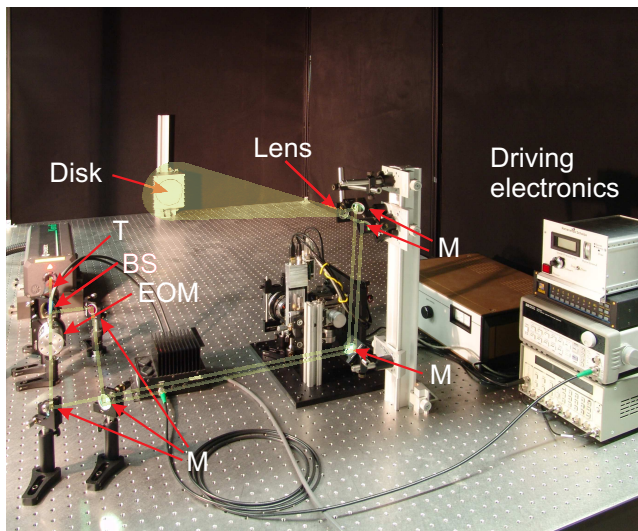


Figure 3.14: Setup of the rotating disk experiment. T: Telescope, BS: Beam splitter, EOM: Electro optic modulator, M: Mirrors.

moving will have an apparent Doppler frequency of 16 kHz. The demodulation frequency of the camera system and therefore the measurement range was limited by the available laser power of 5.5 W. Higher demodulation frequencies lead to shorter integration times and for integration times shorter than 15.625 μ s there was not enough light left to be detected.

Figure 3.16 presents the results of the measurement. It shows the expected linear distribution: The z-component of the velocity is constant on straight lines in the z-direction and increases linearly in the x-direction. Due to the use of the EOM negative velocities are measurable as well, and the noise problem at low velocities has disappeared. Figure 3.17 compares the true velocity of the rotating disk along a line with the measured velocity. The upper plot shows the measured velocities and the true velocity of the disk, while the lower graph shows the error of the measurement. Although all calibration parameters of the system were only measured in situ and not calibrated by an independent procedure, the measurement shows a good agreement. The calculated error is below 0.1 m/s everywhere on the disk surface which is less than 3.5% of the full measurement range of 3 m/s.

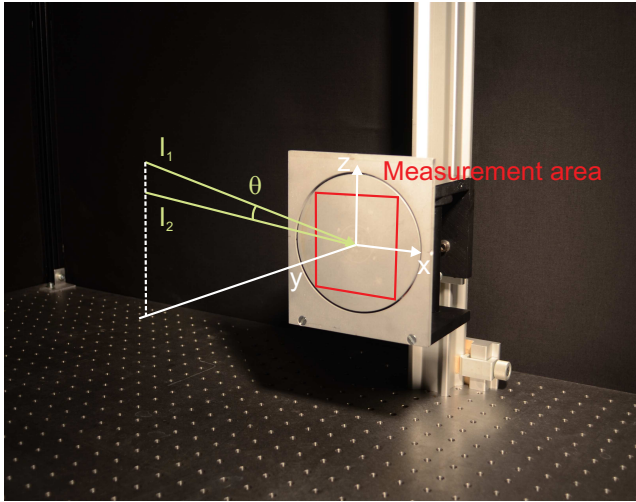


Figure 3.15: Close up on the rotating disk.

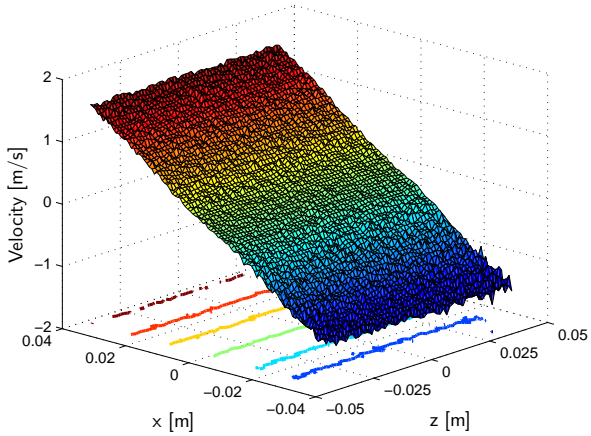


Figure 3.16: Measured z-component of the velocity of the rotating disk.

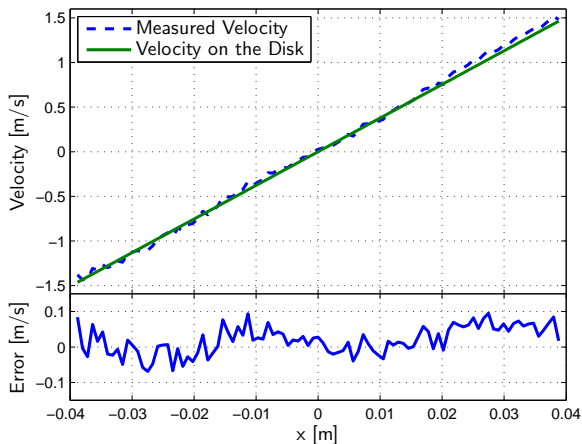


Figure 3.17: Top: Comparison of the measured and the true velocity of the rotating disk. Bottom: Error of the velocity measurement.

Conclusions

The jet experiment demonstrates the basic feasibility of demodulating the Doppler shift of scattered light using a dual light sheet setup and detecting the signal with either the SPDA or a high speed camera to measure flow velocity distributions. The ILDV measurements show a good agreement with reference PIV measurements for both camera systems. Using the co-planar light sheet setup the range of measurable velocities could be extended by more than an order of magnitude compared to HDGV from 2 mm/s to 8 cm/s.

The experiment using the dual sensor camera setup and the EOM demonstrates the further potential of the technique: The measurement range could be extended to 3 m/s and the EOM allowed to shift the operating point of the measurement system. Still, this velocity range can be extended further: The SPDA has only been used at a demodulation frequency of 16 kHz and not yet at its limit of 250 kHz due to the lack of a more powerful laser. With the SPDA running at its maximum speed the measurement range would be extended to about 40 m/s. For a flow measurement this would require a laser with an output power of approximately 180 W.

The ability to use a conventional high speed camera instead of the SPDA, as it is shown in the jet experiment, presents an interesting alternative.

Although conventional high speed cameras are more expensive and their resolution at 1 Mfps is lower than that of the SPDA, they offer two major advantages: Using the SPDA to measure a flow field limits the measurement technique to measuring mean flow fields since about 150 image pairs need to be averaged for the autocorrelation to achieve a converged result. Due to the frame rate of 5000 fps this will always take 25–50 ms. Even for low speed turbulent flows this will be too slow to observe the turbulent structures. And as shown in Sec. 2.4.2, the turbulent fluctuations can also create a bias error in the measurement, dependent on their magnitude, that cannot be corrected. If a high speed camera is used, the measurement of unsteady flows is also possible, despite the need to record a time series of images: Depending on the flow the much shorter acquisition time of the high speed camera might allow to resolve the turbulent time scales and therefore avoid the bias. Additionally also a data analysis procedure can be used that does not generate a bias, even if the turbulent time scale is not resolved, e.g. a short term Fourier analysis. The other advantage of high speed cameras is their fill factor of about 60% compared to the low fill factor of only 10% of the SPDA. This reduces the power requirement for the illumination by a factor of 12 compared to the dual SPDA camera system. The benefits of using standard high speed cameras for ILDV will be presented in the next section.

3.4.2 ILDV with a High Speed Camera

The experiment with the HSC in the previous section demonstrated the possibility to use a standard HSC to detect the Doppler signal. In contrast to the pOCTii SPDA this should allow to measure not only the mean velocity of a turbulent flow but also the instantaneous flow velocities. Therefore a velocity measurement of a turbulent jet is performed. The HSC configuration also allows to test the different algorithms presented in Sec. 2.4. A comparison between the algorithms is shown at the end of the section.

Measurement of a Turbulent Jet in Water

To demonstrate the feasibility of measuring instantaneous turbulent flow fields, the velocity distribution of a turbulent jet in a water tank is measured. Two different setups were tested. For the first setup the co-planar light sheet configuration (Fig. 2.10) was chosen to measure one of the in-plane velocity components of the jet. This setup facilitated a simultaneous PIV measurement using the same high speed camera and the same image data set, therefore allowing a validation of the technique. Figure 3.18 shows the setup used for the in-plane velocity measurement. The laser beam from

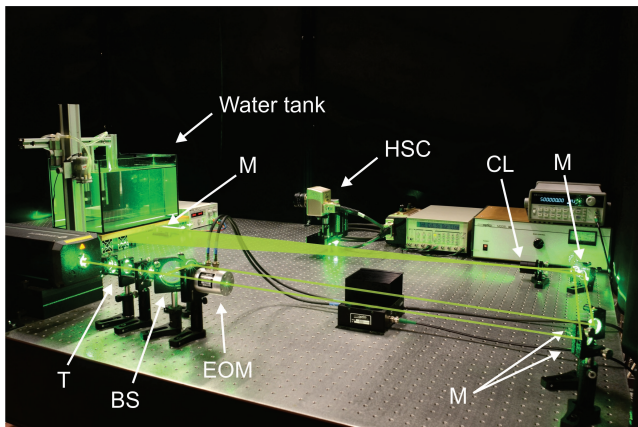


Figure 3.18: Setup of the in-plane velocity measurement of a turbulent jet in water. T: Telescope, BS: Beam splitter, EOM: Electro optic modulator, M: Mirrors, CL: Cylindrical lens, HSC: High speed camera.

the CW-laser is first passed into a telescope (T) to reduce the beam diameter. Then the beam is split up into two beams using a 50:50 beam splitter (BS). One part of the beam is fed into the EOM to shift the frequency of the laser beam. The two beams are then redirected using several mirrors (M) to a cylindrical lens (CL, $f = -25$ mm) which expands the laser beams into light sheets and crosses them. The two light sheets are directed below the water tank where a large front surface mirror redirects them upwards, such that the flow is illuminated by a vertical light sheet. The HSC (Lens: Schneider Kreuznach 25 mm $f/0.95$) is placed in front of the water tank at right angle with respect to the light sheets and images an area of approx. 100×200 mm². A close up of the water tank is shown in Fig. 3.19. The water is seeded with polyamide particles with a diameter of 20 μ m. The seeding density was adjusted to allow for the comparative PIV measurement. For the ILDV measurement alone a higher seeding density would be preferred to obtain a more continuous signal. The jet with a velocity of approx. 10 cm/s is generated using a small water pump and a nozzle with a diameter of 5 mm. With a Reynolds number of 500 the jet is fully turbulent. The two light sheets enter the tank from the bottom and are crossed such that the x-component of the velocity can be measured. The crossing angle is 0.25° at the bottom of the tank. At the top of the tank an anodized aluminum plate is placed below the water surface to suppress the reflections of the laser at the water surface.

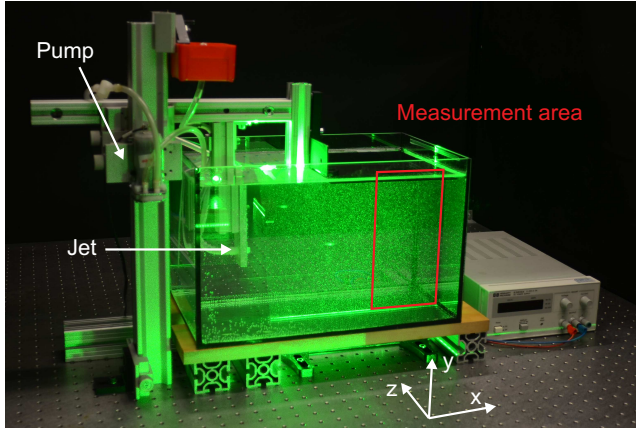


Figure 3.19: Close up on the water tank setup of the in-plane velocity measurement.

The camera was set to a frame rate of 4000 fps. At that frame rate the camera can record 4096 consecutive images at a resolution of 512×256 pixels. The EOM was set to a shift frequency of 1000 Hz, therefore particles that are not moving will generate a signal with a frequency of 1000 Hz. To measure the instantaneous and the mean flow velocities, the camera recorded $M = 32$ independent realizations with a time delay of 0.6 s. In each of the independent realizations 128 consecutive images were recorded. The total signal acquisition time was approximately 20 s.

The ILDV data was analyzed using the autocorrelation based data analysis technique that is implemented on the SPDA (Sec. 2.4.2). The time delay τ was set to $\tau = 4/f_s$ and the 128 consecutive images were used to calculate the autocorrelation to estimate the signal frequency of each independent realization. To account for the spatial variations in the crossing angle between the illumination directions across the y-direction in the tank, a linear model was used to calculate the local crossing angle for each pixel. This local crossing angle was then used to convert the measured signal frequency to the velocity. Each of these 32 independent measurements will give an “instantaneous” velocity distribution. To calculate the mean flow velocities the 32 independent measurements were averaged.

The results of the ILDV measurement are displayed in Fig. 3.20 for the instantaneous flow field and in Fig. 3.21 for the mean flow field. In the mean flow field the shape of the jet in the center of the tank is clearly visible. Due to the walls on the side and at the end of the water tank the jet does

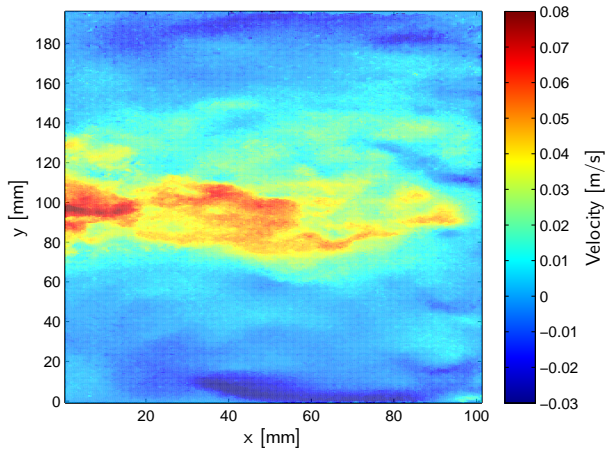


Figure 3.20: Measured instantaneous velocity distribution of the turbulent jet using ILDV with 128 consecutive images.

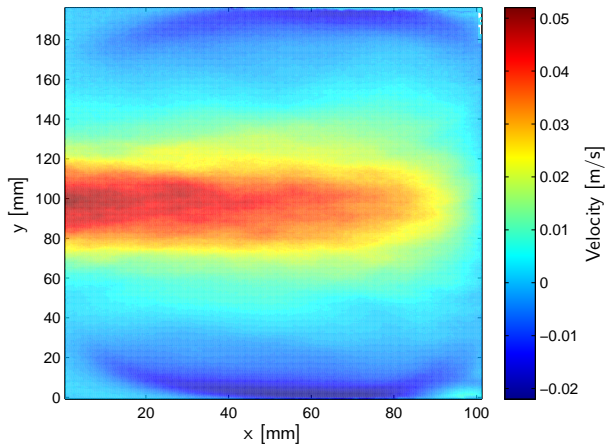


Figure 3.21: Measured mean velocity distribution of the turbulent jet using ILDV.

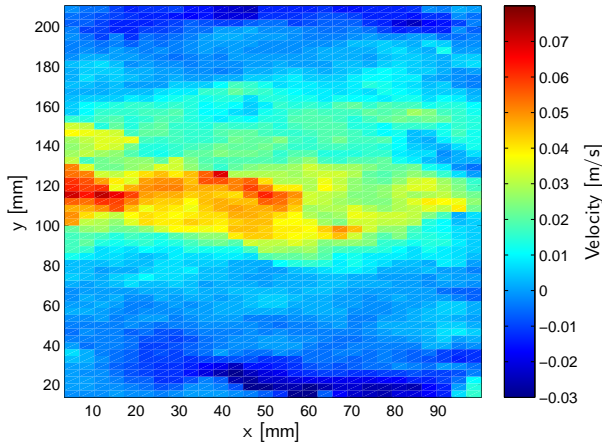


Figure 3.22: Measured instantaneous velocity distribution of the turbulent jet using PIV.

not show any spreading. Instead a drop of the velocity towards the end of the water tank and the back flow at the bottom and at the top can be seen. In the instantaneous flow field the shape of the jet is not as clearly visible any more. Due to the turbulence, the shape of the jet is not as sharply defined as in the mean flow, instead elongated turbulent structures can be identified.

To validate the ILDV velocity measurement the recorded images were also used to compute the flow velocity using PIV. From each of the 32 sets of 128 consecutive images the first 8 images and the last 8 images were averaged to obtain the image pairs for the PIV analysis. This averaging is necessary to eliminate the fluctuating Doppler signal which otherwise disturbs the PIV analysis. The image pairs were then analyzed using PIVView (PIVTec, Germany). The instantaneous and the mean velocity distributions obtained by the PIV analysis are shown in Fig. 3.22 and Fig. 3.23. Comparing the results from PIV with ILDV one can identify the same structures. Especially in the instantaneous velocity distribution the turbulent structures are visible in both measurements. Compared to the PIV measurements the ILDV measurements have a much higher resolution, as PIV uses spatial cross correlations to determine the velocity. The size of the windows used for the cross correlation limits the spatial resolution of the measurement. In contrast ILDV uses the time signal of each pixel

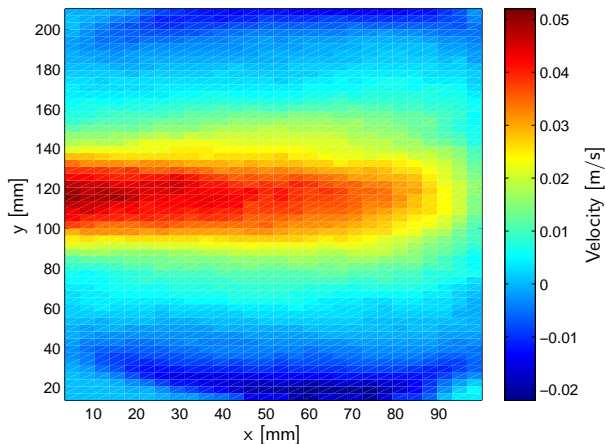


Figure 3.23: Measured mean velocity distribution of the turbulent jet using PIV.

to determine the velocity, thus each pixel gives an independent velocity measurement.

For a more quantitative comparison between the measurement techniques, the mean and instantaneous velocity profiles along a line at $x = 27$ mm obtained with PIV and ILDV are displayed in Fig. 3.24 and Fig. 3.25. The ILDV measurements show a very good agreement with the PIV measurement for both the mean flow and the instantaneous flow measurements, and again the higher resolution of the ILDV measurements are visible.

For the second setup the crossed light sheet configuration (Fig. 2.11) was chosen to measure the out-of-plane velocity component. Figure 3.26 shows the setup used for the measurement. The flow is now illuminated from the side at approx. 20 mm away from the end wall of the tank. The camera is again located at a 90° observation angle and images the area inside the red rectangle of 120×250 mm². The crossing angle, the camera settings and the data analysis technique for the ILDV measurement were the same as for the in-plane velocity measurement.

The measured mean and instantaneous out-of-plane velocity distributions are shown in Fig. 3.27 and Fig. 3.28. The jet in the center is clearly visible in both measurements. At the left and the right side of the tank the areas with the back-flow are visible as well. The instantaneous measurement again shows the turbulent structures of the jet.

A validation of this data using PIV would only be possible using a stereo

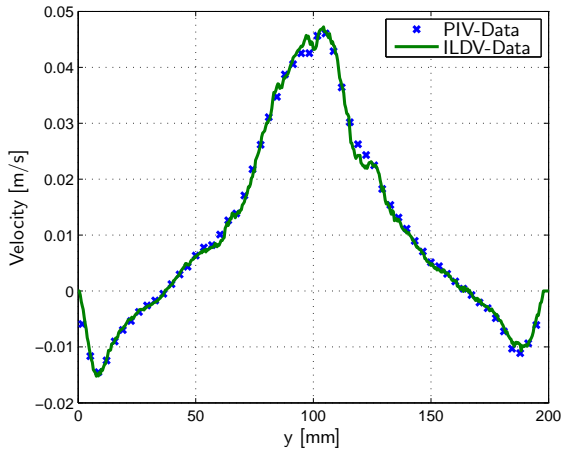


Figure 3.24: Comparison between the measured mean velocities between ILDV and PIV along $x = 27$ mm.

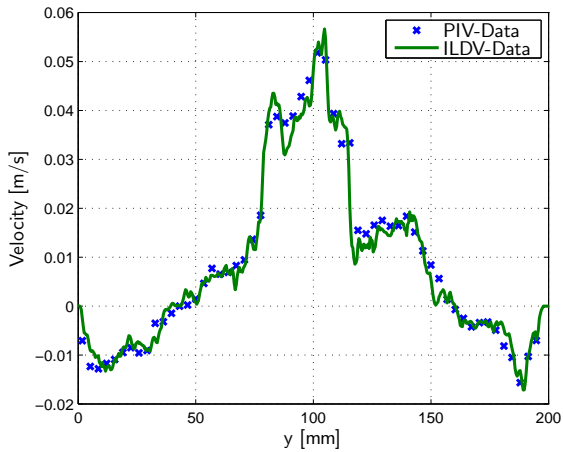


Figure 3.25: Comparison between the measured instantaneous velocities using ILDV and PIV along $x = 27$ mm.

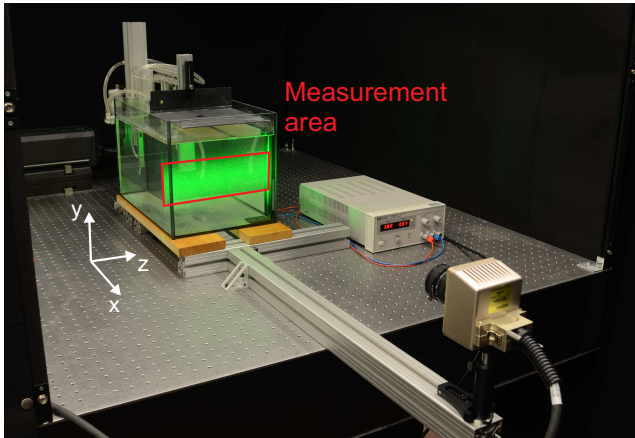


Figure 3.26: Setup of the out-of-plane velocity measurement of a turbulent jet in water.

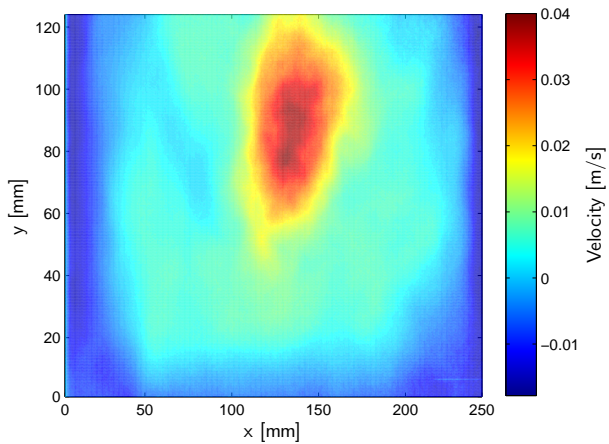


Figure 3.27: Measured mean out-of-plane velocity distribution of the turbulent jet using ILDV.

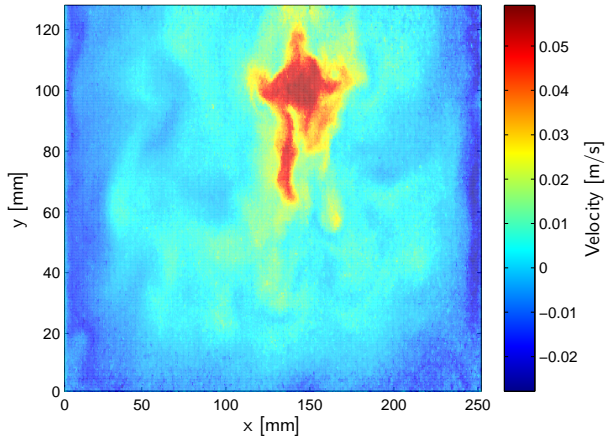


Figure 3.28: Measured instantaneous out-of-plane velocity distribution of the turbulent jet using ILDV with 128 consecutive images.

PIV setup. Nevertheless PIV can be used to analyze this data as well: With PIV the in-plane motion of the particles can be analyzed. A combined ILDV-PIV will then give all three velocity components in the measurement plane. The result of this combined analysis for the mean velocity distribution is shown in Fig. 3.29. The ILDV measurement shows the main structure of the flow and the PIV measurement the secondary flow structures inside the jet.

Comparison of Different Data Processing Algorithms

The setup used for the in-plane velocity measurement of the turbulent jet in water can be used to assess the performance of the different data analysis techniques presented in Sec. 2.4. Using the HSC all the different camera systems presented in Sec. 2.3, except the DVS, can be simulated and the comparative PIV measurements allow to independently validate the results.

Three different measurement series were performed to compare the different data analysis techniques. In the first measurement series the HSC recorded 512 times 8 consecutive frames at 4000 fps. The repetition rate between the recording of the 8 frames was 26 Hz. This time delay allows for a PIV analysis with the successive measurements. With this data set the ability to measure the mean flow velocity using the SPDA-algorithm

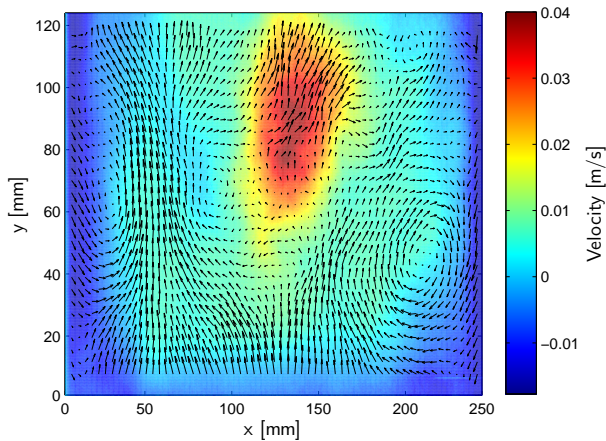


Figure 3.29: Combined ILDV and PIV measurement of the mean flow velocities.

and the Hilbert transform based algorithm with $\tau = 1/f_s$ and $\tau = 4/f_s$ could be tested. It is basically the simulation of the working principle of the pOCTii sensor and the framing cameras where only few consecutive images can be recorded.

The comparison between the velocities measured with PIV and the two different autocorrelation based algorithms introduced in Sec. 2.4 along a line at $x = 27\text{mm}$ is shown in Fig. 3.30 for $\tau = 1/f_s$. To reduce the noise in the results the autocorrelation is not only calculated using the 512 independent realizations but also on a spatial neighbourhood of 3×3 pixels. This increases the number of independent realizations by a factor of 9 and the spatial resolution is only slightly reduced. For $\tau = 1/f_s$ the SPDA-algorithm cannot catch the high velocities at the center of the jet and the Hilbert transform based algorithm overestimates the low velocities at the sides of the jet. These deviations can be either caused by the optical setup of the crossing angle and the magnification of the camera system, such that the number of signal periods a particle generates is too low, or by the turbulence in the flow that generates a finite frequency bandwidth f_B as shown in Sec. 2.4. The turbulence intensity of the jet can be computed from the PIV data. For this flow it is on the order of 15%. This amounts to a FWTM frequency bandwidth $f_B/f_s = 15\%$, and is close to the evaluated value of $f_B/f_s = 12.5\%$ in Fig. 2.32 for the Hilbert-algorithm and Fig. 2.37 for the SPDA-algorithm in the data analysis section. For these f_B a large

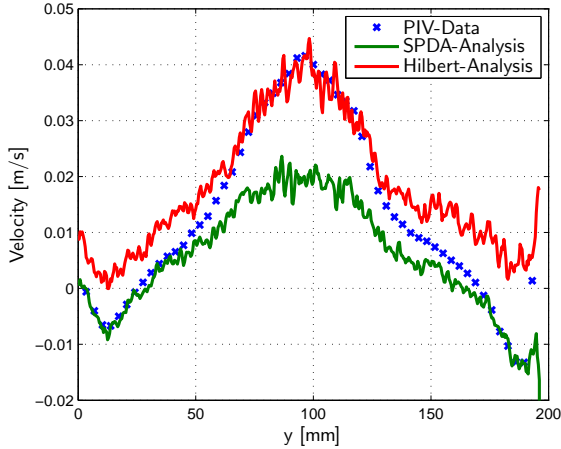


Figure 3.30: Comparison between the SPDA-algorithm, the Hilbert transform based algorithm and PIV along $x = 27$ mm with $\tau = 1/f_s$ for a measurement series with 8 consecutive images and 512 independent realizations.

bias could be expected. Interestingly the bias is roughly in the same range for both techniques and not much larger for the SPDA-algorithm as might be expected. The number of signal periods N_p a particle generates during its passage can be analyzed by looking at the setup: The sensitivity is roughly $10 \text{ kHz}/(\text{m/s})$, the probe volume size is $s = 0.43 \text{ mm}/\text{pixel}$ and $\nu_s = 1000 \text{ Hz}$. Using Eq. 2.21 the minimum number of signal periods amounts to $N_p^{\min} = 4.3$ if the smallest allowed frequency is $f_s/8$. This is also clearly the regime where both techniques generate a large bias as can be seen in the Figs. 2.28 and 2.37. But the flow analyzed has only very low velocities in the negative x-direction. N_p^{\min} is therefore generated by particles passing through the probe volume perpendicular to the sensitive direction. Such particles generate $N_p^{\min} = 8.6$ thus generating a bias smaller than 1%. The measured bias therefore stems from the turbulence intensity of the measured flow.

As shown in Sec. 2.4, this bias can be reduced by increasing τ to $4/f_s$. The results of this analysis are displayed in Fig. 3.31. The bias has completely vanished for both techniques as could be expected. The Hilbert-algorithm now slightly overestimates the velocity. This overestimation of the velocity stems from the used high pass filter F_{HP} . If the same high pass filter is used as in the SPDA-algorithm, i.e. $F_{HP} = [1, 0, -1]$, this error vanishes

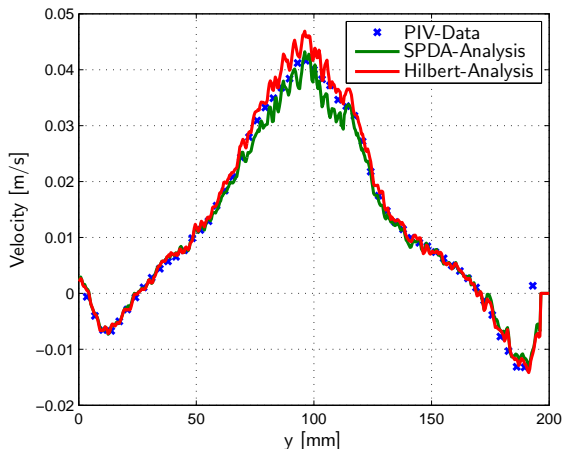


Figure 3.31: Comparison between the SPDA-algorithm, the Hilbert transform based algorithm and PIV along $x = 27$ mm with $\tau = 4/f_s$ for a measurement series with 8 consecutive images and 512 independent realizations.

as shown in Fig. 3.32. The origin of this error appears therefore to be the noise level in the measured signal.

These results show that it is possible to measure the mean flow velocity with only 8 consecutive frames plus averaging over many independent realizations. The number of independent realizations needed for a converged result is shown in Fig. 3.33 for one point in the flow field. Two different curves are displayed for each algorithm. The red and the blue curves show the convergence of the autocorrelation to its mean normalized by the measurement range, with the images used in the order they were recorded. Even after processing 4096 images it does not show convergence. As a comparison the two green curves show the convergence if the samples are used in random order. After 500 images the error is below 1% and after 1000 images the fluctuations are negligible. This indicates that it is the fluctuating flow that generates the fluctuation in the convergence and not the algorithm itself. Thus for a measurement of the mean the chosen repetition rate was simply too high and fewer independent measurements could have been used.

The second measurement which is analyzed, is the one presented in the previous section, where 32 independent realizations consisting of 128 consecutive images were recorded. The 32 independent realization were not

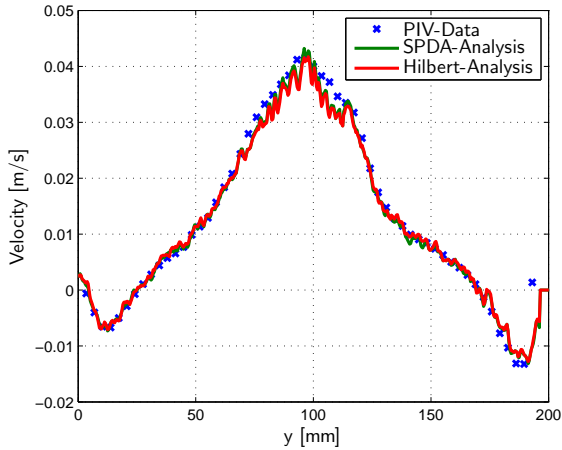


Figure 3.32: Comparison between the SPDA-algorithm, the Hilbert transform based algorithm with a different high pass filter and PIV along $x = 27$ mm with $\tau = 4/f_s$ for a measurement series with 8 consecutive images and 512 independent realizations.

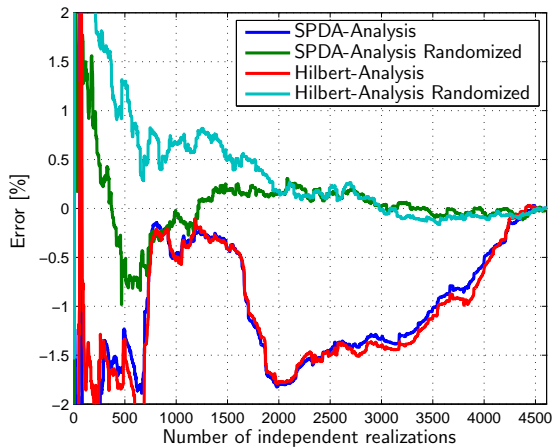


Figure 3.33: Convergence of the autocorrelation of the SPDA-algorithm and the Hilbert transform based algorithm to their respective mean for a single point in the flow field and different ordering of the samples.

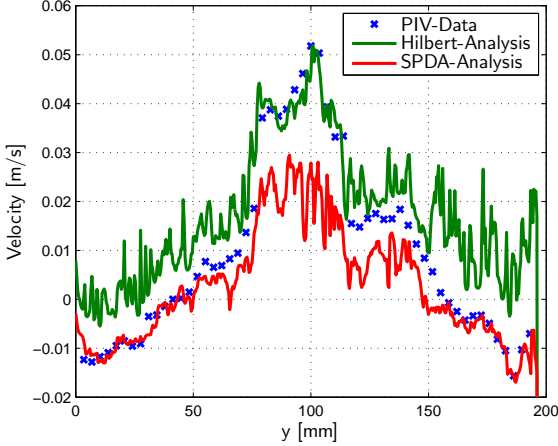


Figure 3.34: Comparison between the SPDA-algorithm, the Hilbert transform based algorithm and PIV along $x = 27$ mm with $\tau = 1/f_s$ for a measurement series with 128 consecutive images.

needed for the analysis. Only the 128 consecutive images were used to calculate the instantaneous velocity distribution. Again the autocorrelation is computed not only in time but also in space on a 3×3 pixel neighborhood.

The results for the two autocorrelation based algorithms for $\tau = 1/f_s$ are shown in Fig. 3.34 for the instantaneous flow field. Again there is a large bias visible although it is a bit smaller than in the measurement with only 8 consecutive frames. The effect of increasing τ is shown in Fig. 3.35 for $\tau = 4/f_s$. The bias has disappeared again and both techniques give a good result.

These results show that it is possible to measure the instantaneous flow velocity using the SPDA-algorithm and the Hilbert transform based algorithm and the difference between the two algorithms is negligible. Therefore the use of the SPDA-algorithm is preferred as it requires a much lower computational effort compared to the Hilbert transform based algorithm.

The result of a Fourier analysis applied on this data set is shown in Fig. 3.36. Surprisingly the Fourier analysis performs much worse than the two other analysis techniques. This can be explained by looking at a typical signal S and its PSD shown in Figs. 3.37 and 3.38. The signal looks quite similar to the simulated signal used in Sec. 2.4.2. The PSD shows the problem of the peak estimation. The peak is very noisy and wide. Detecting

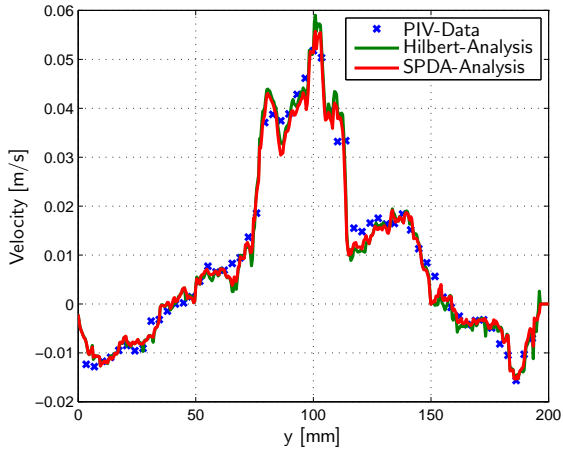


Figure 3.35: Comparison between the SPDA-algorithm, the Hilbert transform based algorithm and PIV along $x = 27$ mm with $\tau = 4/f_s$ for a measurement series with 128 consecutive images.

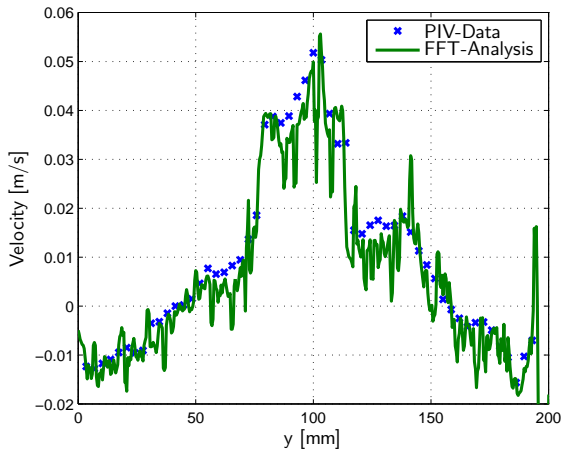


Figure 3.36: Comparison between the resulting velocities for a Fourier analysis applied on the data set with 128 consecutive images and PIV.

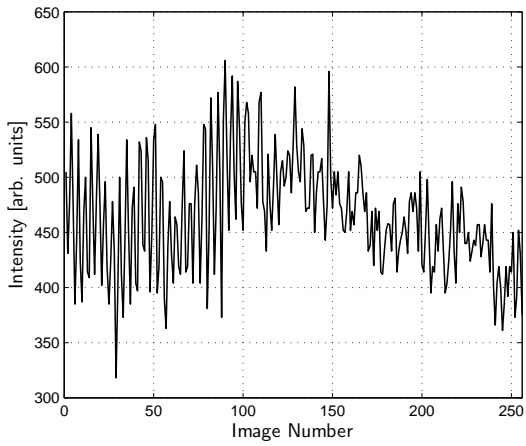


Figure 3.37: Typical signal measured with the high speed camera.

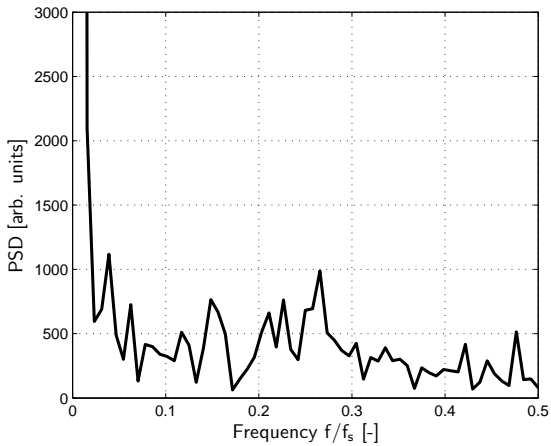


Figure 3.38: “Instantaneous” PSD of the signal measured with the high speed camera.

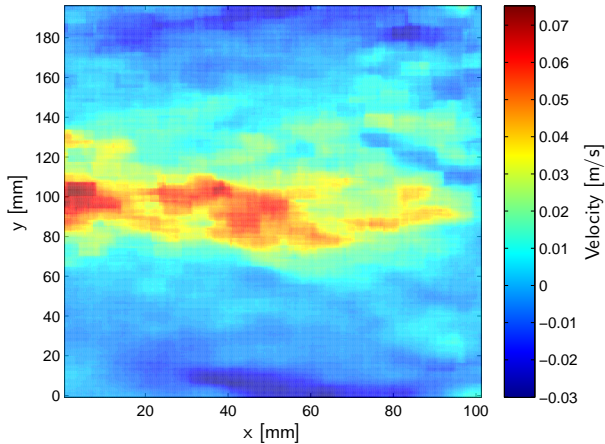


Figure 3.39: Instantaneous in-plane velocity distribution of the turbulent jet using ILDV with spatial autocorrelations calculated using 8 consecutive images on a 16×16 pixel neighborhood.

it and interpolating its position using 3 points will not be a very stable procedure. The reason why the autocorrelation based algorithms work much better on such a data set can be explained through their basic idea: The algorithms estimate the mean of the PSD which is an integral quantity with respect to the PSD itself. This reduces the noise compared to the Fourier analysis where a single peak in a noisy signal has to be detected.

With this data set also the possibility to calculate the autocorrelations in space can be tested. Instead of calculating the autocorrelation with the 128 consecutive images it is calculated on a 16×16 pixel neighborhood using 8 consecutive images. The resulting velocity distribution of this analysis is shown in Fig. 3.39. The spatial resolution is now the same as in the PIV analysis. The different flow structures can be identified as well.

For a better comparison the velocity profiles along a line at $x = 27$ mm are plotted in Fig. 3.40. The green line shows the velocity calculated using 128 consecutive images and the red line the result using the spatial autocorrelation. The curves do not give the same results. This could be expected as the turbulent flow changes over time thus the two techniques average the flow over different times. To compare the techniques the average of the calculated velocities using the spatial autocorrelation over the 128 images is shown as well. The averaged result is very close to the result of the cal-

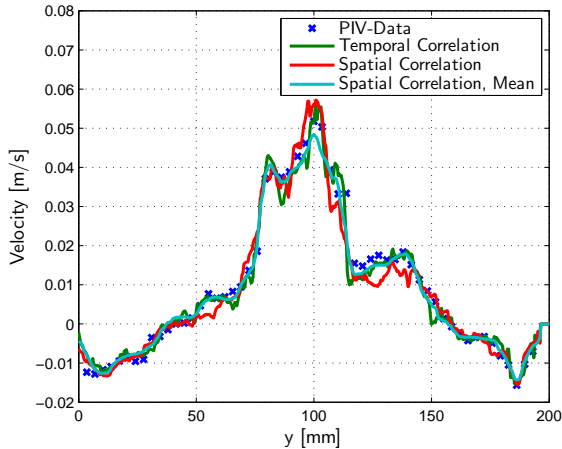


Figure 3.40: Comparison between the data analysis techniques using temporal and spatial correlations and PIV.

ulation using 128 consecutive images. Only the spatial resolution is lost due to the spatial averaging.

The last measurement is performed to see if the 128 images used for the calculation of the autocorrelation are enough for a converged result in the instantaneous measurement. For this a series of 4096 consecutive images was recorded. The convergence of the autocorrelation to its mean, normalized by the measurement range for the SPDA-algorithm and the Hilbert transform based algorithm calculated with 128 consecutive images and $\tau = 4/f_s$ is shown in Fig. 3.41. Using the Hilbert transform based algorithm the convergence data is only available every 128 images and therefore also starts at 128. For both algorithms the convergence rate is fast enough, such that 128 images are just enough to have an error of less than 1%. This also explains the slightly noisy images in the previous section.

Conclusions

The ILDV measurements of the turbulent jet in water showed the benefit of using a conventional high speed camera instead of the SPDA. Not only the mean flow velocity distribution could be measured but also the instantaneous flow field. The comparative PIV measurements showed a very good agreement for the in-plane velocity measurements. Moreover, an out-



Figure 3.41: Relative convergence to its mean of the different autocorrelation based data analysis techniques.

of-plane velocity measurement could also be performed using the crossed light sheets configuration. Both the mean and the instantaneous flow velocity distribution could be measured. While these measurements could not be validated using PIV, the combination of ILDV and PIV allowed to measure all three velocity components in the illuminated plane. In these experiments the crossing angle could be further reduced to a very small value of only 0.25° which allowed to measure a velocity range of 16 cm/s with the high speed camera operating at only 4000 fps. With the fastest cameras available today that offer up to 1 Mfps, this would allow to measure a velocity range of 40 m/s. This makes this technique interesting to be applied in larger facilities e.g. low speed wind tunnels especially to measure the out-of-plane velocity component which is otherwise difficult to obtain. The main problem for such a measurement is the required laser power of about 200 W. Alternatively an image intensifier could be employed.

The comparison of the performance of the different algorithms introduced in Sec. 2.4 showed several interesting results: First, recording only 8 consecutive images and averaging over ≥ 128 independent realizations allows to measure the flow velocity distribution. If the resolution of the camera used is large enough the 128 independent realizations can be extracted from adjacent pixels of the camera. This way the instantaneous flow field can be measured in a very short time. For a mean flow velocity measurement the

128 independent realizations can be recorded over a longer time resulting in a higher spatial resolution.

The comparison between the Hilbert transform based algorithm and the much simpler SPDA-algorithm showed only very small differences. These differences are mainly due to the high pass filter used in the Hilbert transform based algorithm and made the results of this algorithm slightly worse. Therefore using the SPDA-algorithm can be preferred as it is much simpler to implement and performs much faster. The Fourier analysis as a comparison performed much worse. This is mainly due to the very simple approach used for the peak interpolation. A more elaborate approach, for example using a Gaussian distribution which is least-squares fitted to the PSD of the signal, could deliver better results. However, the computational effort of such an approach cannot be justified as the SPDA-algorithm already gives very good results.

Regarding the choice of possible cameras for an ILDV measurement the results show that not only high speed cameras that can record hundreds of consecutive images have to be used. As little as 8 consecutive images are enough to generate the required data. Therefore also the framing cameras and cameras based on on-chip frame storage such as the ISIS-V2 can be used. With the ability to calculate the autocorrelation in space and not over time this technology also allows to measure the instantaneous flow field in a very short time.

4 Conclusions

4.1 Achievements

The objective of this work was to develop a new measurement technique that allows to measure the velocity distribution of a flow field in a plane by using the Doppler shift of the scattered light and optical heterodyning to create a detectable signal. This new technique can therefore be regarded as the planar extension of the well known laser Doppler velocimetry (LDV).

At first, the two most commonly used LDV techniques, namely reference beam laser Doppler velocimetry and dual beam laser Doppler velocimetry (LDV) were analyzed. This analysis indicated the necessary steps to extend those point measurement techniques into planar measurement techniques: How to expand the measurement volume into a planar measurement volume and the requirements on the detection system for a distributed velocity measurement. From these requirements different cameras were identified that could be applied to such a measurement. Among these are high speed framing cameras with frame rates up to 100 Mfps, but also so called “smart pixel detector arrays” (SPDA) that do not just detect the signal but also process it on the pixel level. For these different camera systems an autocorrelation based data analysis technique has been developed. This technique allows to detect the signal frequency using only few consecutive images with a very low computational effort.

The planar extensions were then tested using different measurement systems. At first a simple heterodyne Doppler global velocimetry system (HDGV) was tested. This setup can be seen as the planar extension of the reference beam LDV. With this setup the velocity distributions on a rotating disk and of a buoyant plume were measured. The measurements proved the basic feasibility of measuring velocity distributions using the Doppler shift and optical heterodyning. Nevertheless, the achieved measurement range was limited to some mm/s and a SPDA was needed for the measurement due to the high occurring signal frequencies and the low visibility of the Doppler signal. Also the measurable velocity component is restricted to a slanted out-of-plane velocity component.

To extend this limited measurement range imaging laser Doppler velocimetry (ILDV) was developed, using a dual light sheet illumination setup. This technique can be seen as the planar extension of dual beam LDV. With this method the high signal frequencies and the high dynamic

range that were required to be detected in HDGV could be reduced. ILDV also allows to measure a specific velocity component such as one of the in-plane velocity components or the out-of-plane velocity component.

The capability of this method was then examined on a rotating disk and in two different flow fields. In air a laminar jet was measured and in water ILDV was applied to a fully turbulent jet. During those measurements different camera systems were tested, including a custom developed dual sensor SPDA camera system using two SPDAs in parallel and a conventional high speed camera (HSC). The in-plane velocity measurements in the flow fields were additionally validated using particle imaging velocimetry (PIV) and showed a very good agreement between PIV and ILDV. Using the out-of-plane velocity measurement in combination with PIV a so called 2D3C measurement could be performed, that is a measurement of all three velocity components of the flow field on a plane.

These measurement demonstrated the potential of ILDV to measure instantaneous and mean flow fields and extended the velocity range from HDGV by more than one order of magnitude to approximately 8 cm/s.

The measurements performed on the turbulent jet in water using the HSC also allowed to assess the performance of the different data analysis techniques and the applicability of different high speed camera concepts for an ILDV measurement. The examination of the autocorrelation based data analysis technique showed that as little as 8 consecutive recorded images are enough to estimate the flow velocity, if enough independent measurements are available. It could be shown that these independent measurements can either be consecutive measurements of the flow in time but also neighboring pixels of the camera. This relaxes the requirements on the camera systems tremendously. Framing cameras that can record only 8 consecutive images at up to 100 Mfps with a high resolution can be used as well as conventional HSC that can record hundreds of consecutive images at comparatively low resolutions. Depending on the camera used, this allows to measure either mean or instantaneous flow velocity distributions. Especially the instantaneous velocity distributions can be measured in a very short time if spatial autocorrelations are used.

The measurable velocity range is only limited by the frame rate of the camera and the power of the illumination light source. From the presented measurements it can be extrapolated that using a camera recording at 1 Mfps a measurement range of 40 m/s can be achieved. The derived theory implies that this should be further expandable, if a larger measurement area is examined. This is another promising property of the technique: Since the particles do not need to be resolved as in the displacement based techniques, ILDV should be applicable to large measurement areas. Additionally the frequencies that have to be detected can be reduced as well when measuring

larger areas. This should simplify the measurement on larger areas even more.

4.2 Outlook

The presented experiments have shown that ILDV works in water and in air. The camera and laser used limited these measurements to comparatively slow flows. To increase this measurement range a faster camera and a more powerful laser are needed. The performance analysis of the different data processing techniques showed that several different high speed camera concepts can be used for ILDV. The most obvious and safest choice to improve the system is simply a more recent and therefore faster conventional high speed camera than the one used for the experiments. However the resolutions of these cameras at high speeds is rather low – a resolution of around 100×100 pixels should be preserved to maintain the imaging character of the technique. At these resolution the gain in speed of these cameras would still be around ten, compared to the present system. But to perform a measurement at that speed also a laser with a ten times higher output power is needed. Lasers with 50 W and the required coherence length of some millimeters are, however, quite expensive. If only the out-of-plane component is of interest much more affordable diode lasers can also be used, since the required coherence length is much shorter. Alternatively also an image intensifier could be employed to avoid the need for such a high power laser.

One of the cameras using the ISIS-V2 sensor would be an interesting alternative as their resolution at 1 Mfps is reasonably high. However, the sensitivity of this sensor to light is rather low which requires even more illumination power, or an intensifier with a higher gain.

The framing cameras which offer the highest frame rates and resolutions could give the largest increase in the measurement range – but this possible improvement is also accompanied with a high risk: The influence of a small misalignment between the sensors and the use of an image intensifier as a shutter in front of each sensor in the beam splitter based systems, cannot be assessed. The manufacturing related differences between the intensifiers might introduce too many differences in the signal for each sensor such that the Doppler signal is lost.

At the same time, the existing system should also be applied to different flow fields to further demonstrate the potential of the technique. It could be applied to water tunnels as their maximum velocity is usually limited to around 1 m/s. The velocity distribution around different challenging test objects such as delta wings or cylinders could be measured, especially also

in combination with simultaneous PIV recordings.

In addition the predicted scalability of ILDV to large measurement areas can be further assessed with the existing system. Different measurements in air should be performed where the crossing angle of the light sheets is further reduced and the measurement area simultaneously increased. This might show that the technique can be applied to large scale experiments such as building aerodynamics, tunnel aerodynamics or the flow behind wind turbines even with rather slow high speed cameras and low power lasers.

Bibliography

- Adrian RJ** (1972) Statistics of laser Doppler velocimeter signals: frequency measurement, *J. Phys. E: Sci. Instrum.*, 5, 91–95
- Ainsworth RW, Thorpe SJ, Manners RJ** (1997) A new approach to flow-field measurement - a view of Doppler global velocimetry techniques, *Int. J. Heat Fluid Flow*, 18, pp 116–130
- Albrecht HE, Borys M, Damaschke N, Tropea C** (2003) *Laser Doppler and phase Doppler measurement techniques*, Springer-Verlag, Heidelberg
- Arroyo P, Greated CA** (1991) Stereoscopic particle image velocimetry, *Meas. Sci. Technol.*, 2, pp 1181–1186
- Beer S, Seitz P** (2005) Real-time tomographic imaging without x-rays: a smart pixel array with massively parallel signal processing for real-time optical coherence tomography performing close to the physical limits, *Research in Microelectronics and Electronics 2005 PhD*, 2, pp 135–138
- Beutner TJ, Elliott GS, Mosedale A, Carter C** (1998) Doppler global velocimetry applications in large scale facilities, *AIAA 20th Advanced Measurement and Ground Testing Conference*, AIAA Paper 98-2608
- Chin CT, Lancee C, Borsboom J, Mastik F, Frijlink M, de Jong N, Versluis M, Lohse D** (2003) Brandaris 128: A digital 25 million frames per second camera with 128 highly sensitive frames, *Rev. Sci. Instrum.*, 74, pp 5026–5034
- Czarske J, Büttner L, Razik T, Müller H** (2002) Boundary layer velocity measurements by a laser Doppler profile sensor with micrometre spatial resolution, *Meas. Sci. Technol.*, 13, pp 1979–1989
- Etoh TG, Poggemann D, Kreider G, Mutoh H, Theuwissen A, Ruckelshausen A, Kondo Y, Maruno H, Takubo K, Soya H, Takehara K, Okinaka T, Takano Y** (2003) An image sensor which captures 100 consecutive frames at 1000000 frames/s, *IEEE Trans. Electron Devices*, 647, pp 112–116

- Etoh TG, Dung NH, Dao SVT, Le CV, Tanaka M** (2011) Backside illuminated CCD operating at 16,000,000 frames per second with sub-ten-photon sensitivity, *Nucl. Instrum. Methods A*, 50, pp 144–151
- Elliott GS, Beutner TJ** (1999) Molecular filter based planar Doppler velocimetry, *Prog. Aerosp. Sci.*, 35, pp 799–845
- Elsinga GE, Scarano F, Wieneke B, van Oudheusden BW** (2006) Tomographic particle image velocimetry, *Exp. Fluids*, 41, pp 933–947
- Ghiglia DC, Romero LA** (1994) Robust two-dimensional weighted and unweighted phase unwrapping that uses fast transforms and iterative methods, *J. Opt. Soc. Am. A*, 11, pp 107–117
- Landolt A, Roesgen T** (2009) Global Doppler frequency shift detection with near-resonant interferometry, *Exp. Fluids*, 47, pp 733–743
- Lichtsteiner P, Posch C, Delbruck T** (2007) An 128x128 120dB 15us-latency temporal contrast vision sensor, *IEEE J. Solid-State Circuits*, 43, pp 566–576
- Maas HG, Gruen A, Papantoniou D** (1993) Particle tracking velocimetry in three-dimensional flows, *Exp. Fluids*, 15, pp 133–146
- Meier AH, Roesgen T** (2009) Heterodyne Doppler global velocimetry, *Exp. Fluids*, 47, pp 665–672
- Meier AH, Roesgen T** (2012) Imaging laser Doppler velocimetry, *Exp. Fluids*, 52, pp 1017–1026
- Miller KS, Rochwarger MM** (1972) A covariance approach to spectral moment estimation. *IEEE Trans. Inf. Theory*, 18, pp 588–596
- Nobes DS, Ford HD, Tatam RP** (2004) Instantaneous, three-component planar Doppler velocimetry using imaging fibre bundles, *Exp. Fluids*, 36, pp 3–10
- Prasad AK, Adrian RJ** (1993) Stereoscopic particle image velocimetry applied to liquid flows, *Exp. Fluids*, 15, pp 49–60
- Raffel M, Westerweel J, Willert C, Gharib M, Kompenhans J** (1996) Analytical and experimental investigations of dual-plane particle image velocimetry, *Opt. Eng.*, 35, pp 2067–2074

- Resagk C, du Puits R, Maystrenko A, Thess A, Bosbach J, Wagner C** (2005) Large-scale particle image velocimetry in convective air-flow, Proc. 6th Int. Symposium on Particle Image Velocimetry
- Roehle I, Schodl R, Voigt P, Willert C** (2000) Recent developments and applications of quantitative laser light sheet measuring techniques in turbomachinery components, Meas. Sci. Technol., 11, pp 1023–1035
- Samimy M, Wernet MP** (2000) Review of planar multiple-component velocimetry in high-speed flows, AIAA Journal, 38, pp 553–574
- Smith MW, Drummond JP, Northam GB** (1996) Application of absorption filter planar Doppler velocimetry to sonic and supersonic jets, AIAA Journal, 34, pp 434–441
- vom Stein HD, Pfeiffer HJ** (1969) A Doppler difference method for velocity measurements, Metrologia, 5, pp 59–61
- Willert CE, Gharib M** (1991) Digital particle image velocimetry, Exp. Fluids, 10, pp 181–193
- Willert CE, Stasicki B, Klinner J, Moessner S** (2010) Pulsed operation of high-power light emitting diodes for imaging flow velocimetry, Meas. Sci. Technol., 21, pp 1–11
- Yeh Y, Cummins HZ** (1964) Localized fluid flow measurements with an He-Ne laser spectrometer, Appl. Phys. Lett., 4, pp 176–179

Curriculum vitae

| | |
|---------------------------------------|---------------------------------------------------------------------------------------------------------------------------------------------------------------------|
| Name | Alexander Heinz Meier |
| Date of birth | August 2, 1980 |
| Place of birth | Zürich, Switzerland |
| Nationality | Swiss |
| July 2005 to March 2011 | PhD student, research and teaching assistant, and lecturer under the supervision of Prof. Dr. T. Rösgen at the Institute of Fluid Dynamics, ETH Zürich, Switzerland |
| March 2005 | Diploma (Dipl. Masch.-Ing. ETH, equivalent to Master's degree) in Mechanical Engineering, ETH Zürich, Switzerland |
| October 2000 to March 2005 | Studies in Mechanical Engineering, ETH Zürich, Switzerland |
| January 2000 | Matura (high-school graduation), Kantonsschule Zürcher Oberland, Wetzikon, Switzerland |

List of Publications

Refereed Journal Articles

- Meier AH, Roesgen T** (2009) Heterodyne Doppler Global Velocimetry, *Exp. Fluids*, 47, pp 665–672
- Meier AH, Roesgen T** (2012) Imaging laser Doppler velocimetry, *Exp. Fluids*, 52, pp 1017–1026
- Prochazka L, Meier AH, Viggiani A, Roesgen T** (2012) Optically interrogated MEMS pressure sensor array, *Exp. Fluids*, 52, pp 1003–1015
- Hermanns T, Strebel DD, Hefermehl LJ, Gross O, Mortezavi A, Mueller A, Eberli D, Muentener M, Michel MS, Meier AH, Sulser T Seifert HH** (2011) Lithium triborate laser vaporization of the prostate using the 120 w, high performance system laser: High performance all the way?, *The Journal of Urology*, 185, pp 2241-2247
- Hermanns T, Sulser T, Hefermehl L, Strebel D, Michel M, Muentener M, Meier AH, Seifert HH** (2009) Loss of power output and laser fibre degradation during 120 watt lithium-triborate hps laser vaporisation of the prostate, *Proc. SPIE*, 7161, pp 71611I–71611I-10

Refereed Proceeding Articles

- Meier AH, Schlamp S** (2006) Improved signal intensity for transient grating spectroscopy using a PIV laser, *AIAA Paper 2006-2973*
- Meier AH, Roesgen T** (2008) Heterodyne doppler global velocimetry, In 14th Int Symp on Applications of Laser Techniques to Fluid Mechanics, Lisbon, Portugal, 07-10 July 2008.
- Meier AH, Roesgen T** (2010) Imaging laser doppler velocimetry, In 15th Int Symp on Applications of Laser Techniques to Fluid Mechanics, Lisbon, Portugal, 05-08 July, 2010.
- Prochazka L, Meier AH, Viggiani A, Roesgen T** (2010) Optically interrogated MEMS pressure sensor array, In 15th Int Symp on Applications of Laser Techniques to Fluid Mechanics, Lisbon, Portugal, 05-08 July, 2010.

Landolt A, Borer D, Meier AH, Roesgen T (2010) Quantitative flow visualization applied to a passive wake control problem, In *Aerodynamics of Heavy Vehicles III: Trucks, Buses and Trains* September 12-17, 2010, Potsdam, Germany.